



INTERNATIONAL UNIVERSITY LIAISON INDONESIA (IULI)

BACHELOR'S THESIS

**COMPARATIVE NUMERICAL STUDY OF DOMINANT PERTURBATION
EFFECTS ON VLEO SATELLITE ORBIT DEGRADATION**

By

Renggani Ghifari

11202101009

Presented to the Faculty of Engineering and Life Sciences
In Partial Fulfilment Of the Requirements for the Degree of

SARJANA TEKNIK

In

AVIATION ENGINEERING

FACULTY OF ENGINEERING AND LIFE SCIENCES

BSD City 15345

Indonesia

Month YEAR

APPROVAL PAGE

COMPARATIVE NUMERICAL STUDY OF DOMINANT
PERTURBATION EFFECTS ON VLEO SATELLITE ORBIT
DEGRADATION

RENGGANI GHIFARI

11202101009

Presented to the Faculty of Engineering

In Partial Fulfillment of the Requirements for the Degree of

SARJANA TEKNIK

In

AVIATION ENGINEERING

FACULTY OF ENGINEERING AND LIFE SCIENCES

Triwanto Simanjuntak, PhD

Thesis Advisor

Date (MM/DD/YYYY)

Dipl.-Ing. Sentot Wahjoe Georitno, M.Si.

Dean of Faculty of Engineering and Life Sciences

Date (MM/DD/YYYY)

COMPARATIVE NUMERICAL STUDY OF DOMINANT PERTURBATION EFFECTS ON VLEO
SATELLITE ORBIT DEGRADATION

EXAMINERS APPROVAL PAGE

Dewi Habsari Budiarti, PhD

BRIN (National Research and Innovation Agency)

Date (MM/DD/YYYY)

Dr. Eng. Ridlo Erdata Nasution

BRIN (National Research and Innovation Agency)

Date (MM/DD/YYYY)

Dr. Eng. Ressa Octavianty

Department of Aviation Engineering - IULI

Date (MM/DD/YYYY)

STATEMENT BY THE AUTHOR

I hereby declare that this submission is my own work and to the best of my knowledge, it contains no material previously published or written by another person, nor material which to a substantial extent has been accepted for the award of any other degree or diploma at any educational institution, except where due acknowledgement is made in the thesis.

Renggani Ghifari

Student

Date (MM/DD/YYYY)

ABSTRACT

Comparative Numerical Study of Dominant Perturbation Effects on VLEO
Satellite Orbit Degradation

by

Renggani Ghifari

Triwanto Simanjuntak, PhD, Advisor

, Co-Advisor

Very Low Earth Orbit (VLEO) offers headways for Earth Observation (EO), low-latency communications, and intelligence gathering, but its benefits come at the cost of strongly amplified perturbations from atmospheric drag and Earth's oblateness. This work presents an open-source orbital propagation framework developed in Scilab, using custom mathematical models for both Earth oblateness and drag effects. The intention is to validate the tool against two-body motion and then quantify orbit type-dependent rates of nodal regression, perigee rotation, and orbital decay. The results reproduced and predicted real-world orbital behaviors under various perturbation models to an extant. Analyses of results underscore the trade-offs between coverage, lifetime, and maintenance. By providing a transparent, reproducible simulation environment, this study aims to advance mission design capabilities for next-generation VLEO satellites.

Keyword(s): *Very Low Earth Orbit, Orbital Perturbations, Atmospheric Drag, J_2 , Scilab, Spacecraft Mission Design*

ACKNOWLEDGEMENTS

The author believes that any accomplishment made must also be viewed within a community context, for its realisation is that of a collaborative and supportive nature, despite its attribution to the sole author. As such, gratitude is owed to many of those who have supported the author's efforts.

1. No amount of appreciation will ever be adequate for all that has been given by my parents, for all I am cannot be if not for them.
2. Triwanto Simanjuntak, PhD, who I am deeply indebted to for the generosity that has been given in the form of guidance, time, patience, and wisdom. His dedication and resolve were a measure that I could hold to emulate those same aspects within myself.
3. All those that have been the backbone in keeping academic activities alive in IULI. I hope with this contribution; I could add to the body of knowledge and encourage others to do so.
4. The company of friends that I have made in classes, study halls, libraries, and pursuit of a shared dream.
5. My big sister, who has always challenged me to find the best parts of myself. Any standards I have for kindness, strength, and tolerance are only there because she showed the way.
6. My uncle Ben, the reason I look to the stars.

Contents

Approval Page	i
EXAMINERS APPROVAL PAGE	ii
Statement by The Author	iii
Abstract	iv
Acknowledgements	v
Contents	vi
List of Figures	x
List of Tables	xiii
1 Introduction	1
1.1 Background	1
1.2 Problem Statement	2
1.3 Research Objectives	2
1.4 Research Scope and Limitation	2
1.5 Significance of the Study	3
2 Literature Review	4
2.1 Introduction to Very Low Earth Orbit (VLEO) Satellites	4
2.1.1 Definition and Classification of VLEO	4
2.1.2 Current and Planned VLEO Satellite Missions	4
2.1.3 Advantages and Challenges of VLEO Operations	6
2.2 Orbital Mechanics Fundamentals	8

2.2.1	Keplerian Elements and Two-Body Problem	8
	Specific Dynamic Energy Conservation Law	10
	Kepler's Zeroth Law	11
	Kepler's First Law	12
	Kepler's Second Law	14
	Kepler's Third Law	16
2.2.2	Orbital Perturbation Theory Basics	18
2.2.3	Fundamentals of Orbital Decay	19
2.3	Perturbation Forces in VLEO	19
2.3.1	Atmospheric Drag Effects	19
2.3.2	Earth's Non-Spherical Gravitational Field (J2-J4 Effects)	22
2.4	Numerical Methods for Orbit Propagation	24
2.4.1	Overview of Common Numerical Integrators	24
3	Research Methodology	26
3.1	Research Outline	26
3.2	SCILAB Programming Language	27
3.3	Data Collection	28
3.3.1	Atmospheric Model Data: USSA76	28
3.3.2	Zonal Harmonics Data: J_2 from Vallado	29
3.4	Mathematical Modelling	29
3.4.1	Orbital Elements Conversion from State Vectors	29
3.4.2	State Vector Conversion from Orbital Elements	31
3.4.3	Atmospheric Density Model: USSA76	32
3.4.4	Custom Fourth-Order Runge–Kutta Integrator	35
3.4.5	Perturbation Models for Orbital Propagation	36
	Atmospheric Drag Model (drag)	37
	J_2 Perturbation Model (j2rates)	37
	Combined Drag and J_2 Model (dragj2)	38
3.5	Simulation & Comparative Analysis	38
3.5.1	Simulation Configuration	39
3.5.2	Orbital Element Extraction	39
3.5.3	Orbit-Based Reframing of Data	40

3.5.4	Comparative Analysis Approach	41
4	Results and Discussions	43
4.1	Verification of Two-Body Restricted Simulation	43
4.2	VLEO Satellites Affected by Dominant Perturbation	46
4.2.1	VLEO Satellites Affected by J_2 Perturbation	48
4.2.2	VLEO Satellites Affected by Atmospheric Drag	51
4.2.3	Atmospheric Drag + J_2 Perturbed Simulation	53
4.3	Variation of Initial Orbital Parameters	56
4.3.1	Variation of Initial Orbital Parameters – i	56
Simulation With J_2 Perturbation Model	56	
Simulation With Drag + J_2 Perturbation Model	60	
4.3.2	Variation of Initial Parameters – a	64
Simulation With Drag Perturbation Model	65	
Simulation With J_2 Perturbation Model	68	
Simulation With Drag + J_2 Perturbation Model	74	
5	Summary, Conclusion, Recommendation	80
5.1	Summary of Research	80
5.2	Research Conclusions	81
5.2.1	The Success of the Simulation	81
Two-Body Restricted Simulations	81	
J_2 Perturbed Simulations	81	
Drag Perturbed Simulations	82	
Drag + J_2 Perturbed Simulations	83	
5.2.2	Importance of Findings	83
Orbital Lifetime and Altitude Planning	84	
Inclination and Perturbation Sensitivity	84	
Coverage vs. Lifetime Trade-offs	85	
Eccentricity Damping and Imaging Stability	85	
Increased Revisit Opportunities from Shorter Periods	85	
Constellation Phasing and Passive Control	86	
5.3	Recommendations for Future Research	87

Bibliography	88
Appendices	91
Turnitin Report	104
Curriculum Vitae	112

List of Figures

2.1	Coordinate system representation.	9
2.2	Coordinate System for Specific Dynamic Energy Conservation Law.	11
2.3	Coordinate System for Conservation of Specific Angular Momentum.	12
2.4	Coordinate System for Conservation of Kepler's First La.	13
2.5	Coordinate System With \bar{B} as a Reference Direction.	14
2.6	Coordinate System as a Reference Direction.	15
2.7	Coordinate System as a Reference Direction.	15
2.8	Coordinate System as a Reference Direction.	16
2.9	Classical orbital elements in 3D: showing inclination i , RAAN Ω , argument of periapsis ω , and true anomaly ν	18
2.10	Total pressure and mass density as a functiion of geometric altitude, USSA76 [13].	20
3.1	Research flowchart	26
3.2	Interpolated Atmospheric Density Profile from USSA76 (Log Scale)	33
3.3	Atmospheric Density Model: <code>atmosphere(z)</code> function flowchart	34
3.4	Workflow of Simulations	42
4.1	Two-Body Restricted Orbital Elements' Variation Over Time.	44
4.2	Altitude variation of a VLEO satellite in Two-Body restricted simulation.	46
4.3	Altitude variation of a VLEO satellite due to atmospheric drag and J_2 pereturbatiion, respectively.	47
4.4	Variation of the RAAN of a LEO due to J_2 perturbation.	48
4.5	Variation of the argument of perigee of a LEO due to J_2 perturbation.	49
4.6	Variation of the semi-major axis of a VLEO due to J_2 perturbation.	49

4.7 Variation of the eccentricity of a LEO due to J_2 perturbation.	50
4.8 Long/short periodic beat period from zonal harmonics [15]	50
4.9 Variation of the eccentricity of a LEO due to atmospheric drag.	51
4.10 Variation of the semi-major axis of a VLEO due to atmospheric drag. .	52
4.11 Variation of the argument of perigee of a LEO due to atmospheric drag.	52
4.12 Altitude variation of a VLEO satellite due to atmospheric drag + J_2 perturbation.	53
4.13 Variation of the semi-major axis of a VLEO due to atmospheric drag + J_2 Perturbation.	54
4.14 Variation of the eccentricity of a LEO due to atmospheric drag + J_2 Perturbation.	54
4.15 Variation of the argument of perigee of a LEO due to atmospheric drag + J_2 Perturbation.	55
4.16 RAAN regression due to atmospheric drag + J_2 Perturbation.	55
4.17 Variation of the RAAN of a VLEO due to J_2 perturbation for different inclinations.	58
4.18 Variation of the argument of perigee of a VLEO due to J_2 perturbation for different inclinations.	59
4.19 Variation of the semi-major axis of a VLEO due to J_2 perturbation for different inclinations.	59
4.20 Variation of the semi-major axis of a VLEO due to drag + J_2 perturbation for different inclinations.	61
4.21 Variation of the semi-major axis of a VLEO due to atmospheric drag perturbation for different a	66
4.22 Semi-major axis change with number of revolutions due to atmospheric drag perturbation for different a	66
4.23 Variation of the eccentricity of a VLEO due to atmospheric drag perturbation for different a	67
4.24 Variation of the argument of perigee of a VLEO due to atmospheric drag perturbation for different a	67
4.25 Variation of the RAAN of a VLEO due to atmospheric drag perturbation for different a	68

4.26 Variation of the semi-major axis of a VLEO due to J_2 perturbation for different a	69
4.27 Semi-major axis change with number of revolutions due to J_2 perturbation for varying a	70
4.28 Variation of the eccentricity of a VLEO due to J_2 perturbation for different a	71
4.29 Variation of the argument of perigee of a VLEO due to J_2 perturbation for different a	72
4.30 Variation of the RAAN of a VLEO due to J_2 perturbation for different a	73
4.31 Variation of the semi-major axis of a VLEO due to atmospheric drag + J_2 perturbation for different a	74
4.32 Semi-major axis change with number of revolutions due to atmospheric drag + J_2 perturbation for varying a	75
4.33 Variation of the eccentricity of a VLEO due to atmospheric drag + J_2 perturbation for different a	76
4.34 Variation of the argument of perigee of a VLEO due to atmospheric drag + J_2 perturbation for different a	77
4.35 Variation of the RAAN of a VLEO due to atmospheric drag + J_2 perturbation for different a	78

List of Tables

2.1	Summary of Orbital Elements	17
2.2	Zonal Harmonic Coefficients	23
4.1	Initial and final orbital parameters of the satellite obtained from a two-body restricted simulation.	43
4.2	Initial and final orbital parameters of a small spherical VLEO satellite under various perturbations.	47
4.3	Final Orbital Parameters of Satellite under J_2 Perturbation	48
4.4	Final Orbital Parameters of Satellite under Atmospheric Drag Perturbation	51
4.5	Final Orbital Parameters of Satellite under Atmospheric Drag + J_2 Perturbation	53
4.6	Final orbital parameters after a 16-day propagation under J_2 perturbation. Initial parameters are listed in Table 4.1.	56
4.7	Comparison of J_2 -induced precession rates from GP theory and numerical simulation over a 16-day period.	57
4.8	Final Orbital Parameters of Satellite Cases with Varying i under Atmospheric Drag + J_2 Perturbation.	60
4.9	Initial Orbital Parameters of Satellite Cases with Varying Semimajor Axis (a).	65
4.10	Final Orbital Parameters of Satellite Cases with Varying a under Atmospheric Drag Perturbation.	65
4.11	Final Orbital Parameters of Satellite Cases with Varying a under J_2 Perturbation.	68
4.12	Calculated Regression and Rotation Rates of Ω and ω over 14 Days under J_2 Perturbation.	72

4.13 RAAN regression rate $\dot{\Omega}$ and argument of perigee rotation rate $\dot{\omega}$ under J_2 Perturbation, computed using GP theory.	72
4.14 Final Orbital Parameters of Satellite Cases with Varying a under Atmospheric Drag + J_2 Perturbation.	74

List of Abbreviations

VLEO Very Low Earth Orbit
EO Earth Observation

Dedicated to my parents

CHAPTER 1

INTRODUCTION

1.1 Background

The Very Low Earth Orbit (VLEO) region is increasingly gaining interest for satellite missions. This renewed attention is driven by several factors, including advances in miniaturization, improved propulsion and attitude control systems, reductions in launch costs, and growing demand for high-resolution Earth observation and low-latency communications. Operating at such altitudes offers distinct benefits in performance and coverage; however, it also introduces significant engineering challenges, particularly in orbital longevity and stability [1].

In VLEO, the effects of Earth's oblateness (represented primarily by the J_2 zonal harmonic) and atmospheric drag are dominant perturbations that can cause rapid changes in the orbit [16], potentially degrading satellite performance or mission duration if not accounted for precisely. Accurately predicting these effects is essential for mission designers seeking to plan or maintain sustained operations in this orbital regime.

Several propagation methods exist to account for orbital perturbations, though they are bound by the accuracy of their assumptions, numerical stability, and model reliability (ex. standard atmospheric or gravity models). As such numerical propagation using open-source tools is not only a cost-effective approach but also one that can be tailored and validated independently.

This research is backboned with Scilab, a fully open-source numerical computing environment, to build a custom orbital propagation framework. By doing so, it enables direct modelling of dominant perturbative forces while also promoting transparency and accessibility in orbital mechanics research and education.

1.2 Problem Statement

Despite the advantages of deploying satellites in the VLEO region, the strong influence of J_2 perturbation and atmospheric drag leads to rapid orbital changes that must be predicted with high accuracy. However, existing tools are often proprietary, limiting flexibility and accessibility, while theoretical models alone are insufficient without numerical validation. There remains a need to simulate and analyse the dominant perturbations that affect satellite motion in VLEO using a transparent and customizable framework to better understand their behaviour and provide more informed guidance for mission design.

1.3 Research Objectives

The objectives of this research are to investigate:

- The development of a fully open-source, custom orbital propagator using Scilab as an accessible alternative to proprietary tools.
- The accurate modelling and simulation of dominant perturbative effects in VLEO, particularly J_2 and atmospheric drag, using self-constructed numerical integrators.
- The ability of such models to correctly replicate or predict satellite behaviour over time in the presence of these perturbations.
- The potential of this research to contribute to better-informed mission planning, orbit selection, and operational strategies for future VLEO missions.

1.4 Research Scope and Limitation

The focus will be on satellite behaviour exclusively within the VLEO region. The scope is limited to the considerations of the two most dominant perturbative effects in this regime: atmospheric drag and the Earth's oblateness. Other perturbations, such as higher-order zonal harmonics, tesseral effects, third-body influences, or solar radiation pressure, are outside the current scope but may be addressed in future work.

1.5 Significance of the Study

This study brings into light the importance of accurately evaluating Earth's dominant perturbative forces, especially in the context of the increasingly relevant VLEO operational regime. By developing a self-contained orbital propagation framework entirely in Scilab, the research presents a transparent, reproducible, and open-source alternative to commonly used but proprietary tools. This contribution is particularly significant in educational and research contexts, where accessibility is crucial.

Beyond technical implementation, the work also aims to demonstrate the value of numerically simulating orbital decay and precession effects, providing deeper insight into the behaviour of satellite orbits under realistic conditions. These insights are vital for mission designers and satellite operators who must account for such perturbations when selecting orbits, defining mission lifetimes, or designing control strategies. By accurately predicting orbital evolution under dominant forces, this research contributes to safer, more efficient, and more cost-effective mission planning in the VLEO domain.

CHAPTER 2

LITERATURE REVIEW

2.1 Introduction to Very Low Earth Orbit (VLEO) Satellites

2.1.1 Definition and Classification of VLEO

Very Low Earth Orbits (VLEO) are considered to be orbital paths that are substantially closer to the Earth's surface. Though all LEO satellites come in contact with aerodynamic forces of atmosphere residue, the VLEO area is considered to be situated where the magnitude of those challenges are at its highest intensity, below 450-500 km[2]. The lower boundary of VLEO is indistinguishable to the Kármán line, which is a conventional definition of boundary separating Earth's atmosphere and outer space[3].

Therefore, VLEO is an orbital area below approximately 450 kilometres altitude, with 100 km above sea level generally accepted as the lower boundary of space.

2.1.2 Current and Planned VLEO Satellite Missions

When a satellite comes in contact with the atmospheric drag of low orbits, it significantly effects its orbital and attitude dynamics, which in turn limits a satellite's mission duration and range. As such, missions below 500 km have been few and far between as the short mission lifetime and environmental challenges do not often merit the high expenditure of launching a spacecraft. However, there have been missions that have sustained, and even remain to function in operations within the VLEO range.

Increased aerodynamic forces can be tolerated for goals that are deemed crucial. Reconnaissance are one such goal, as satellites are a remote and minimally invasive method to visually obtain strategic information. This was a driving force behind the first spy satellite programs, the very first was the U.S.' CORONA and Soviet Union's Zenit reconnaissance satellites in the 1950s[4], these program made a trade-off utilising eccentric orbits with VLEO perigees to prolong orbit lifetime, in consequence limiting the time window when imaging operations could be conducted. Space stations, such as the International Space Station (ISS) and Tiangong, maintain their orbits below 450 km, however necessitate periodic resupply missions to provide propellant for sustaining their orbits.

Operations in VLEO offers significant advantages over those operating in LEO, it could open up new possibilities for military intelligence, communication operations, and research missions. As such there has been a concerted effort to develop technology that would enable a spacecraft to undergo longer duration missions in the region. On 17 March 2009, ESA launched the Gravity Field and Steady-State Ocean Circulation Explorer (GOCE), utilising a VLEO orbital path to provide greater detail in mapping the Earth's Gravity Field. The spacecraft sustained a circular orbit at an altitude 254.9 km for 4 years, 7 months, and 3 days. For 4.6 years, the spacecraft sustained a 254.9 km-altitude circular orbit, utilising an ion propulsion system and a unique arrow-fletching shape as a means of minimizing drag.

JAXA's Super Low Altitude Test Satellite (SLATS) was a mission dedicated to demonstrating these drag-minimising methods in VLEO operations. Ion engines fire out charged particles behind the spacecraft consistently, providing stability in its trajectory through a constant level of thrust against aerodynamic turbulence. Unlike GOCE's arrow-fletching shape, SLATS utilized thin solar array "wings" to aid in aerodynamic stability.

Future VLEO missions plan to benefit and even improve on these drag-minimizing methods.

2.1.3 Advantages and Challenges of VLEO Operations

The proximity of VLEO satellite's orbital paths to the Earth's surface have numerous advantages which are particularly relevant to Earth Observation (EO) operations. EO dedicated satellites operate on remote-sensing principles, where they collect data without physically interacting with the source. As a result of this, technological advances have been encouraged to overcome VLEO's unique physical and operational challenges to provide a meaningful orbital lifetime suitable for EO missions.

Advantages that would come from EO missions in the VLEO regime would impact space operations, applications and employability, which includes, but is not limited to:

- **Communication Efficiency:** The power required for data transfer can be significantly reduced as the distance between satellites and ground stations are decreased. This can be utilized in either or both of these ways, lower the power needs or achieve greater data transfer rate with the same power [5].
- **Higher Resolution Imagery:** Optical satellites will have the ability to capture images of a higher resolution due to the reduction in orbital altitude within VLEO compared to LEO [6].
- **Active Sensing:** Synthetic Aperture Radar (SAR) and Light Detection & Ranging (LIDAR) are remote sensing technologies that can capitalize on its application within the VLEO region. As the resulting proximity towards target areas will improve signal-to-noise ratio [7].
- **Temporal Resolution:** The time between when a satellite reappears at predetermined point will be reduced when operating at smaller orbits, also reducing the number of satellites required [7].
- **Lower-Latency Data Transfer:** Reducing the time taken between data transmission and reception, is crucial for modern satellite-enabled communications (satcom). Missions in VLEO will inevitably explore lower orbits to capitalize on latency reduction. For example, LEO-based satcom constellations offer 32-millisecond latency compared to the 600-millisecond provided by GEO-based satellites [8].

Challenges would need to be addressed as operations in VLEO have not yet achieved maturity, some of them being:

- **Constellation Numbers:** As altitude decreases, more satellites are required to provide the same coverage area as higher altitude constellations due to the smaller area each satellite can cover at lower altitudes [9].
- **Satellite Design:** The architecture of the platforms would have to evolve from the general shape of large square object with huge solar panels, as such a form would invite significant drag in VLEO, rendering the satellite ineffective. Designs will have to combine smaller size and more streamlined shapes for drag reduction, which will enable better spacecraft control and select manoeuvrability for drag reduction in a variable atmosphere and for end-of-life re-entry manoeuvre [10].
- **Lower Thermosphere Perturbations:** As mentioned, operation in VLEO will have to face the challenges of operating against the residual atmosphere in the thermosphere. In addition, satellites in VLEO are subject to substantial amounts of elemental oxygen, otherwise known as atomic oxygen (AO), a highly reactive form of oxygen that will corrodes most substances quickly. This has remained one of the main limiting considerations for utilising these altitudes. There is also the subject of earth oblateness, and its effect that will be delved into shortly [11].
- **Platform Stability:** The precision that those aforementioned operations require are paramount, and as they are dependent on the platform's stability, residual atmosphere that could cause aerodynamic perturbations will have to be considered [9].
- **Regulation:** The "boom" of VLEO operations may require an evolution of launch and operating licensing practices to account for unprecedented dynamics and the impacts on increased space activities [12].

2.2 Orbital Mechanics Fundamentals

2.2.1 Keplerian Elements and Two-Body Problem

The two-body problem is mostly used to describe the motion of two bodies in space interacting with each other completely through their gravitational properties. It is an important part of astrodynamics as it is the basis point of calculations that will allow for a more complex problems such as the motion of a spacecraft under the influence of a central body. In such a system, it is assumed that all other forces are negligible, and the only force influencing either of the masses is purely the gravitational attraction of the other mass.

Two body astrodynamics will be governed by differential equation derived from two laws originated by Sir Isaac Newton. Newton's Law of Universal Gravitation states that all massed particles within the universe attract one another. The equation for universal gravitation takes the form:

$$F_g = G \frac{Mm}{r^2} \quad (2.1)$$

where

- F_g is for the force between the masses.
- G is the gravitational constant. The measured value of G in SI units is $6.674 \times 10^{-11} m^3 \cdot kg^{-1} \cdot s^{-2}$.
- M is the mass of the Earth, with the current best estimate of $5.972 \times 10^{-24} kg$.
- m is the mass of the satellite.
- r is the distance between the centres of first mass and second mass.

$$F = ma \quad (2.2)$$

Newton's 2nd Law state that the force acting on a system is equal to the mass of the system multiplied by its acceleration. In the above equation, F is the force applied to the system, m stands for its and a describes its acceleration.

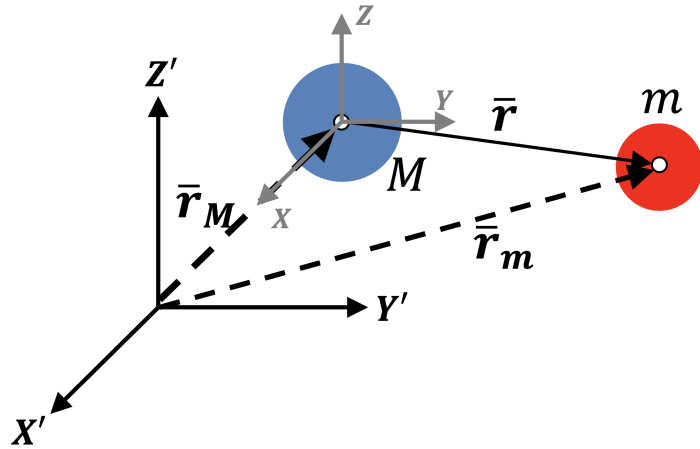


FIGURE 2.1: Coordinate system representation.

Calculation requires a reference frame to be defined. The frame used will be the one in Figure 2.1, a coordinate system with M and m as the masses, where:

- M is the mass of the larger body;
- m is the mass of the smaller body;
- \bar{r}_M is the vector from the origin of the reference coordinate system to the centre of M ;
- \bar{r}_m is the vector from the origin of the reference coordinate system to the centre of m ;
- \bar{r} is the vector between M and m ;
- $X'Y'Z'$ are the axis of the inertial coordinate system; and
- XYZ are the axis of the geocentric coordinate system.

We can discern now how the vector from Earth to the satellite looks like in mathematical form,

$$\bar{r} = \bar{r}_M - \bar{r}_m \quad (2.3)$$

With $\bar{r} = \bar{r}_m - \bar{r}_M$ being the position vector of the satellite relative to the Earth, its time derivative will define the relative velocity:

$$\dot{\bar{r}} = \dot{\bar{r}}_m - \dot{\bar{r}}_M = \bar{v} \quad (2.4)$$

The defined inertial reference frame allows differentiation of the vectors without considering the derivatives of each axis of the coordinate system. Following the equation, the satellite's acceleration relative to the Earth can be found,

$$\bar{r} = \bar{r}_M - \bar{r}_m \Rightarrow \ddot{\bar{r}} = \ddot{\bar{r}}_M - \ddot{\bar{r}}_m = \bar{a} \quad (2.5)$$

and combining Newton's Second Law of Motion and Universal Law of Gravitation shown here,

$$\Sigma \bar{F} = \frac{d(m\bar{v})}{dt} = m\bar{a} \quad (2.6)$$

$$\Sigma \bar{F} = -\frac{GMm}{r^2} \left(\frac{\bar{r}}{r} \right) \quad (2.7)$$

will lead to the inertial force on the satellite and on the Earth, respectively,

$$m\ddot{\bar{r}}_m = -\frac{GMm}{r^2} \left(\frac{\bar{r}}{r} \right) \quad (2.8)$$

$$M\ddot{\bar{r}}_M = -\frac{GMm}{r^2} \left(\frac{\bar{r}}{r} \right) \quad (2.9)$$

Now since in the cases that we will be exploring where the Earth's is exceedingly high than that of the orbiting body (satellite), to such a degree that the sum of the two masses would just virtually be the mass of the Earth itself. It would be reasonable to assume that $M \gg m$ so that the expression can become:

$$\ddot{\bar{r}} = -\frac{G(M)}{r^3} \bar{r} \quad (2.10)$$

which then gravitational parameter of the referenced "Earth" can be denoted using μ

$$\ddot{\bar{r}} = -\frac{\mu}{r^3} \bar{r} \quad (2.11)$$

Specific Dynamic Energy Conservation Law

Then, apply the scalar product of \bar{r} to both sides to get,

$$\bar{r}\ddot{r} = -\bar{r}\frac{\mu}{r^3}\bar{r} \quad (2.12)$$

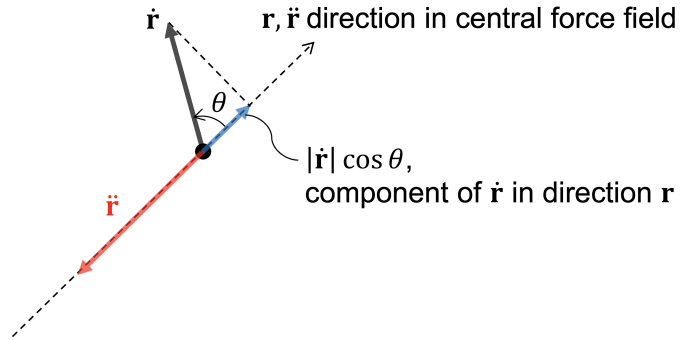


FIGURE 2.2: Coordinate System for Specific Dynamic Energy Conservation Law.

Defined is the equation that expresses the balance with respect to energy. This relation is then applied,

$$\dot{r}\ddot{r} = \frac{1}{2} \frac{d}{dt}(\dot{r}\dot{r}) = \frac{d}{dt}\left(\frac{v^2}{2}\right) \quad \text{and} \quad \bar{r}\dot{r} = \frac{1}{2} \frac{d}{dt}(\bar{r}\bar{r}) = \frac{d}{dt}\left(\frac{r^2}{2}\right) \quad (2.13)$$

To eventually arrive at,

$$\frac{d}{dt}\left(\frac{v^2}{2}\right) + \frac{\mu}{r^3} \frac{d}{dt}\left(\frac{r^2}{2}\right) = \frac{d}{dt}\left(\frac{v^2}{2} - \frac{\mu}{r}\right) = 0 \quad (2.14)$$

The result after integration would then be

$$\frac{v^2}{2} - \frac{\mu}{r} = E \quad (2.15)$$

Derived would be the **specific dynamic energy conservation law**. The sum of the kinetic energy and the potential energy per unit mass of the universal gravitation force becomes the integration constant, denoted by E .

Kepler's Zeroth Law

We can use Equation 2.12 again, but now take it to express the balance with respect to moments. Apply the relation,

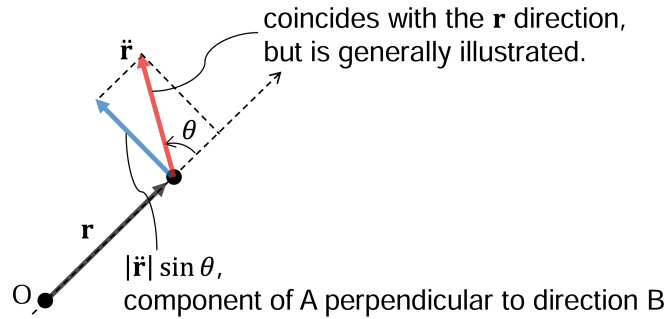


FIGURE 2.3: Coordinate System for Conservation of Specific Angular Momentum.

$$\bar{r} \times \bar{r} = 0 \quad \text{and} \quad \frac{d}{dt}(\bar{r} \times \dot{\bar{r}}) = \dot{\bar{r}} \times \dot{\bar{r}} + \bar{r} \times \ddot{\bar{r}} = \bar{r} \times \ddot{\bar{r}} \quad (2.16)$$

To arrive at,

$$\frac{d}{dt}(\bar{r} \times \dot{\bar{r}}) = 0 \quad (2.17)$$

The result after integration would have the position and velocity vectors remain in one place

$$\bar{r} \times \dot{\bar{r}} = \bar{r} \times \bar{v} = \bar{h} \quad (2.18)$$

The constant angular momentum vector is defined as \bar{h} , and \bar{r} and \bar{v} remains in the one plane. Essentially, the orbit is limited to one plane in space, and angular momentum is conserved in orbital motion. .

Kepler's First Law

Rearrange and apply the vector product of the specific angular momentum vector \bar{h} to Equation 2.11 .

$$\ddot{\bar{r}} \times \bar{h} + \frac{\mu}{r^3}(\bar{h} \times \bar{r}) = 0 \quad (2.19)$$

Examining closer, we would see that,

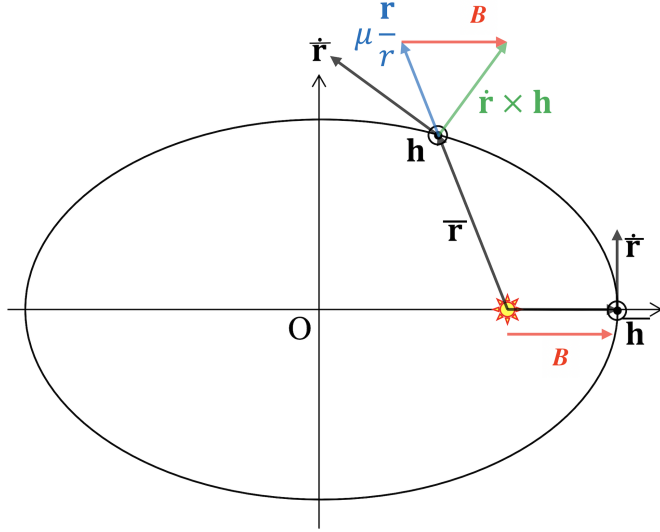


FIGURE 2.4: Coordinate System for Conservation of Kepler's First Law.

$$\frac{d}{dt}(\dot{r} \times \bar{h}) = \ddot{r} \times \bar{h} + \dot{r} \times \frac{d\bar{h}}{dt} = \ddot{r} \times \bar{h} \quad (2.20)$$

$$\frac{\mu}{r^3} \bar{r} \times \bar{h} = \frac{\mu}{r^3} \bar{r} \times (\bar{r} \times \bar{v}) = \frac{\mu}{r^3} \bar{r} \times (\bar{r} \times \dot{\bar{r}}) = \frac{\mu}{r^3} [(\bar{r} \cdot \dot{\bar{r}})\bar{r} - (\bar{r} \cdot \bar{r})\dot{\bar{r}}] \quad (2.21)$$

Continued:

$$\frac{\mu \dot{r}}{r^2} \bar{r} - \frac{\mu \dot{r}}{r} = \frac{d}{dt} \left(-\frac{\mu}{r} \right) = \frac{d}{dt} \left(\dot{r} \times \bar{h} - \mu \frac{\bar{r}}{r} \right) = 0 \quad (2.22)$$

Integrating this, we obtain

$$\dot{r} \times \bar{h} - \mu \frac{\bar{r}}{r} = \bar{B} \quad (2.23)$$

\bar{B} is called the Laplace vector. Where it can be found that

- \bar{B} is in the orbital plane because $\bar{h} \bar{B} = 0$.
- \bar{B} is a constant value vector because \bar{B} is an integral constant.
- $k\bar{B}$ always indicates the direction of perigee from the central object for any \bar{r} . Imagine at periapsis.

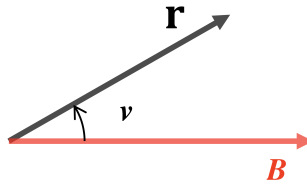


FIGURE 2.5: Coordinate System With \bar{B} as a Reference Direction.

Now that we can make \bar{B} a reference direction, let's look at the shape of the orbit using this. That is, take the scalar product of \bar{B} and \bar{r} .

$$\bar{r}(\dot{\bar{r}} \times \bar{h}) - \mu \frac{\bar{r}\bar{r}}{r} = \bar{r}\bar{B} \quad \therefore \quad h^2 - \mu r = rB \cos v \quad (2.24)$$

Rewritten, it'll be

$$r = \frac{h^2}{\mu + B \cos v} = \frac{\frac{h^2}{\mu}}{1 + \frac{B}{\mu} \cos v} = \frac{p}{1 + e \cos v} = \frac{a(1 - e^2)}{1 + e \cos v} \quad (2.25)$$

The parameter, a , is the semimajor axis and e is the orbit eccentricity. The form of the equation confirms that orbits derived under these assumptions take the shape of the conic sections and is dependent upon e :

- When $e = 0$, the orbit is circular.
- When $0 < e < 1$, the orbit is elliptical.
- When $e = 1$, the orbit is parabolic.
- When $e > 1$, the orbit is hyperbolic.

This is Kepler's first law. However, "elliptical orbit" is extended to "conic curve."

Kepler's Second Law

Remembering expression for the angular momentum vector, \bar{h} , as shown in Equation 2.18. And the expressions for vectors \bar{r} and \bar{v} being,

$$\bar{v} = \frac{dr}{dt} \hat{r} + r \frac{d\theta}{dt} \hat{\theta} \quad (2.26)$$

The expression for \bar{h} is, then:

$$\bar{h} = \bar{r} \times \dot{\bar{r}} = \begin{vmatrix} \hat{r} & \hat{\theta} & \hat{k} \\ r & 0 & 0 \\ \frac{dr}{dt} & r \frac{d\theta}{dt} & 0 \end{vmatrix} = r^2 \frac{d\theta}{dt} \hat{k}$$

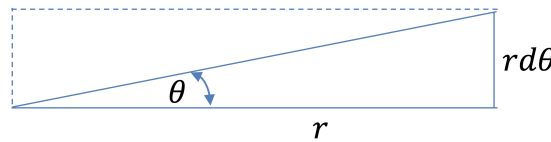


FIGURE 2.6: Coordinate System as a Reference Direction.

So, the magnitude of this vector is constant as is the nature of specific angular momentum.

$$h = |\bar{h}| = r^2 \frac{d\theta}{dt} = \text{constant} \quad (2.27)$$

We also recognize that the area swept out over time is simply one half of the specific angular momentum:

$$\frac{dA}{dt} = \frac{1}{2} h = \frac{1}{2} r^2 \frac{d\theta}{dt} = \text{constant} \quad (2.28)$$

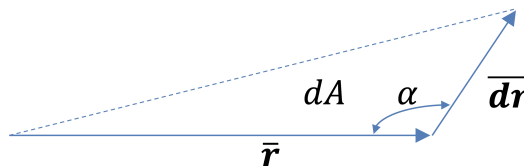


FIGURE 2.7: Coordinate System as a Reference Direction.

Another approach would be,

$$dA = \frac{1}{2} r dr \sin \alpha \quad (2.29)$$

If we let the differential area, dA , be represented as a vector, \bar{dA} , ...

$$\bar{dA} = \frac{1}{2} \bar{r} \times \bar{dr} \quad (2.30)$$

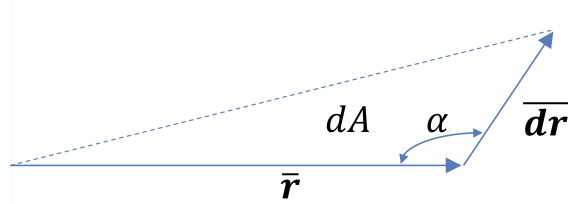


FIGURE 2.8: Coordinate System as a Reference Direction.

With respect to time, differentiate to obtain,

$$\dot{\bar{A}} = \frac{d\bar{A}}{dt} = \frac{1}{2}\bar{r} \times \dot{\bar{r}} \quad (2.31)$$

By differentiating again, you will obtain a vector crossed with itself and vectors pointed in same direction, cancelling each other out. Leaving the area velocity to be constant at $\frac{1}{2}$ of the specific angular momentum.

$$\ddot{\bar{A}} = \frac{d}{dt} \left(\frac{d\bar{A}}{dt} \right) = \frac{1}{2} \frac{d}{dt} (\bar{r} \times \dot{\bar{r}}) = \frac{1}{2} (\dot{\bar{r}} \times \dot{\bar{r}} + \bar{r} \times \ddot{\bar{r}}) = 0 \quad \therefore \quad \frac{d\bar{A}}{dt} = \text{constant} \quad (2.32)$$

Kepler's Third Law

The area of the ellipse is πab . Since the area velocity of the orbital motion is $\frac{d\bar{A}}{dt} = \frac{1}{2}\bar{h}$ from Kepler's second law, therefore, the orbital period is the time to fill the entire area of the ellipse, which is given by:

$$T = \frac{2\pi ab}{\bar{h}} \quad (2.33)$$

Here, since $b = a\sqrt{1 - e^2} = \sqrt{a_p}$ and $|\bar{h}| = \sqrt{\mu p}$,

$$T = \frac{2\pi ab}{\bar{h}} = \frac{2\pi a^{\frac{3}{2}} \sqrt{p}}{\sqrt{\mu p}} = 2\pi \sqrt{\frac{a^3}{\mu}} \quad \therefore \quad T^2 = \left(\frac{4\pi^2}{\mu}\right) a^3 \quad (2.34)$$

The third law states: The square of the period, T of a planet (or spacecraft) is proportional to the cube of its mean distance, a to the sun (or its central body).

COMPARATIVE NUMERICAL STUDY OF DOMINANT PERTURBATION EFFECTS ON VLEO
SATELLITE ORBIT DEGRADATION

Icon	Name	Definition	Remarks	Expression
a	Semimajor Axis	Half the distance from apoapsis to periapsis.	Orbital period and energy depend on orbit size.	$a = \left(\frac{2}{r} - \frac{v^2}{\mu} \right)^{-1}$
e	Eccentricity	Ratio of half the foci separation (c) to the semimajor axis (a)	Closed orbits: $0 \leq e < 1$ Open orbits: $e \geq 1$	$\vec{e} = \frac{\vec{v} \times (\vec{r} \times \vec{v})}{\mu} - \frac{\vec{r}}{r}$ $e = \vec{e} $
i	Inclination	Angle between the orbital plane and equatorial plane, measured counter clockwise at the ascending node	Equatorial: $i = 0^\circ$ or 180° Prograde: $0^\circ \leq i \leq 90^\circ$ Polar: $i = 90^\circ$ Retrograde: $90^\circ < i \leq 180^\circ$	$i = \cos^{-1} \left(\frac{h_z}{ h } \right)$
Ω	Right Ascension of The Ascending Node	Angle, measured eastward, from the vernal equinox to the ascending node	$0^\circ < \Omega \leq 360^\circ$ Undefined when $i = 0^\circ$ or 180° (Equatorial orbit)	$\Omega = \cos^{-1} \left(\frac{n_x}{ \vec{n} } \right)$ if $n_y < 0 \Rightarrow \Omega = 2\pi - \Omega$
ω	Argument of Perigee	Angle, measured in the direction of satellite motion, from the ascending node to perigee	$0^\circ < \omega \leq 360^\circ$ Undefined when $i = 0^\circ, 180^\circ$, or $e = 0$ (Circular orbit)	$\omega = \cos^{-1} \left(\frac{\vec{n} \cdot \vec{e}}{ \vec{n} \vec{e} } \right)$ if $e_z < 0 \Rightarrow \omega = 2\pi - \omega$
v	True Anomaly	Angle, measured in the direction of satellite motion, from perigee to the satellite's location	$0^\circ < v \leq 360^\circ$ Undefined when $e = 0$ (Circular orbit)	$\nu = \cos^{-1} \left(\frac{\vec{e} \cdot \vec{r}}{e r} \right)$ if $\vec{r} \cdot \vec{v} < 0 \Rightarrow \nu = 2\pi - \nu$

TABLE 2.1: Summary of Orbital Elements

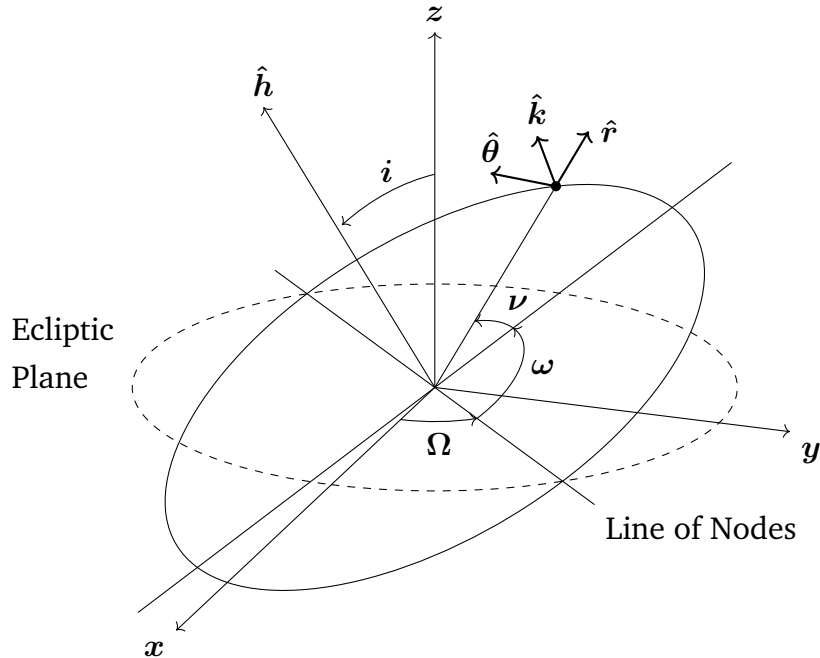


FIGURE 2.9: Classical orbital elements in 3D: showing inclination i , RAAN Ω , argument of periapsis ω , and true anomaly ν .

2.2.2 Orbital Perturbation Theory Basics

Other forces exist that affect the orbits of satellites that will deviate it away from its normal orbital path. Such deviating forces, known as perturbations, would cause the motion to deviate from a Keplerian trajectory. These perturbing forces can be added to the right-hand side of Equation 2.11 as \mathbf{P} , which then yields

$$\ddot{\mathbf{r}} = -\frac{\mu}{r^3} \mathbf{r} + \mathbf{P} \quad (2.35)$$

where \mathbf{p} is the net perturbing acceleration external to that of the two bodies' gravitational attraction. Major perturbing sources include a non-spherical central body, atmospheric, propulsive thrust, solar radiation pressure, and gravitational interactions with other celestial objects.

2.2.3 Fundamentals of Orbital Decay

Orbital decay is commonly referred to as the gradual decrease in altitude of satellites, eventually leading to its re-entry into the atmosphere. All satellites experience orbital decay in varying degrees, and have lifetimes dictated almost entirely by their interaction with perturbation forces. Prediction of such decay rates are of vital importance as they allow for efficient satellite operation, optimization of mission lifespans, and effective space debris management, reducing the risk of collisions and ensuring the long-term sustainability of space activities.

There are two approaches that are commonly employed to address these perturbation forces in detail:

General Perturbation Techniques replace original equations of motion or change in the orbital elements with analytical approximations, capturing essential motion characteristics over a narrow time interval. These techniques provide analytic expressions for Keplerian variables, reflecting orbit size, shape, and orientation. Although computationally economical, they result in truncated approximations, affecting accuracy.

Special Perturbation Techniques (i.e. numerical integration of orbits) where the projected positions and velocities are obtained through numerical approaches that are comprised of datasets, representing values for the positions, velocities and accelerative forces on the bodies of interest at a given time. Numerically integrating the full motion equations inclusive of all necessary perturbing acceleration yields very accurate results, but to the cost of computing time and the gradual build-up of roundoff and errors due to computational approximation.

2.3 Perturbation Forces in VLEO

2.3.1 Atmospheric Drag Effects

Though the Earth's atmospheric density dissipates exponentially with the upper atmosphere of orbit areas, their effect on a satellites' orbit are never void. The

effect that satellites experiences is due to the drag force resulting from its interaction with the smattering air molecules that are present at these altitudes. At orbital speeds, such an effect becomes even more significant when interactions are prolonged, leading to orbital decay or damage due to aerodynamic heating.

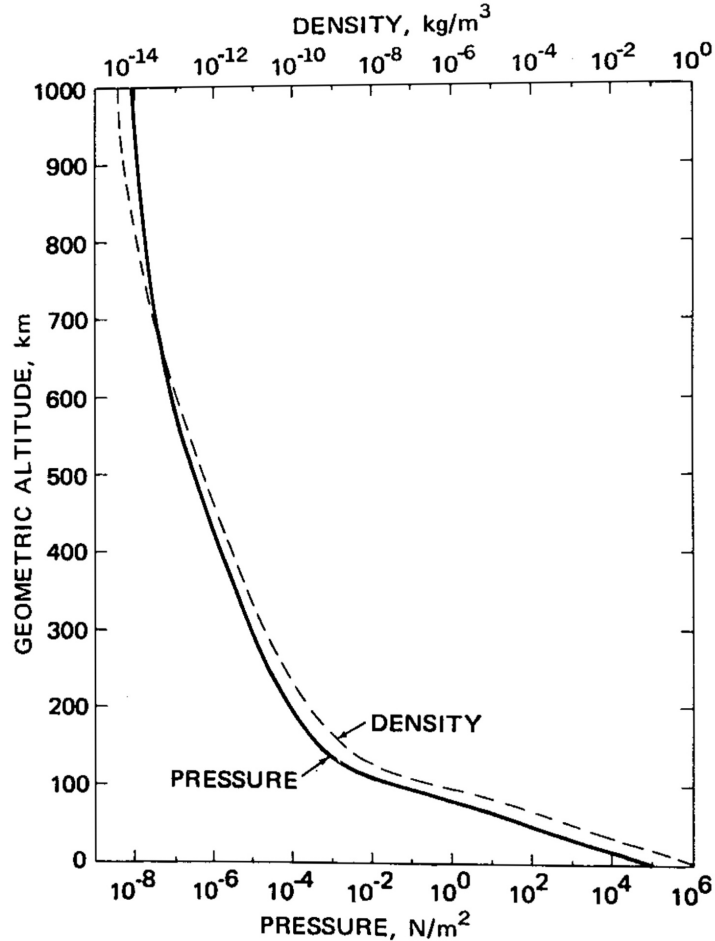


FIGURE 2.10: Total pressure and mass density as a function of geometric altitude, USSA76 [13].

Show in in Figure 2.10 is the variation of atmospheric density according to USSA76, the US Standard Atmosphere 1976. The USSA76 model shows atmospheric density variation from sea level to an altitude of 1000 km.

It is worth noting that according to USSA76, the atmosphere is a spherically symmetric 1000-km-thick gaseous shell surrounding the Earth. Its properties

throughout are steady-state and consistent with a period of moderate solar activity. The hypothetical variation of properties with altitude approximately represents the year-round conditions at midlatitudes averaged over many years. The model provides realistic values of atmospheric density that, however, may not match the actual values at a given place or time.

Drag, which can be defined as inertial atmospheric velocity (\mathbf{v}_{atm}), is in the opposite direction of the inertial velocity of a satellite (\mathbf{v}) and removes energy from the orbit, this results in the satellite velocity relative to the atmosphere defined as:

$$\mathbf{v}_{\text{rel}} = \mathbf{v} - \mathbf{v}_{\text{atm}} \quad (2.36)$$

The inertial atmospheric velocity (\mathbf{v}_{atm}) is dependent upon Earth's angular velocity ($\boldsymbol{\omega}_E$), which is relative to the origin O of the geocentric equatorial frame. This is because the atmosphere rotates with the Earth, and so the relationship is defined as $\mathbf{v}_{\text{rel}} = \boldsymbol{\omega}_E \times \bar{\mathbf{r}}$, where $\bar{\mathbf{r}}$ is the spacecraft position vector. Thus,

$$\mathbf{v}_{\text{rel}} = \mathbf{v} - \boldsymbol{\omega}_E \times \bar{\mathbf{r}} \quad (2.37)$$

Since the drag force \mathbf{D} on an object acts in the direction opposite to the relative velocity vector, we can write that

$$\mathbf{D} = -D\hat{\mathbf{v}}_{\text{rel}} \quad (2.38)$$

and $\hat{\mathbf{v}}_{\text{rel}} = \mathbf{v}_{\text{rel}}/\mathbf{v}_{\text{rel}}$ is the unit vector in the direction of the relative velocity, and the drag force can be defined as

$$D = \frac{1}{2} \rho v_{\text{rel}}^2 C_D A \quad (2.39)$$

- ρ is the atmospheric density at a given altitude;
- A is the frontal area of the spacecraft (the area normal to the relative velocity vector); and
- C_D is the dimensionless drag coefficient.

and if the mass of the spacecraft is m , then the perturbing acceleration due to the drag force is $\mathbf{p} = \mathbf{D}/m$, so that

$$\mathbf{P} = -\frac{1}{2} \rho v_{\text{rel}} \left(\frac{C_D A}{m} \right) \mathbf{v}_{\text{rel}} \quad (2.40)$$

so, when calculating in terms vector quantities, the expression becomes

$$\mathbf{P}_{\text{drag}} = -\frac{1}{2} \rho v_{\text{rel}} \left(\frac{C_D A}{m} \right) \begin{bmatrix} v_x^{\text{rel}} \\ v_y^{\text{rel}} \\ v_z^{\text{rel}} \end{bmatrix} \quad (2.41)$$

2.3.2 Earth's Non-Spherical Gravitational Field (J2-J4 Effects)

The initial approach towards the two-body problem are subject to the assumption of Earth's homogenous mass and spherical symmetry, such assumptions are to be removed when considering the reality of perturbational forces. In actuality, the Earth's mass is not homogenous nor is its shape spherically symmetrical. The Earth's accurate structure, commonly defined as an oblate spheroid, resembles more of a squashed globe. This oblateness is attributed to the Earth's lifelong rotation, subjecting its mass to continual centrifugal forces causes its poles to be flattened and its equator to bulge outward.

Though not spherically symmetric, continuous centrifugal forces allow Earth's shape to be considered as rotationally symmetric. This rotational symmetry allows for prediction of mass distribution, and because gravity is affected by mass and distance, the gravitational potential on a satellite can be predicted. For example, the denser core is closer to the poles, leading to a slightly stronger gravitational pull there compared to the equator. The perturbation of the gravitational potential due Earth oblateness can be denoted as Φ , and when written, this rotationally symmetric perturbation is given by the infinite series

$$\Phi(\bar{r}, \phi) = \frac{\mu}{\bar{r}} \sum_{k=n}^{\infty} J_k \left(\frac{R}{\bar{r}} \right)^k P_k \cos(\phi) \quad (2.42)$$

where

- J_k is the zonal harmonics of the Earth, unique to itself;
- R is the Earth's equatorial radius; and

- P_k is the Legendre polynomials, obtained from a formula derived by French mathematician Olinde Rodrigues (1795–1851);

Zonal harmonics are a subset of spherical harmonics that are symmetric around the planet's axis of rotation. They are characterized by the zonal harmonic coefficients, denoted by J_0 , J_1 , J_2 , J_3 , and so on. However, since J_0 is related to the total mass of the planet, and J_1 is related to the planet's centre of mass, they are typically normalized and J_1 is set to zero because the centre of mass is usually defined as the origin of the coordinate system. As such, for the Earth, the next six zonal harmonics are

$$\begin{array}{ll} J_2 = 0.00108263 & J_5 = -0.20995 \times 10^{-3} J_2 \\ J_3 = -2.33936 \times 10^{-3} J_2 & J_6 = 0.49941 \times 10^{-3} J_2 \\ J_4 = -1.49601 \times 10^{-3} J_2 & J_7 = 0.32547 \times 10^{-3} J_2 \end{array}$$

TABLE 2.2: Zonal Harmonic Coefficients

As seen in Table 2.2, J_2 is so much larger than the other zonal harmonics. Higher-order zonal harmonics (J_3 , J_4 , etc.) also contribute to the overall gravitational field and can cause smaller orbital perturbations. However, their effects are generally much less pronounced than those of J_2 , which even causes changes in the orbital elements, such as the right ascension of the ascending node (RAAN) and the argument of perigee.

Considering this, the focus is only on J_2 's contribution to the gravitational perturbation. In that case, only the relevant Legendre polynomial may be calculated for application, which then yields

$$\Phi(\bar{r}, \phi) = \frac{J_2 \mu}{2r} \left(\frac{R}{r} \right)^2 (3 \cos^2 \phi - 1) \quad (2.43)$$

The perturbation acceleration due to J_2 can be written as

$$a_x = +\frac{3}{2} \frac{J_2 \mu}{r^2} \left(\frac{R}{r} \right)^2 \frac{x}{r} \left[5 \left(\frac{z}{r} \right)^2 - 1 \right] \quad (2.44)$$

$$a_y = +\frac{3}{2} \frac{J_2 \mu}{r^2} \left(\frac{R}{r} \right)^2 \frac{y}{r} \left[5 \left(\frac{z}{r} \right)^2 - 1 \right] \quad (2.45)$$

$$a_z = +\frac{3 J_2 \mu}{2 r^2} \left(\frac{R}{r}\right)^2 \frac{z}{r} \left[5 \left(\frac{z}{r}\right)^2 - 3 \right] \quad (2.46)$$

It is apparent that there is a common multiplier, which allows for a simplified solution in vector form when calculating the total perturbing acceleration \mathbf{P} due to J_2

$$\mathbf{P}_{J_2} = -\frac{3 J_2 \mu}{2 r^2} \left(\frac{R}{r}\right)^2 \begin{bmatrix} \left(1 - 5 \frac{z^2}{r^2}\right) \frac{x}{r} \\ \left(1 - 5 \frac{z^2}{r^2}\right) \frac{y}{r} \\ \left(3 - 5 \frac{z^2}{r^2}\right) \frac{z}{r} \end{bmatrix} \quad (2.47)$$

2.4 Numerical Methods for Orbit Propagation

2.4.1 Overview of Common Numerical Integrators

As brought up before, numerical integration of orbits is a Special Perturbation Technique that yields very accurate results due to its accounting of the full equations of motions and the necessary perturbing accelerations. Cowell's and Encke's methods are two distinct approaches within special perturbations. Cowell's method directly integrates the equations of motion in rectangular coordinates, while Encke's method focuses on the difference between the actual orbit and a reference orbit (often a two-body orbit). Though Encke's method can be more efficient for certain types of orbits, Cowell's method is generally used more frequently than Encke's method for orbit prediction due to its ease of implementation and wider applicability, add to that modern-day computers can meet the method's demand of high computational capability.

Cowell's special perturbation approach directly integrates, step-wise, the equation of motion in Equation 2.35. This yield its 2nd ODE as a set of two 1st order ODEs:

$$\frac{d}{dt} \begin{bmatrix} \bar{r} \\ \bar{v} \end{bmatrix} = \begin{bmatrix} \bar{v} \\ -\mu \frac{\bar{r}}{R^3} + \bar{a}_{\text{total}} \end{bmatrix} \quad (2.48)$$

This is then numerically integrated through various technique, one being the Runge-Kutta method fourth order (RK4) integration scheme. As previously explained, such methods can become inaccurate for long-term numerical studies, computationally expensive, and requires a small step size. That being said, scenarios in VLEO are considered short-term due to rapidly decaying orbits, which finds the method to be adequate.

CHAPTER 3

RESEARCH METHODOLOGY

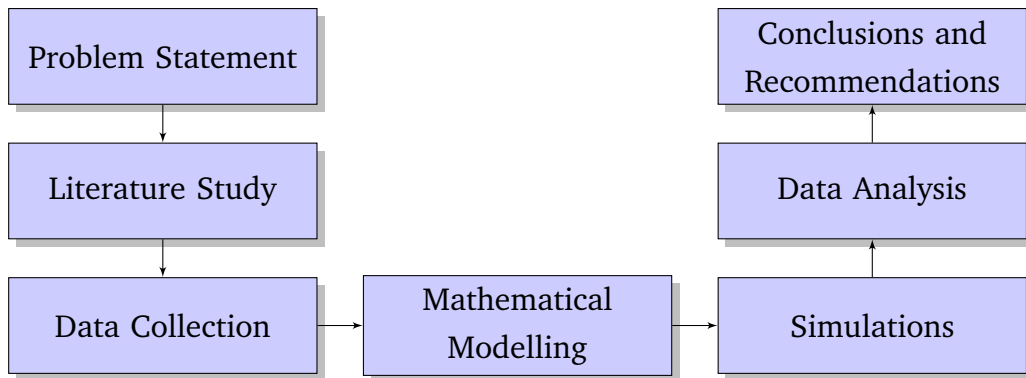


FIGURE 3.1: Research flowchart

3.1 Research Outline

This section will provide a structured outline on the approach taken to conduct the research. Through outlining the processes, methods, and reasoning behind data collection and analysis, the framework will be detailed so as to make the methodology replicable and the findings verifiable. The following is a broad outline of the steps taken

1. Problem Statement

The initial problem rose from the demand of VLEO satellites that will provide superior imaging resolution, lower latency communication, and more frequent Earth observation capabilities, and add to that a potentially lower cost than traditional higher-altitude satellites. As such, the prediction of perturbations in VLEO is also demanded.

2. Literature Study

Various journals, websites, and books that are related to the field of study

were referenced to aid in the research. From those references, was acquired a sufficient knowledge of astrodynamics on orbital mechanics, how satellite's state is represented, and propagation methods. Additionally, an adequate knowledge of orbital perturbations had to be attained as the goal of this research is to analyse and compare the effects of dominant perturbation on VLEO satellite orbit degradation.

3. Programming Language and Tools

The open-source software SCILAB was used for this, specifically the SCILAB 2025.0.0 version that is compatible with Intel-based macOS systems. SCILAB was used to gather data for the research, create mathematical models, propagation simulations.

4. Data Collection

Data collection is crucial for understanding, predicting, and mitigating dominant perturbation forces. The accuracy of simulation is highly dependent on data such as atmospheric density, aerodynamic forces and torques, and space weather conditions.

5. Mathematical Modelling and Simulation

Models for the conversion of orbital elements, numerical integration, propagation of orbits, and mainly the computation of dominant perturbation forces had to be made for the case of this research. They were made using programming tool mentioned before, which was also how the propagation simulation was conducted.

6. Comparative Analysis

The data needed for comparison was gathered using the mathematical and simulations tools prepared. An analysis was derived from comparing between the different and combined perturbations in VLEO which will give insight accurate orbit prediction and attitude control.

3.2 SCILAB Programming Language

SCILAB was chosen for its free and open-source nature, while also reputed for being used by scientists and engineers as a high-level programming language. Being

open source and free, it has no need for licensing costs, and allows for wider accessibility and collaboration. This wide accessibility allowed for the research to utilize a handful of references on the utilization of the language.

3.3 Data Collection

Several external datasets and references were used to construct the perturbation models applied in this study. While basic knowledge of orbital mechanics was obtained from Curtis [14], the mathematical models developed for atmospheric drag and J_2 oblateness required accurate physical and environmental parameters that can only be sourced from established standards and references.

3.3.1 Atmospheric Model Data: USSA76

To model atmospheric drag in low Earth orbit (LEO), this study adopts the **U.S. Standard Atmosphere 1976 (USSA76)** model. This empirical model provides tabulated reference values for atmospheric density and scale height as a function of geometric altitude, ranging from sea level up to 1000 km.

The USSA76 is widely used in orbital mechanics due to its practicality and representativeness of average atmospheric conditions. It describes a globally averaged atmosphere and does not account for local weather or solar activity variations, making it suitable for long-term orbital simulations [14], [15]. The selection of USSA76 is motivated by:

- **Simplicity:** The model enables fast and efficient computation using pre-tabulated data and exponential decay formulas.
- **Relevance:** It is applicable in the orbital regime where atmospheric drag becomes significant but is still amenable to empirical modelling.
- **Widespread Use:** It is a standard in the aerospace industry and academic studies, providing a baseline for analysis and comparison.

For this simulation, atmospheric data from USSA76 is reformatted as a lookup table consisting of 28 geometric altitude entries, each associated with a base density and a corresponding scale height. These values serve as the basis for interpolation in the drag model.

3.3.2 Zonal Harmonics Data: J_2 from Vallado

For modelling the perturbation due to Earth's oblateness, the zonal harmonic coefficient J_2 is adopted. The value of J_2 used in this study is:

$$J_2 = 1.08263 \times 10^{-3}$$

This value, along with Earth's equatorial radius ($R_E = 6378.137$ km), is obtained from Vallado's *Fundamentals of Astrodynamics and Applications* [15].

J_2 is the dominant term in the Earth's gravitational potential expansion and accounts for the flattening of Earth at the poles. It introduces secular changes in the argument of perigee, inclination, and right ascension of the ascending node, which are critical to long-term orbit prediction.

The reasons for selecting Vallado as the reference include:

- **High precision:** The values reported are based on the latest gravity field models.
- **Comprehensive derivation:** The book provides detailed derivations of perturbation effects due to J_2 .
- **Reliability:** Vallado is widely cited in both academic research and operational orbital mechanics software.

The J_2 value is used in the vector-form acceleration expression derived in Equation 12.30 of Curtis, and validated with values reported in Vallado, ensuring consistency across literature sources.

3.4 Mathematical Modelling

3.4.1 Orbital Elements Conversion from State Vectors

To analyse and interpret satellite motion in a more physically meaningful form, the position and velocity state vectors are transformed into Classical Orbital Elements (COEs). This transformation is carried out using a custom function, `coe_from_sv`, which follows Algorithm 4.1 commonly found in orbital mechanics literature.

Function Purpose. The function `coe_from_sv(R, V, μ)` computes the orbital elements from a given position vector \vec{R} and velocity vector \vec{V} , assuming a known gravitational parameter μ . This is essential for propagating orbital motion and for analysing the dynamical effects of perturbations over time.

Input Parameters.

- \vec{R} — Position vector in inertial coordinates (km)
- \vec{V} — Velocity vector in inertial coordinates (km/s)
- μ — Standard gravitational parameter of the central body (km³/s²)

Output. The function returns a 1×7 vector containing the following classical orbital elements:

$$[h, e, \Omega, i, \omega, \theta, a]$$

where:

- h — Specific angular momentum magnitude (km²/s)
- e — Eccentricity (dimensionless)
- Ω — Right Ascension of the Ascending Node (rad)
- i — Inclination (rad)
- ω — Argument of Perigee (rad)
- θ — True Anomaly (rad)
- a — Semi-major axis (km)

Computational Method. The function applies a step-by-step vector analysis:

1. Compute magnitudes of position, velocity, and radial velocity.
2. Calculate the angular momentum vector $\vec{h} = \vec{R} \times \vec{V}$, from which inclination i is derived.
3. Determine the node vector $\vec{N} = \vec{k} \times \vec{h}$ (where \vec{k} is the unit vector in the z-direction), and use it to compute the Right Ascension of the Ascending Node Ω .
4. Calculate the eccentricity vector \vec{e} from the vis-viva relationship.
5. Derive the argument of perigee ω and true anomaly θ using dot and cross product relationships, with proper quadrant checks.

6. Compute the semi-major axis a using the specific mechanical energy relation.

Special conditions, such as circular or equatorial orbits (i.e., $e \approx 0$ or $i \approx 0$), are handled using threshold checks to avoid singularities and ensure numerical stability.

Relevance to This Study. The `coe_from_sv` function is central to post-processing orbital propagation data. By converting Cartesian state vectors back to orbital elements at each simulation timestep, it enables quantitative tracking of perturbation effects (e.g., J_2 oblateness, atmospheric drag) on orbital behaviour. The evolution of COEs over time provides the basis for further analysis and visualization, supporting conclusions regarding orbit stability and mission longevity.

3.4.2 State Vector Conversion from Orbital Elements

To initialize orbital simulations or reconstruct the trajectory from known orbital parameters, the function `sv_from_coe` is employed. It performs the inverse of the `coe_from_sv` transformation, converting Classical Orbital Elements (COEs) back into Cartesian position and velocity vectors in an inertial frame.

Function Purpose. The function `sv_from_coe(coe, μ)` computes the position vector \vec{r} and velocity vector \vec{v} from a set of given orbital elements. It is used primarily to generate initial conditions for orbit propagation routines.

Input Parameters.

- `coe` — A 1×6 vector of orbital elements in the form:

$$[h, e, \Omega, i, \omega, \theta]$$

- μ — Standard gravitational parameter of the central body (km^3/s^2)

Output.

- \vec{r} — Position vector in inertial frame (km)

- \vec{v} — Velocity vector in inertial frame (km/s)

Computational Method. The function constructs the perifocal frame position and velocity vectors \vec{r}_p and \vec{v}_p using standard geometric formulations based on the true anomaly θ . It then transforms these vectors into the inertial frame via three successive rotations:

1. Rotation about the z-axis by $-\omega$
2. Rotation about the x-axis by $-i$
3. Rotation about the z-axis by $-\Omega$

These rotations are implemented using standard 3D transformation matrices. The final inertial frame vectors \vec{r} and \vec{v} are obtained by applying the transpose of the combined rotation matrix to \vec{r}_p and \vec{v}_p .

Relevance to This Study. The `sv_from_coe` function is utilized to generate consistent initial conditions from analytically derived or known orbital elements. It supports the simulation of orbital evolution under various perturbative environments by ensuring accurate and consistent initialization of the state vector.

3.4.3 Atmospheric Density Model: USSA76

To reconstruct a continuous function for atmospheric density from the tabulated USSA76 data, exponential interpolation is used. For each altitude z , the algorithm identifies the corresponding bracketed interval $[h_i, h_{i+1})$ and computes density using:

$$\rho(z) = \rho_i \exp\left(-\frac{z - h_i}{H_i}\right)$$

where:

- ρ_i is the reference density at the base altitude h_i ,
- H_i is the scale height for that interval,
- z is the target altitude.

This method is implemented in the `atmosphere.sce` function used by the propagation routine. For robustness, altitudes beyond the 0–1000 km range are clamped to the nearest endpoint to prevent extrapolation errors.

Adequacy of the 28-Point Resolution:

The 28-point discretization is sufficient for orbital drag modelling. This is because:

- The data is spaced more densely at lower altitudes where density changes rapidly, and more sparsely at higher altitudes where the atmosphere is thinner and changes more gradually.
- The exponential form of interpolation preserves the natural logarithmic decay of atmospheric density, which matches empirical observations [15].
- Comparative plots confirm that the resulting function captures the overall profile of the atmosphere with good fidelity.

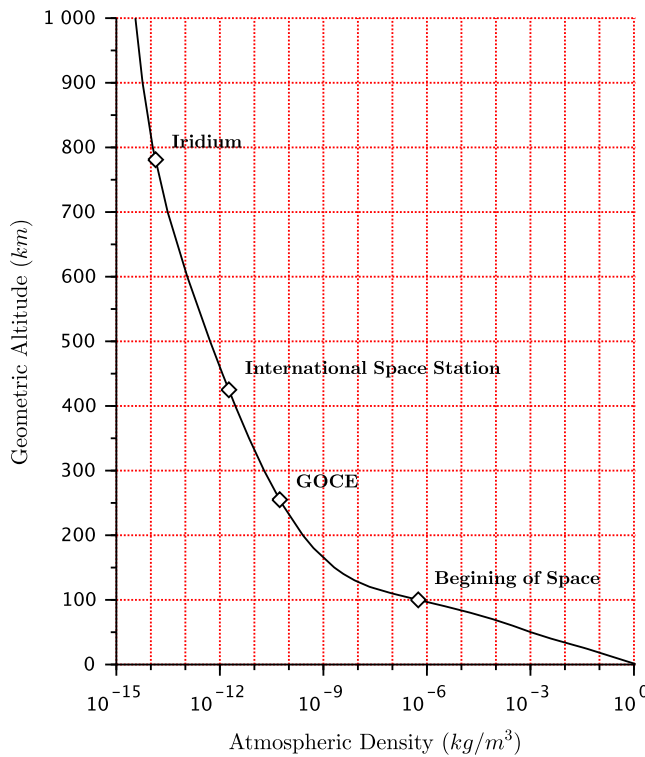


FIGURE 3.2: Interpolated Atmospheric Density Profile from USSA76
(Log Scale)

Figure 3.2 shows the logarithmic density-altitude profile generated from the interpolated function. The shape closely replicates standard atmospheric profiles published in the literature [14], validating the interpolation approach and data resolution.

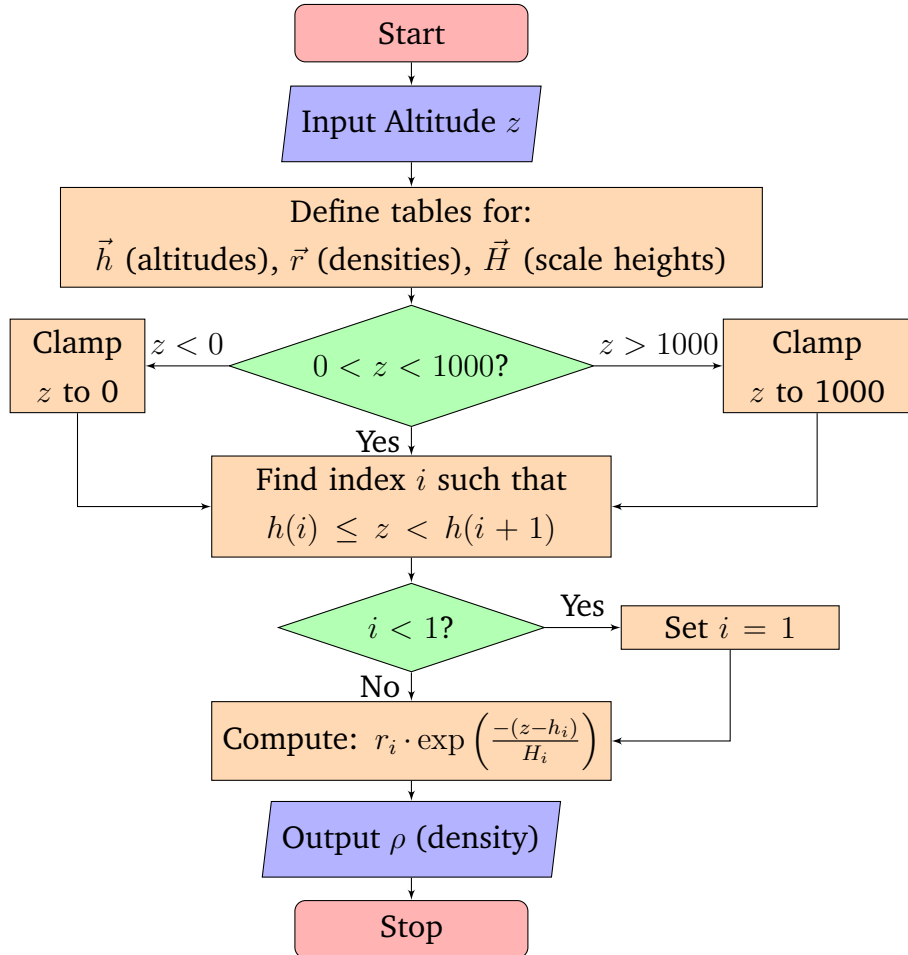


FIGURE 3.3: Atmospheric Density Model: `atmosphere(z)` function flowchart

3.4.4 Custom Fourth-Order Runge–Kutta Integrator

To numerically solve the equations of motion for orbital propagation, a custom fourth-order Runge–Kutta (RK4) integrator was developed in Scilab. This integrator is designed to solve first-order ordinary differential equations (ODEs) of the form:

$$\frac{d\vec{Y}}{dt} = \vec{f}(t, \vec{Y})$$

where \vec{Y} is the state vector comprising position and velocity components, and \vec{f} is a user-defined function representing the derivatives (i.e., acceleration due to forces such as gravity or drag).

State Vector Definition. The initial state vector is constructed as:

$$\vec{Y}_0 = [x_0, y_0, z_0, v_{x0}, v_{y0}, v_{z0}]^T$$

representing the Cartesian position and velocity of the satellite in an inertial frame (units in km and km/s).

Time Configuration. The simulation runs over a user-defined time span $\text{tspan} = [t_0, t_f]$, with a fixed time step h . The RK4 integrator adapts the final step to exactly reach t_f .

Integrator Algorithm. The implemented integrator follows the classical RK4 formulation:

$$\begin{aligned}\vec{k}_1 &= \vec{f}(t_n, \vec{Y}_n) \\ \vec{k}_2 &= \vec{f}\left(t_n + \frac{h}{2}, \vec{Y}_n + \frac{h}{2}\vec{k}_1\right) \\ \vec{k}_3 &= \vec{f}\left(t_n + \frac{h}{2}, \vec{Y}_n + \frac{h}{2}\vec{k}_2\right) \\ \vec{k}_4 &= \vec{f}(t_n + h, \vec{Y}_n + h\vec{k}_3) \\ \vec{Y}_{n+1} &= \vec{Y}_n + \frac{h}{6}(\vec{k}_1 + 2\vec{k}_2 + 2\vec{k}_3 + \vec{k}_4)\end{aligned}$$

This update is performed iteratively until the final time is reached. The time history is stored in `tout`, and the corresponding state vectors in `yout`.

Two-Body Dynamics Example. An example ODE function `two_body_ode(t, Y)` was defined to model the idealized two-body problem:

$$\frac{d^2\vec{r}}{dt^2} = -\frac{\mu\vec{r}}{r^3}$$

where $\mu = 398600 \text{ km}^3/\text{s}^2$ is Earth's gravitational parameter. The function computes position derivatives (velocities) and acceleration due to gravity, returning the full derivative vector $d\vec{Y}/dt$.

Relevance to This Study. This custom integrator forms the computational backbone of the orbital propagation framework used in this research. It enables flexible testing of:

- Different perturbation models (e.g., J_2 , atmospheric drag)
- Various orbit types (e.g., circular, elliptical, inclined)
- Sensitivity analyses through consistent step-by-step numerical integration

By building the integrator in-house, complete control over the solver behaviour is maintained, allowing easier adaptation, debugging, and modification for future perturbation extensions.

3.4.5 Perturbation Models for Orbital Propagation

To study the influence of various perturbative forces on satellite motion, three rate functions were developed in Scilab: `drag`, `j2rates`, and `dragj2`. These extend the classical two-body model by incorporating atmospheric drag and Earth's oblateness (J_2) effects. Each function returns the time derivative of the state vector $\vec{f} = [\vec{r}; \vec{v}]$, allowing them to be used directly in numerical integrators.

Atmospheric Drag Model (drag)

The drag function models atmospheric drag using the following formulation:

$$\vec{a}_{\text{drag}} = -\frac{1}{2} \frac{C_D A}{m} \rho v_{\text{rel}}^2 \hat{v}_{\text{rel}}$$

where:

- C_D — drag coefficient
- A — cross-sectional area (m^2)
- m — satellite mass (kg)
- ρ — atmospheric density at altitude, from the USSA76 model
- v_{rel} — relative velocity w.r.t. the rotating atmosphere
- \hat{v}_{rel} — unit vector in the direction of relative velocity

Relative velocity is computed by subtracting Earth's rotation vector $\vec{\omega}_E \times \vec{r}$ from the satellite's inertial velocity \vec{v} . Drag acceleration is added to the gravitational acceleration $\vec{a}_{\text{grav}} = -\mu \vec{r} / r^3$, forming the total acceleration:

$$\vec{a} = \vec{a}_{\text{grav}} + \vec{a}_{\text{drag}}$$

J_2 Perturbation Model (j2rates)

The Earth's oblateness (zonal harmonic J_2) introduces secular and periodic variations in the orbit, especially in the right ascension of the ascending node (Ω) and argument of perigee (ω). The J_2 perturbing acceleration is computed from the formerly formulated Equation 2.47 adapted from Curtis [14]:

$$\vec{a}_{J_2} = -\frac{3}{2} J_2 \frac{\mu R_E^2}{r^4} \begin{bmatrix} (1 - 5\frac{z^2}{r^2}) \frac{x}{r} \\ (1 - 5\frac{z^2}{r^2}) \frac{y}{r} \\ (3 - 5\frac{z^2}{r^2}) \frac{z}{r} \end{bmatrix}$$

This term is added to the gravitational acceleration to yield:

$$\vec{a} = \vec{a}_{\text{grav}} + \vec{a}_{J_2}$$

Combined Drag and J_2 Model (dragj2)

To capture more realistic orbital evolution in low Earth orbit (LEO), both drag and J_2 perturbations can be combined. The `dragj2` function implements:

$$\vec{a} = \vec{a}_{\text{grav}} + \vec{a}_{\text{drag}} + \vec{a}_{J_2}$$

This modular design allows one to isolate or compound the perturbative forces for comparative studies. By modifying components within the `dragj2` function, direct quantification of each perturbation's influence can be performed on quantities such as:

- Semimajor axis decay
- Nodal precession rate ($\dot{\Omega}$)
- Argument of perigee rotation ($\dot{\omega}$)
- Eccentricity growth or damping

Relevance to This Study. These rate functions form the core of the dynamic model used in orbital propagation. By systematically applying them in numerical simulations using the custom RK4 integrator, the time evolution of orbital elements under isolated and combined perturbations can be analysed in detail. This forms the basis for sensitivity analysis, orbital lifetime estimation, and mission planning for spacecraft operating in LEO.

3.5 Simulation & Comparative Analysis

The numerical simulations in this study were carried out using a custom-built Runge–Kutta 4 (RK4) integrator in Scilab. The simulation framework integrates the satellite's state vector over time using the perturbation models discussed in the previous sections. Each simulation case is initialized with a specific set of Classical Orbital Elements (COEs), which are converted into inertial position and velocity vectors via the `sv_from_coe` function.

3.5.1 Simulation Configuration

The simulation function is defined in a modular structure, allowing perturbation effects (e.g., J_2 and drag) to be toggled as needed. An example wrapper function is shown below:

```

1  function dydt = dragj2_wrapper(t, f)
2  dydt = dragj2(t, f, params);
3  endfunction

```

LISTING 3.1: Wrapper function for integrator input

This wrapper was necessary to pass a ‘params’ structure into the perturbation model, a design choice made to maintain flexibility and consistency between simulation runs.

Each simulation begins by defining the initial orbital elements:

- h_0 , e_0 , Ω_0 , i_0 , ω_0 , and θ_0 as the classical orbital elements.
- The COEs are then converted into a state vector $\vec{f}_0 = [\vec{r}_0; \vec{v}_0]$.
- Integration is performed over a time span of approximately 16 days using a fixed step size.

To avoid numerical issues and error accumulation in Scilab (especially when performing back-to-back simulations), each case is fully reset, including the initial state vector and integration time. This prevents memory or function leakage across successive runs.

3.5.2 Orbital Element Extraction

After each integration step, the resulting state vector is transformed back into COEs using the `coe_from_sv` function. This enables post-processing of each orbital parameter over time:

$$\begin{aligned}
 \vec{f}(t) &= [\vec{r}(t); \vec{v}(t)] \\
 &\Downarrow \\
 \vec{\text{COE}}(t) &= [h(t), e(t), \Omega(t), i(t), \omega(t), \theta(t), a(t)]
 \end{aligned}$$

From the derived semimajor axis a and eccentricity e , the perigee and apogee altitudes relative to Earth's surface are also computed:

$$r_p = a(1 - e) - R_E \quad r_a = a(1 + e) - R_E$$

These orbital parameters are stored in time-tagged arrays for each case, enabling direct comparison of orbital evolution under varying conditions.

3.5.3 Orbit-Based Reframing of Data

To provide a different way of presenting the secular and periodic changes in orbital elements, the simulation data can be reframed using orbit completion as a frame of reference instead. This is done by tracking the cumulative change in true anomaly $\theta(t)$, the angular position of the satellite in its orbit.

Starting by computing the instantaneous orbital period $T(t)$ at each integration point, a cumulative angular counter is maintained to detect full orbit cycles.

By consecutively comparing true anomaly values $\theta(t)$ and compensating for irregularities at $360^\circ \rightarrow 0^\circ$ completions, the code accrues angular motion:

$$\Delta\theta_k = \begin{cases} \theta_k - \theta_{k-1}, & \text{if } |\theta_k - \theta_{k-1}| < 180^\circ \\ \theta_k - \theta_{k-1} \pm 360^\circ, & \text{otherwise} \end{cases}$$

Each time the calculated angle surpasses an integer multiple of 360° , the orbit counter is added on to. Using the example semimajor axis, the matched values of a and T will be recorded each time the counter is increased. This continues until the last timestep, where a fractional orbit will then be computed as:

$$N_{\text{orbits}} = \frac{\sum \Delta\theta_k}{360^\circ}$$

This rearranging of data allows for the study of long-term trends per completed orbit, rather than per unit time, which can be more objective in the context of perturbation-induced drift. The T and orbit number N are preserved for plotting and comparison, forming the new independent variable basis for attitude evolution that can be adapted for all the orbital elements.

3.5.4 Comparative Analysis Approach

The analysis focuses primarily on classical orbital elements, as they provide a more intuitive understanding of:

- Orbital size and shape — via semimajor axis a and eccentricity e
- Orientation in space — through right ascension of the ascending node (Ω), inclination (i), and argument of perigee (ω)
- Position within orbit — true anomaly (θ)

By comparing the time evolution of these elements across different inclination scenarios or perturbation models, the specific effects of drag and J_2 can be quantified. This also provides insight into orbit decay rates, nodal precession, and other long-term dynamical behaviour.

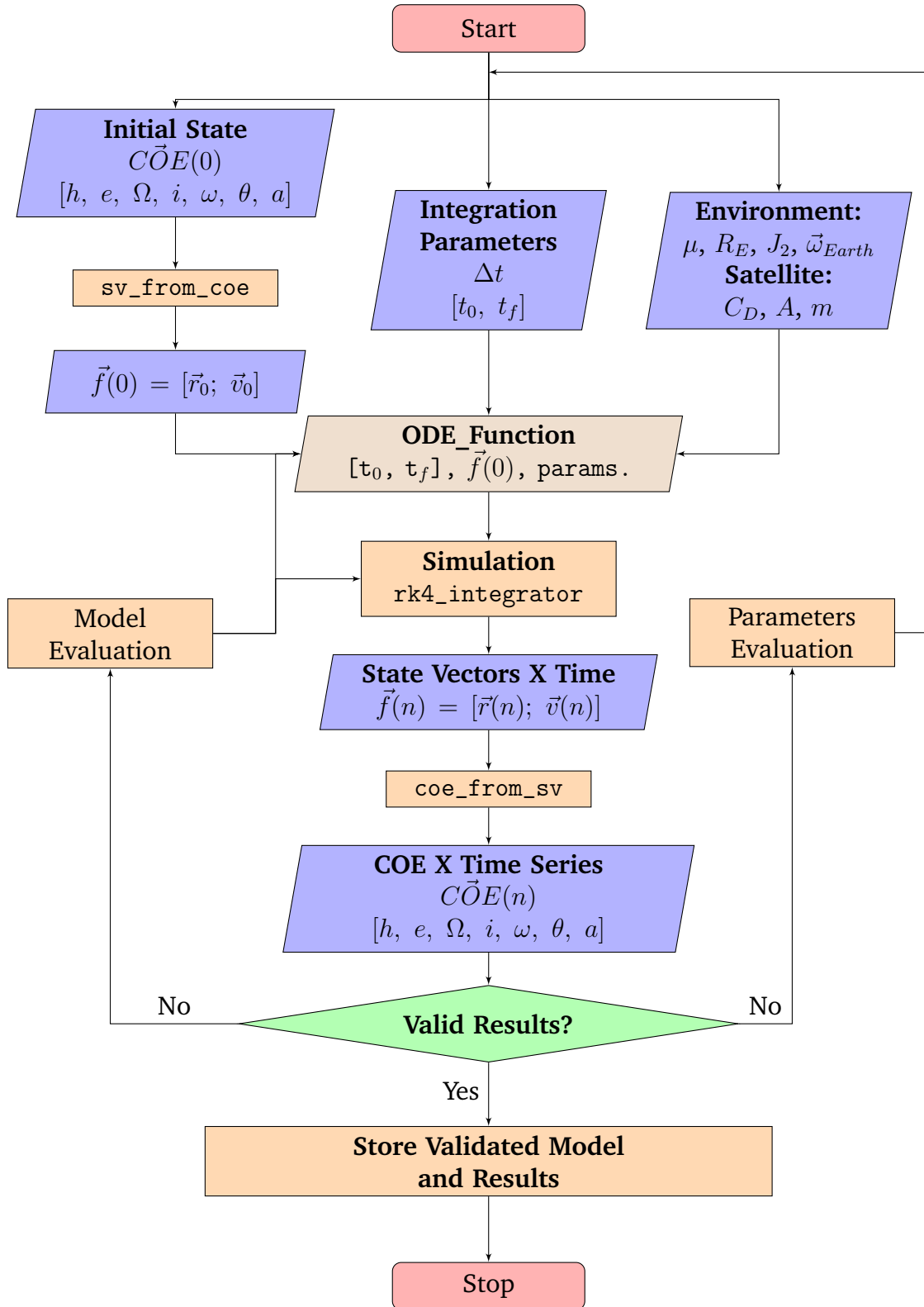


FIGURE 3.4: Workflow of Simulations

CHAPTER 4

RESULTS AND DISCUSSIONS

4.1 Verification of Two-Body Restricted Simulation

Parameters	Values		Unit
	Initial	Final	
Semimajor Axis (a)	6678.1726	6678.17	km
Eccentricity (e)	0.015	0.015	—
Inclination(i)	10	10	deg
Right Ascension of the Ascending Node (Ω)	339.94	339.94	deg
Argument of Perigee (ω)	58	58.0005	deg
True Anomaly (ν)	332	298.179	deg
Orbital Period (P)	90.520393	90.5204	min
Revolutions Completed ($rev.$)	0	15.9	—

TABLE 4.1: Initial and final orbital parameters of the satellite obtained from a two-body restricted simulation.

The research called for verification of the Two-Body Restricted simulation, as it is dependent on the custom-built integrator that back-boned the research. In accordance with the two-body problem theory, an unchanging result signifies that the simulation is correctly modeling the idealized, unperturbed motion of two bodies under gravity, free from external influences or numerical errors. The final values in Table 4.1 are obtained from the final parameters correspond to the last simulated orbital state.

Figure 4.1 shows all of the classical orbital elements' variation over the span of 24 hours with a 30-second integration step. Following the theory of Kepler's

Second Law, θ oscillates between 0 and 360 degrees, reflecting the body's movement around its orbit. A full cycle of this oscillation corresponds to one completed orbit. The true anomaly's fluctuating nature is due to the varying orbital speed, which is faster at perigee and slower at apogee.

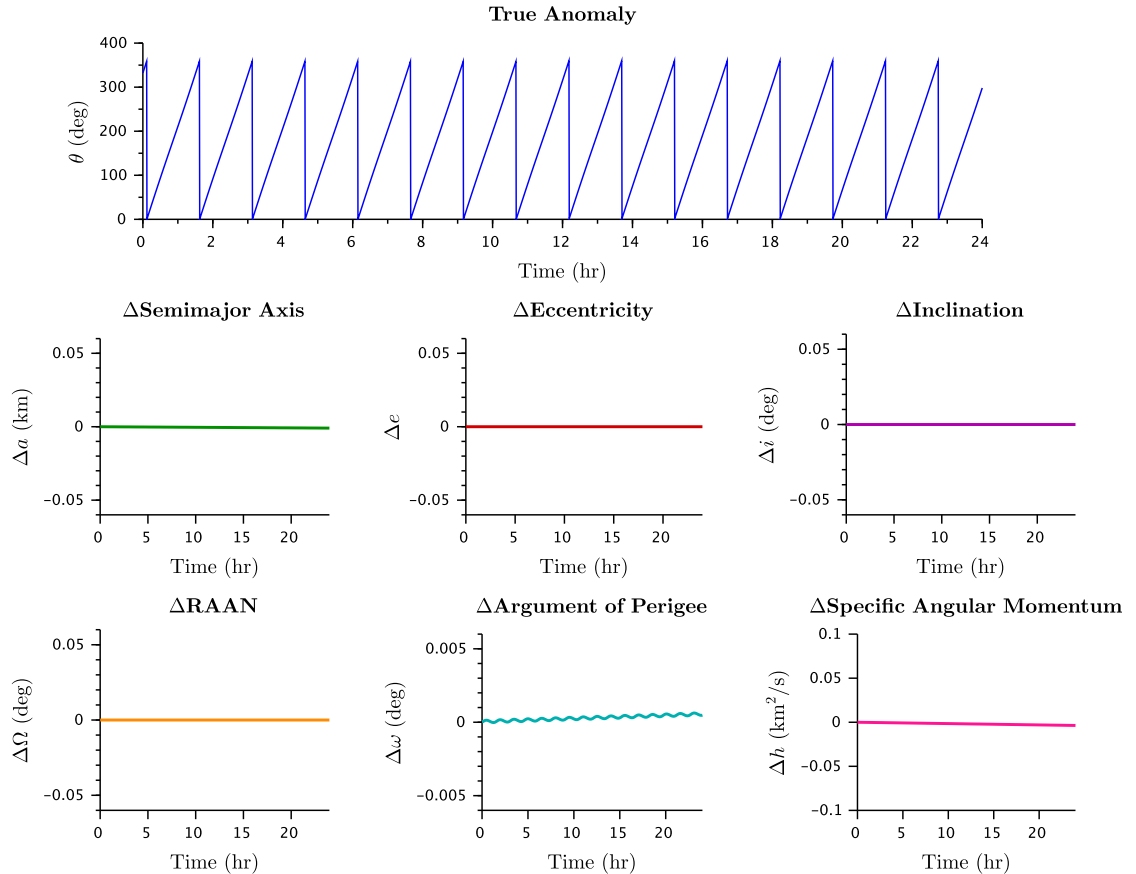


FIGURE 4.1: Two-Body Restricted Orbital Elements' Variation Over Time.

From the observation of Figure 4.1, alone the remaining orbital elements appears to remain unchanged. However, by further observation on the final extracted parameters, there are indications of minor changes. Changes in eccentricity (e), inclination (i), and right ascension of the ascending node (Ω) were found to be negligible over the 24-hour period, with variations on the order of machine precision. In contrast, measurable differences were found in semimajor axis (a),

orbital period (P), argument of perigee (ω), and specific angular momentum (h).

The percentage changes in these quantities are calculated as follows:

$$\Delta a = \frac{6678.17 - 6678.1726}{6678.1726} \times 100 \approx -3.895 \times 10^{-5}\%$$

$$\Delta P = \frac{90.5204 - 90.520393}{90.520393} \times 100 \approx 7.735 \times 10^{-6}\%$$

$$\Delta h = \frac{51588 - 51587.990}{51587.990} \times 100 \approx 1.937 \times 10^{-5}\%$$

Due to the secular nature of the perturbation affecting the argument of perigee, it is more appropriate to express its rate of change per hour:

$$\Delta \omega = \frac{58.000482 - 58}{24} = 2.008 \times 10^{-2} \text{ deg/h}$$

It can be perceived that these minor variations merely reflect the inherent properties of the orbit, like slight adjustments in orientation or shape, rather than significant deviations caused by external forces or errors in the simulation. Then again, seemingly minor random changes in these elements during simulations are often indicative of a numerical artifact, rather than a real physical effect. These artifacts can be attributed towards the limitations of numerical methods used to solve the equations of motion.

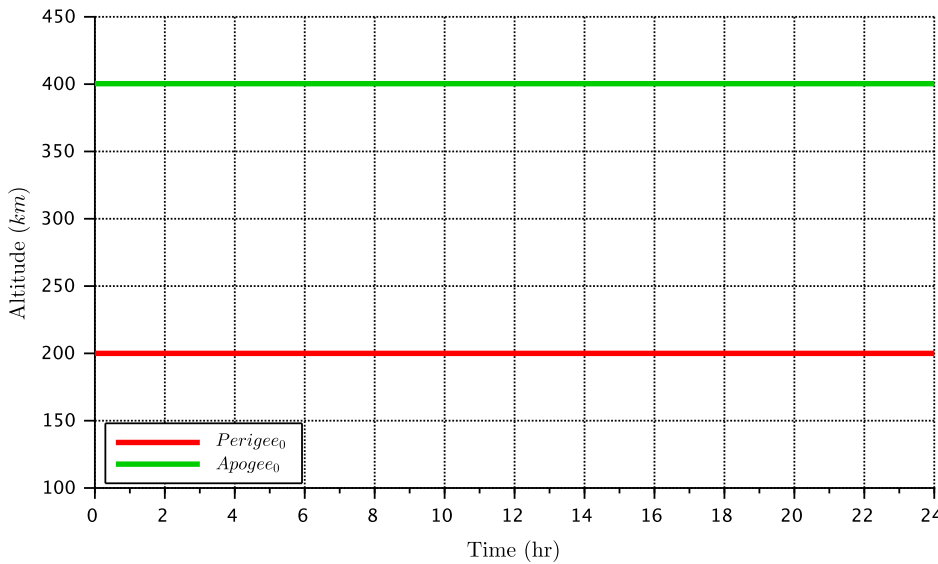


FIGURE 4.2: Altitude variation of a VLEO satellite in Two-Body restricted simulation.

4.2 VLEO Satellites Affected by Dominant Perturbation

The perturbations examined for this study are atmospheric drag and J_2 , as they significantly influence a satellite's behavior. J_2 perturbation is generally considered more dominant than atmospheric drag, however, it is important to acknowledge how the manner in which these perturbations affect an orbit is different. Atmospheric drag generally leads to a more significant and noticeable orbital decay in an orbit. J_2 mainly affects the orientation of an orbit, noticeable through changes in orbital elements over a period of time.

To visualize this, a VLEO satellite affected by atmospheric drag and J_2 , respectively, is taken into consideration in a 20-day period. It small spherical earth satellite has a diameter of 1 m , a drag coefficient of $C_D = 1.5$ and a mass of 100 kg . Utilizing the same parameters in Table 4.1 and using the 1976 US Standard Atmosphere rotating with the earth, Cowell's method is employed for propagation. The two orbits obtained will be plotted distinctly, with the apogee and perigee of both orbits plotted.

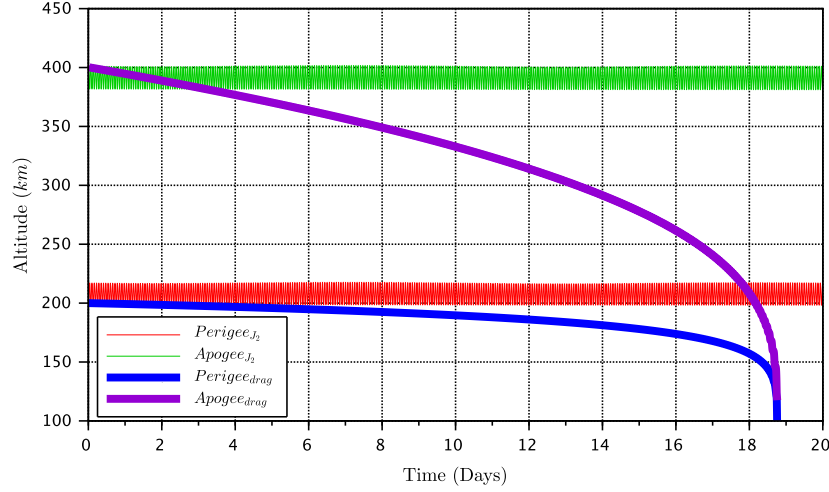


FIGURE 4.3: Altitude variation of a VLEO satellite due to atmospheric drag and J_2 perturbation, respectively.

From the solution, shown in Figure 4.3, it can be observed that exclusively under aerodynamic drag, the satellite experiences significant orbital decay leading to re-entry within 19 days. Considering this and how VLEO satellites aim to operate below 300 kilometers to leverage the benefits of closer proximity to Earth, further examination of how both perturbations can affect orbital elements will have similar propagation periods. Figure 4.3 also shows that under J_2 perturbation, the satellite remains in orbit though its altitude begins oscillating.

Params.	Initial Values	Final Values			Unit
		J_2	Drag	$J_2 +$ Drag	
a	6678.1726	6677.49	6478.18	6478.11	km
e	0.015	0.0124288	0.00260927	0.00289822	—
i	10	9.99533	9.99541	9.98427	deg
Ω	339.94	172.164	339.937	202.398	deg
ω	58	26.6835	322.134	22.9422	deg
ν	332	202.297	218.542	246.809	deg
P	90.520393	90.5065	86.4848	86.4834	min
$rev.$	0	318.63971	300.68484	256.76336	—

TABLE 4.2: Initial and final orbital parameters of a small spherical VLEO satellite under various perturbations.

4.2.1 VLEO Satellites Affected by J_2 Perturbation

To further understand how the orbit's shape, size, and orientation evolve due to this specific perturbing force, it is important to analyze the change in its Keplerian elements over time. Table 4.3 shows the Keplerian elements of the orbit converted from the last recorded state vector at the end of the 20 day period.

Qty.	Value	Unit
a	6676.64	km
e	0.0125442	—
i	9.99254	deg
Ω	172.118	deg
ω	25.8229	deg
ν	215.123	deg
P	90.49	min
$rev.$	318.67	—

TABLE 4.3: Final Orbital Parameters of Satellite under J_2 Perturbation

As predicted, the right ascension of the node and the argument of perigee exhibit the most changes throughout the period. The rate of change can then be visualized by plotting these elements over time, shown in Figures 4.4 and 4.5.

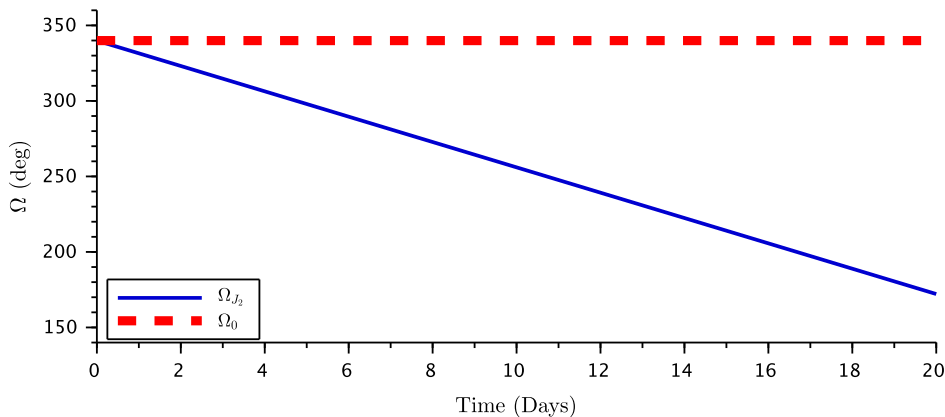


FIGURE 4.4: Variation of the RAAN of a LEO due to J_2 perturbation.

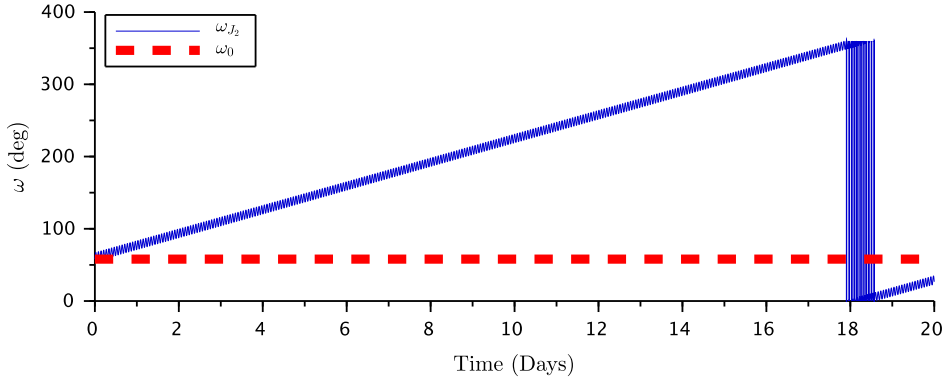


FIGURE 4.5: Variation of the argument of perigee of a LEO due to J_2 perturbation.

In this particular orbit, the RAAN decreases whereas the argument of perigee increases. The plots show that both parameters have either a straight line or secular variation on which a small or short-periodic variation is inflicted. Decrease in the node angle Ω with time is called regression of the node, whereas the increase of argument of perigee ω with time is called the advance of perigee. An approximation of the average values of the slopes of the curves can be simply found by dividing the difference between the final and initial values, which yields

$$\Delta\Omega = -0.345 \text{ deg/h}$$

$$\Delta\omega = 0.75 \text{ deg/h}$$

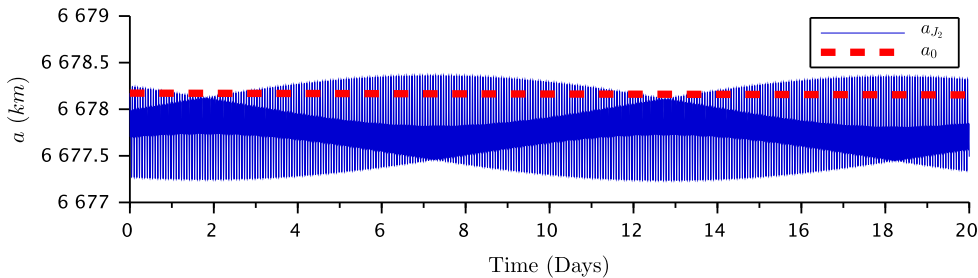


FIGURE 4.6: Variation of the semi-major axis of a VLEO due to J_2 perturbation.

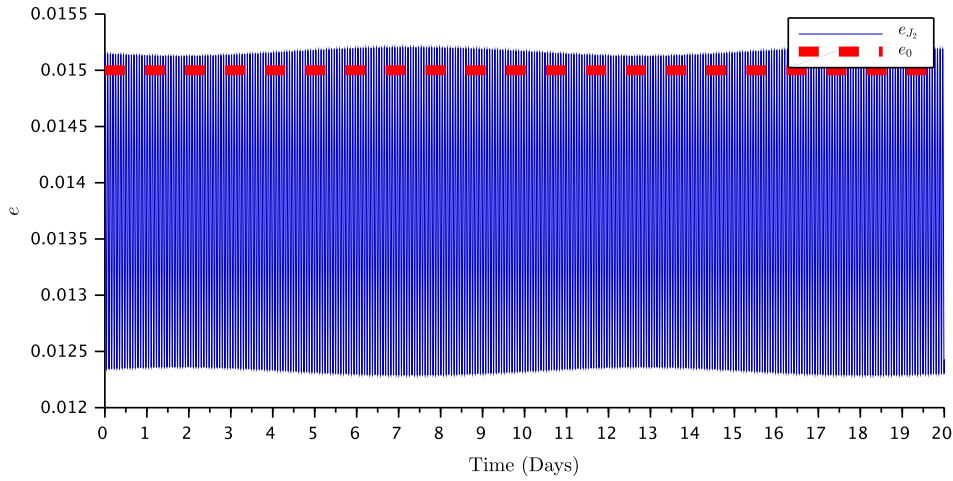


FIGURE 4.7: Variation of the eccentricity of a LEO due to J_2 perturbation.

While zonal harmonics affect the elements similarly, Figure 4.7 is the most clearly that shows another form of beat period appearing due to the zonal harmonics. Interactions between short-periodic and long-periodic variations creates a high-frequency oscillation with an amplitude that oscillates at the long-periodic frequency. This effect is described in Figure 4.8.

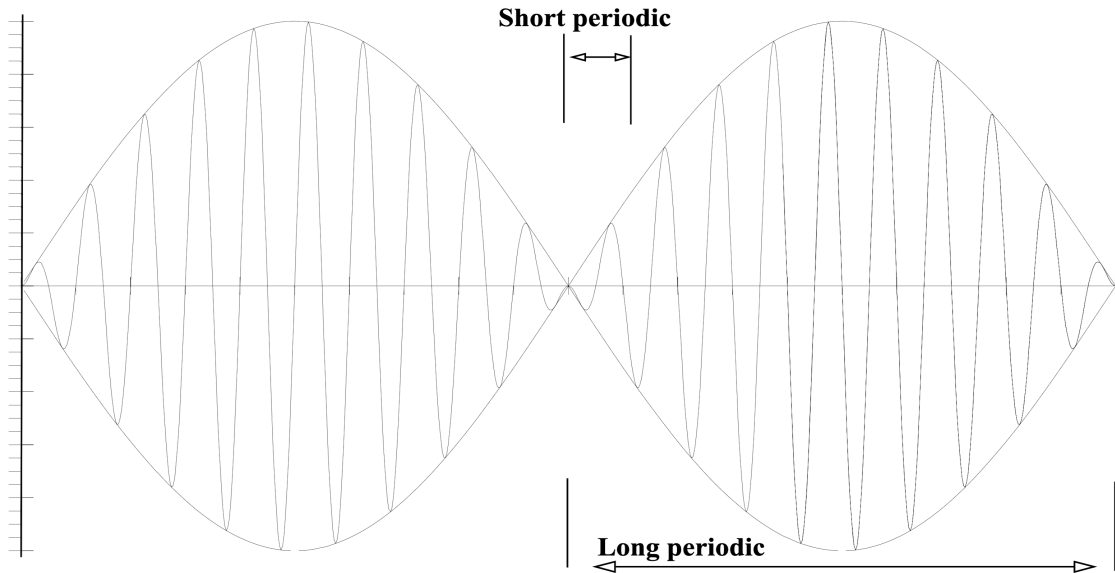


FIGURE 4.8: Long/short periodic beat period from zonal harmonics
[15]

4.2.2 VLEO Satellites Affected by Atmospheric Drag

As drag causes the satellites altitude to decay, the Keplerian elements in Table 4.4 are extracted from the last state vector before reentry, as shown with the semimajor axis having a value of 6478.18 km (roughly 100 km altitude).

Qty.	Value	Unit
a	6478.18	km
e	0.00260927	—
i	9.99541	deg
Ω	339.937	deg
ω	322.134	deg
ν	218.542	deg
T	86.48	min
$rev.$	300.68	—

TABLE 4.4: Final Orbital Parameters of Satellite under Atmospheric Drag Perturbation

The results show how the effects of dominant perturbations vary, as drag primarily causes a decrease in altitude and in eccentricity. Figure 4.9 shows the eccentricity nearing zero, confirmed by Figure 4.3 showing the apogee approaching perigee, due to the drag forces are stronger at higher altitudes than at lower altitudes.

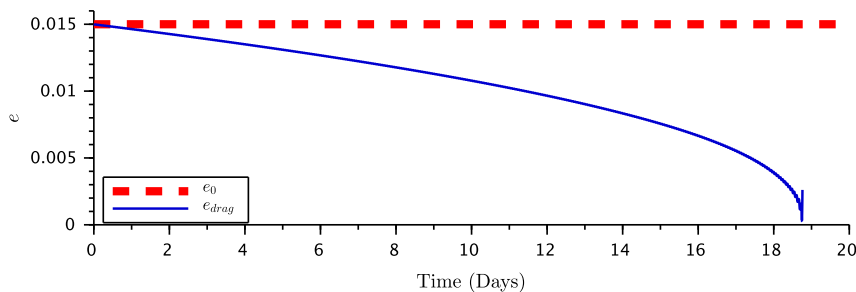


FIGURE 4.9: Variation of the eccentricity of a LEO due to atmospheric drag.

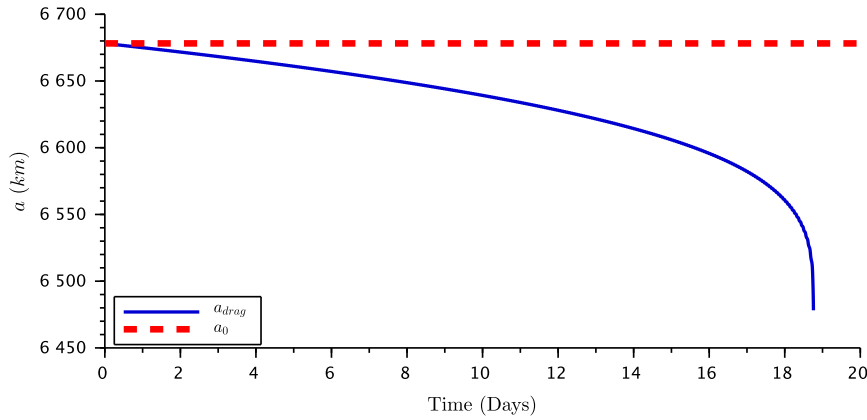


FIGURE 4.10: Variation of the semi-major axis of a VLEO due to atmospheric drag.

The decrease of semi-major axis is shown in Figure 4.10, where the last value shown is ~ 6478 km. This confirms the last recorded position corresponds to an altitude of approximately 100 km, as the average radius of the Earth is approximately ~ 6378 km. It can be taken as the orbit radius as at the same time, eccentricity becomes near zero, indicating a near-circular orbit.

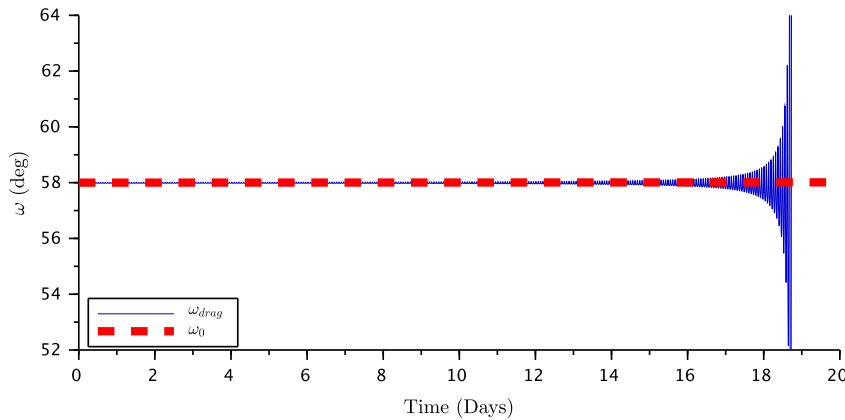


FIGURE 4.11: Variation of the argument of perigee of a LEO due to atmospheric drag.

Aside from the effect of on the semimajor axis and eccentricity, perturbation is also seen in other orbital elements. As shown in Figure 4.11 where as altitude rapidly decays, the location of the perigee will shift, causing the argument of perigee to increasingly oscillate.

4.2.3 Atmospheric Drag + J_2 Perturbed Simulation

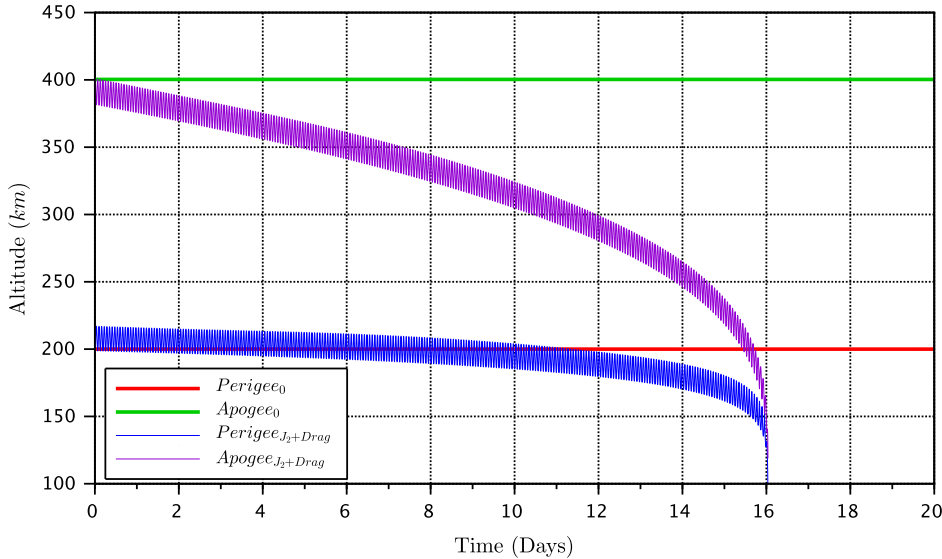


FIGURE 4.12: Altitude variation of a VLEO satellite due to atmospheric drag + J_2 perturbation.

The interaction between two dominant perturbations was verified to affect the satellite's orbit. Figure 4.12 shows combined decay and oscillations, while Table 4.5 confirms long-term and accelerated drift of Keplerian elements, apart from inclination, from their initial value.

Qty.	Value	Unit
a	6478.11	km
e	0.00289822	—
i	9.98427	deg
Ω	202.398	deg
ω	22.9422	deg
ν	246.809	deg
T	86.48	min
$rev.$	256.7	—

TABLE 4.5: Final Orbital Parameters of Satellite under Atmospheric Drag + J_2 Perturbation

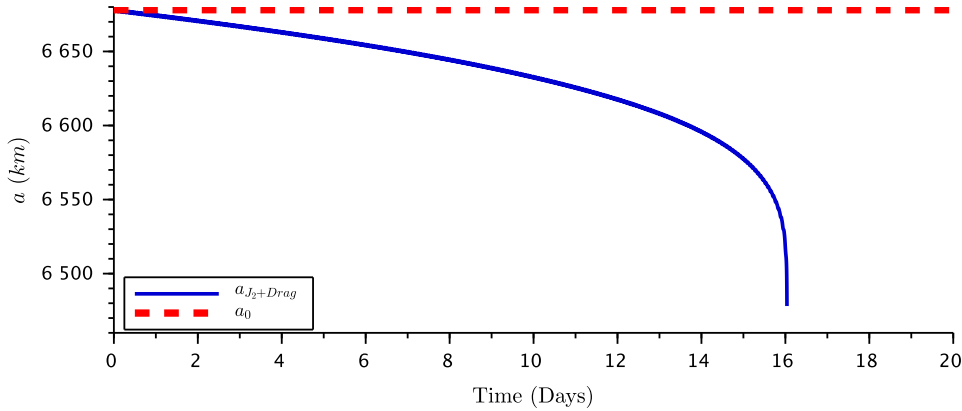


FIGURE 4.13: Variation of the semi-major axis of a VLEO due to atmospheric drag + J_2 Perturbation.

A compounded effect is shown in Figure 4.13, where the same satellite now affected by both forces simultaneously decays to 100 km in 16 days, almost 3 days earlier than if it were subjected only to atmospheric drag. Even though the variation of a only appears to be decay, minor oscillations positioning the satellite at lower altitude would expose it to higher atmospheric density.

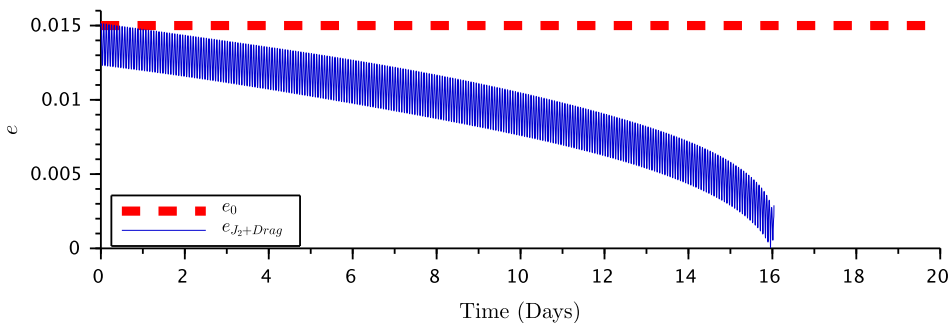


FIGURE 4.14: Variation of the eccentricity of a LEO due to atmospheric drag + J_2 Perturbation.

Figure 4.14 most clearly illustrates compounding the perturbations causes complex behaviour. With the eccentricity over time experiencing significant oscillation and increase/decrease.

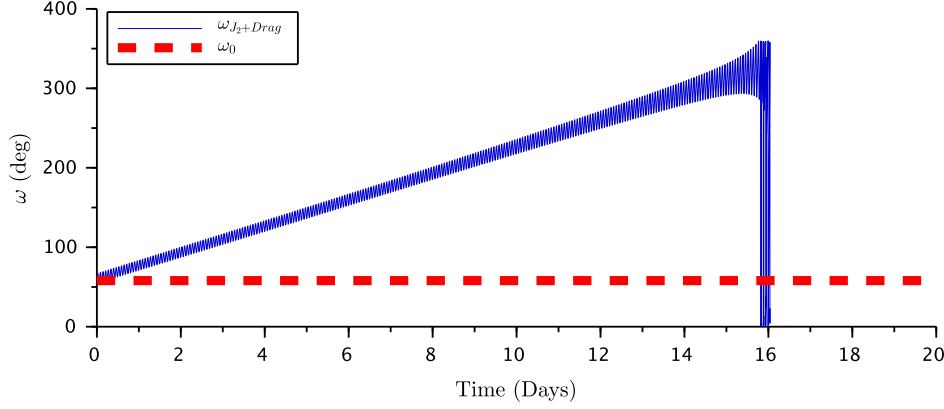


FIGURE 4.15: Variation of the argument of perigee of a LEO due to atmospheric drag + J_2 Perturbation.

Figure 4.15 show that the argument of perigee and the RAAN still increase. The precession of ω is compounded by shifting of the perigee during decay, increasing the oscillations in its amplitude.

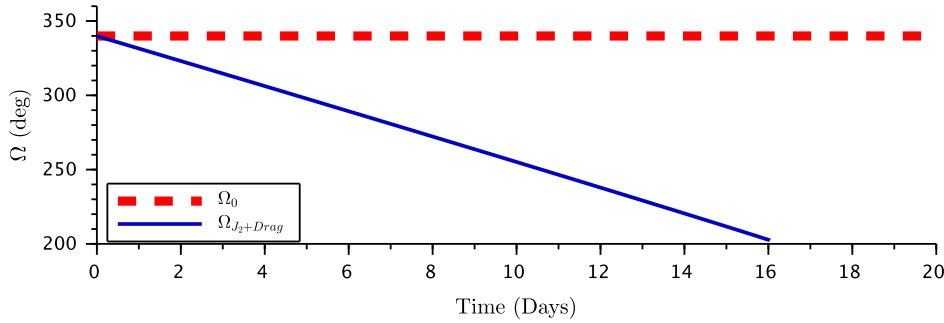


FIGURE 4.16: RAAN regression due to atmospheric drag + J_2 Perturbation.

As seen in Figure 4.4, atmospheric drag, while decaying the orbit, has a less significant direct impact on RAAN compared to the J_2 perturbation. As such, in analysing RAAN precession, the effect of J_2 is the dominant factor considered.

4.3 Variation of Initial Orbital Parameters

In any research, variation can be crucial to understanding the applicability of findings and the potential impact of various factors. In perturbation studies, variation of initial orbital parameters can help to better understand how different starting points affect the behavior of an orbit under various perturbing forces.

4.3.1 Variation of Initial Orbital Parameters – i

The magnitude of J_2 effect on a satellite's orientation is dependent on the angle between the orbital plane and the Earth's equator, its inclination. To demonstrate this and verify the effect of earth oblateness, the parameters in [4.1](#) will be utilized with varying the inclination of the orbit to see its influence.

Simulation With J_2 Perturbation Model

Table [4.6](#) shows the final orbital parameters of the satellite after a short-term propagation (16 days). The varying inclinations are in increments of 20° after the lowest inclination at 10° and the last being 90° , with the satellite undergoing a polar orbit.

Params.	Final Values				
	$i = 10^\circ$	$i = 30^\circ$	$i = 50^\circ$	$i = 70^\circ$	$i = 90^\circ$
a (km)	6677.14	6678.51	6679.448	6668.02	6681.42
e	0.0145059	0.0141767	0.014228	0.0158782	0.0146707
i (deg)	9.9891	30.0073	50.0068	69.9846	90
Ω (deg)	205.671	221.89	252.399	293.387	339.94
ω (deg)	318.841	242.529	127.832	30.1503	347.069
ν (deg)	306.587	284.296	248.438	214.304	205.445
T (min)	90.49	90.52	90.54	90.31	90.58
$rev.$	254.91	254.85	254.75	254.66	254.63

TABLE 4.6: Final orbital parameters after a 16-day propagation under J_2 perturbation. Initial parameters are listed in Table [4.1](#).

From the extracted final orbital parameters, the most significant changes are observed in the right ascension of the ascending node (Ω) and the argument of perigee (ω). Using the initial and final values, the nodal regression rate $\dot{\Omega}$ [deg/day] and perigee rotation rate $\dot{\omega}$ [deg/day] are obtained and compared against analytical predictions from general perturbation (GP) theory [16], as shown in Table 4.7.

The GP expressions for J_2 -induced precession are:

$$\dot{\Omega}_{J_2} = -2.06474 \times 10^{14} \cdot a^{-7/2} \cdot \cos(i_{\text{rad}}) \cdot (1 - e^2)^{-2}$$

$$\dot{\omega}_{J_2} = 1.03237 \times 10^{14} \cdot a^{-7/2} \cdot (4 - 5 \cdot \sin^2(i_{\text{rad}})) \cdot (1 - e^2)^{-2}$$

As predicted, a polar orbit ($i = 90^\circ$) shows no RAAN regression over the simulation period, while other inclinations exhibit precession rates consistent with theoretical expectations. Minor deviations between calculated and simulated values arise from the numerical integration capturing additional dynamical effects beyond the GP assumptions.

Inclination (i)	Precession Rates [deg/day]			
	Nodal Regression ($\dot{\Omega}$)		Perigee Rotation ($\dot{\omega}$)	
	GP Theory	Simulation	GP Theory	Simulation
10°	-8.358	-8.39	+16.334	+16.23
30°	-7.350	-7.38	+11.670	+11.53
50°	-5.455	-5.48	+4.334	+4.36
70°	-2.903	-2.91	-1.762	-1.74
90°	0.000	0.00	-4.244	-4.43

TABLE 4.7: Comparison of J_2 -induced precession rates from GP theory and numerical simulation over a 16-day period.

From Table 4.7, the agreement between GP theory and numerical simulation is evident across all inclinations, with differences within a few hundredths of a degree per day, primarily due to the numerical integration capturing effects beyond the idealised J_2 model. As expected, polar orbits ($i = 90^\circ$) exhibit no nodal regression, while lower inclinations experience progressively larger magnitudes.

For the perigee rotation rate $\dot{\omega}$, both analytical and simulated results indicate a sign change between $i = 50^\circ$ and $i = 70^\circ$, marking a transition from prograde to retrograde rotation. This implies the existence of a “critical inclination” in this range where $\dot{\omega}$ is zero or near zero, a condition that can be exploited in mission design to maintain a fixed argument of perigee without active control.

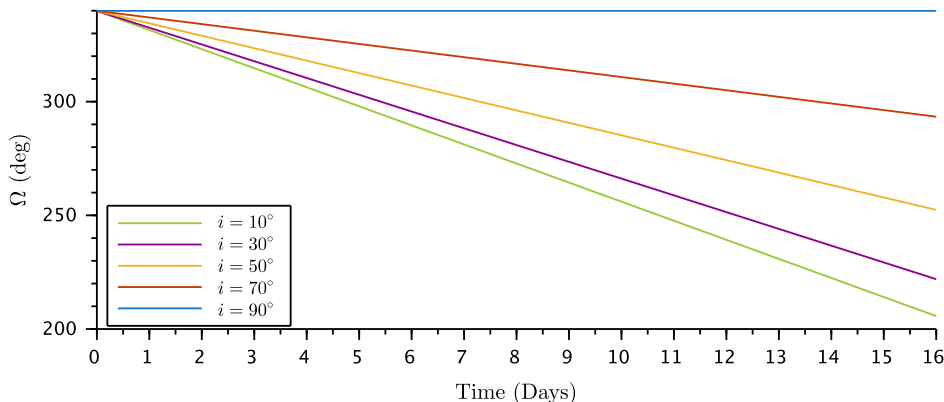


FIGURE 4.17: Variation of the RAAN of a VLEO due to J_2 perturbation for different inclinations.

The nodal regression rate $\dot{\Omega}$ are further confirmed by both the data in Figure 4.17, where it is confirmation that the simulation consider satellites traveling much closer to the equatorial bulge during their orbits are pulled more by it.

Figure 4.18 more clearly visualize that there is an unconsidered i between 50° and 70° , from which deviation will generally lead to a faster rotation of the perigee. Using GP-derived rate of change, we can find the i where the perigee remaines fixed, which is 63.43° .

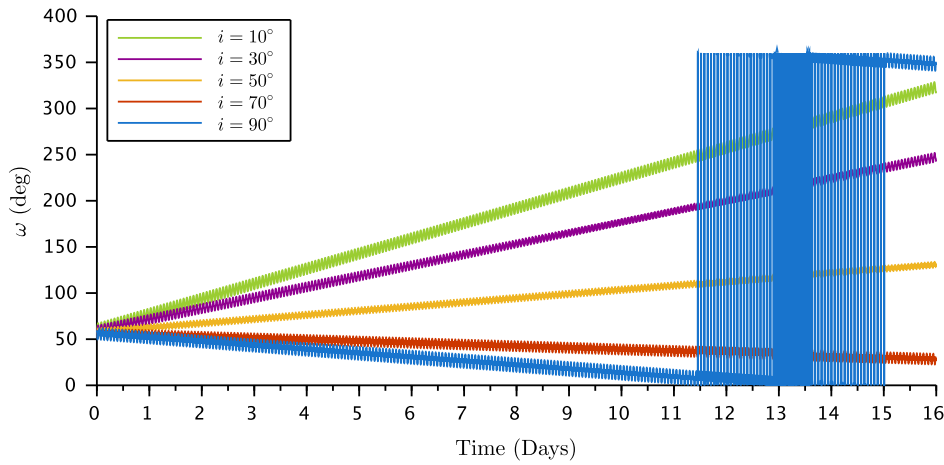


FIGURE 4.18: Variation of the argument of perigee of a VLEO due to J_2 perturbation for different inclinations.

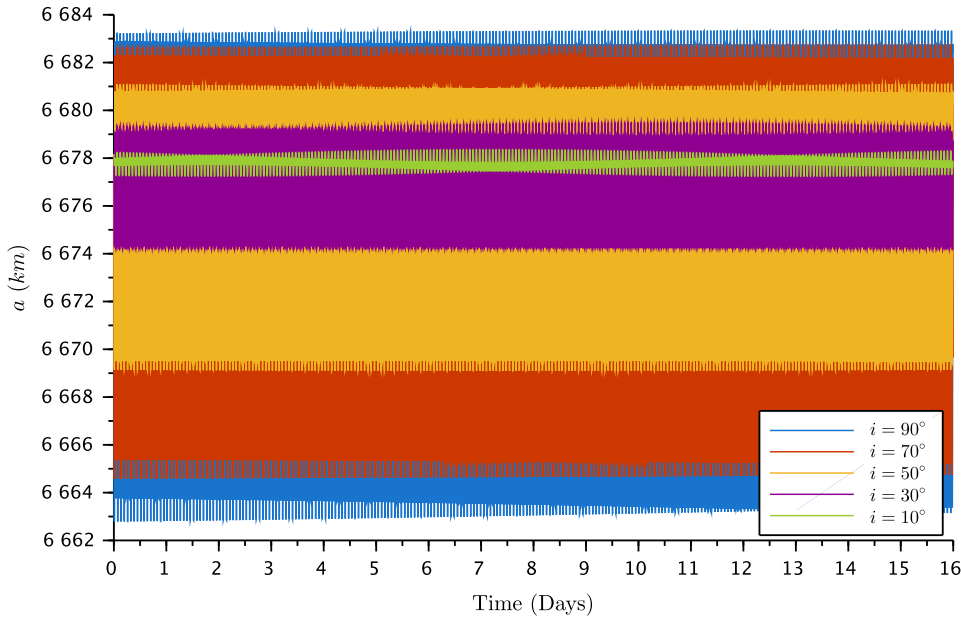


FIGURE 4.19: Variation of the semi-major axis of a VLEO due to J_2 perturbation for different inclinations.

While lower i will intensify the effect that J_2 has on Ω and ω , the opposite seems to be for its effect on a . As seen in Figure 4.19, higher i orbits experience more significant oscillations in their a due to the J_2 effect. This reflects that polar orbits pass over the regions of Earth's oblateness most significantly.

Passing over the Earth's poles and equatorial bulge on each revolution, causes these orbits to experience the most variations in their orbital altitude. With each decreasing i , the oscillations decrease, due to their orbits also furthering from the maximum and minimum radius of the Earth. As a sanity check, it can be seen that maximum oscillations of the polar orbit are roughly 20 km, this corresponds with the earth's equatorial radius being 21 km larger than the polar's.

This also reflects the increased sensitivity of orbital energy variations at higher i , even though the average (secular) value of a is not directly affected in simplified J_2 theory. The numerical simulation captures these short-period variations that become more significant as inclination increases.

Simulation With Drag + J_2 Perturbation Model

Qty.	$i = 10^\circ$	$i = 30^\circ$	$i = 50^\circ$	$i = 70^\circ$	$i = 90^\circ$	Unit
a	6478.11	6478.47	6478.55	6478.06	6478.29	km
e	0.002898	0.002449	0.002958	0.0026835	0.002642	—
i	9.98427	29.9608	49.9596	69.9551	89.9711	deg
Ω	202.398	216.111	245.669	288.934	339.922	deg
ω	22.9422	17.7226	183.389	264.299	199.94	deg
ν	246.809	237.057	237.101	190.651	212.146	deg
T	86.48	86.49	86.49	86.482	86.487	min
$rev.$	256.76	262.73	270.73	274.60	269.66	—

TABLE 4.8: Final Orbital Parameters of Satellite Cases with Varying i under Atmospheric Drag + J_2 Perturbation.

The final orbital parameters obtained from simulations incorporating both J_2 perturbation and atmospheric drag for various inclinations are presented in Table 4.8. All simulations were conducted until orbital decay, defined by the semi-major axis reducing to near the edge of space. The decay of the semi-major axis is as depicted in Figure 4.20.

Atmospheric drag causes a continuous reduction in the semi-major axis for all inclination cases. Across the board, the final semi-major axis values converge to around 6478 km, representing a 200 km loss from the initial value (6678 km).

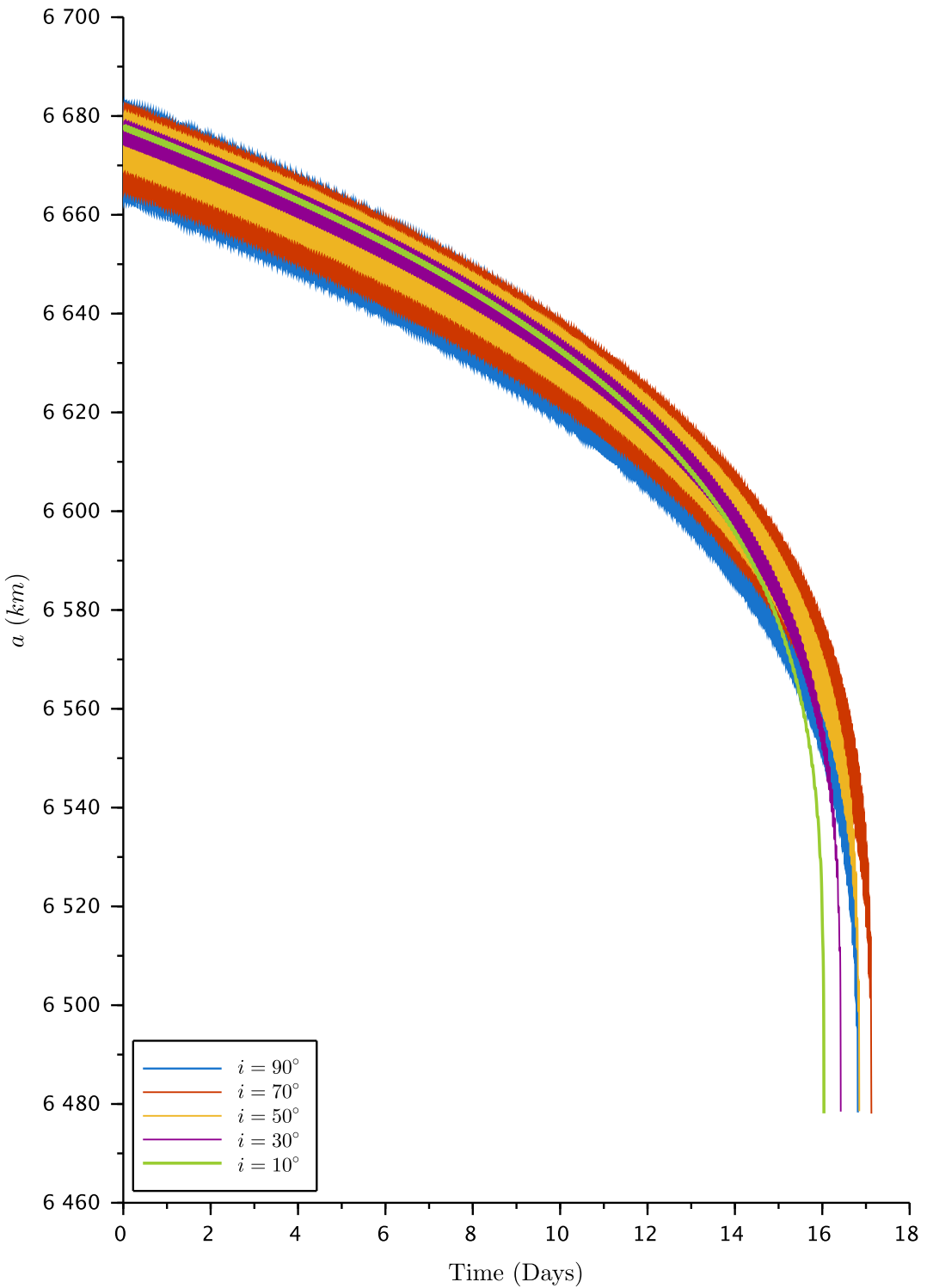


FIGURE 4.20: Variation of the semi-major axis of a VLEO due to drag + J_2 perturbation for different inclinations.

Correspondingly, the orbital period reduces from about 90.5 minutes in the J_2 -only cases to approximately 86.5 minutes under drag influence. This contraction is consistent with the expected outcome of drag dissipating orbital energy.

Decay durations (i.e., time until deorbit) slightly vary with inclination:

- Fastest decay occurs at $i = 10^\circ$ (16.04 days),
- Slowest at $i = 70^\circ$ (17.12 days),
- Interestingly, polar orbit ($i = 90^\circ$) decays faster than 70° , indicating a fluctuating trend.

In contrast to the J_2 -only results in Table 4.6 where eccentricity remains relatively stable (0.014–0.016), the inclusion of drag leads to rapid eccentricity damping, with final values dropping to 0.0025–0.003. This confirms that the simulation still demonstrates drag’s strong tendency to circularize the orbit over time, reducing the variations in perigee/apogee altitudes.

The secular variations of RAAN (Ω) and argument of perigee (ω) persist under the combined perturbations. However, the final values differ slightly from the J_2 -only case, hinting that drag indirectly alters the precession rate by modifying orbital size and velocity. Still, the dominant cause of their evolution remains J_2 .

Interestingly, the total number of revolutions until decay is higher in the drag-affected cases. This is because, although the mission duration remains roughly constant (16–17 days), the orbital period is shorter due to decay, allowing for more frequent orbits. For example, the $i = 70^\circ$ case completes 274 revolutions, compared to 254 in the J_2 -only scenario.

Relevance of Findings. The findings of this section highlight the significant role of J_2 in shaping orbital behavior within VLEO. The numerical findings reveal key inclination-dependent effects: nodal regression ($\dot{\Omega}$) decreases with inclination, while perigee rotation ($\dot{\omega}$) shows a turning point at a critical inclination, where ω would theoretically remain fixed.

The combined effects of J_2 and atmospheric drag demonstrate how these perturbations collectively reduce orbital altitude, circularize eccentricity, and continue to drive secular changes in Ω and ω . Although atmospheric drag causes orbital decay, the inclination-dependent J_2 effects remain clearly observable throughout the mission lifespan.

These perturbative behaviors must be considered in Earth observation (EO) mission design due to the high cost of launches and the importance of orbital maintenance over extended mission durations. From an engineering perspective, several actionable insights arise for EO mission designers:

- **Orbital Lifetime vs. Inclination:** The decay time varies slightly across inclinations, with the shortest observed at 10° (16.04 days) and the longest at 70° (17.12 days). The irregular trend, such as the faster decay at 90° than 70° , suggests that orbital lifetime is not linearly correlated with inclination, due to complex interactions between drag exposure and precession effects. Selecting inclinations with slightly extended lifespans (e.g., 70°) may or may not benefit missions requiring frequent access without rapid orbital degradation.
- **Eccentricity Damping for Imaging Stability:** A stable eccentricity is important for consistent EO imaging. As drag strongly damps e , an extremely low eccentricity would minimize altitude variability and provide ground track repeatability. However, circular orbits tend to decay faster than an elliptical because the drag force is more consistently applied at all points in a circular orbit. The unequal distribution of drag force in an elliptical orbits, due to the significantly thicker atmosphere at the perigee than at the apogee, tends to delay the decay process.
- **Coverage vs. Decay Trade-off:** Polar orbits ($i \approx 90^\circ$) exhibit the strongest semi-major axis oscillations due to frequent traversal over the equatorial bulge and poles. While beneficial for global coverage, these orbits demand more robust altitude control and orbit maintenance planning as they decay more quickly than certain mid-inclination orbits (e.g., 70°), due to increased drag exposure over high latitudes. Therefore, mission planners must balance the coverage benefits of high inclinations with the associated fuel or design requirements to sustain altitude.

- **Selection of Inclination:** For EO missions requiring consistent ground coverage and stable perigee location (e.g., SAR imaging or repeated passes over a target), an inclination near the critical 63.43° offers minimized perigee drift, reducing the need for corrective maneuvers.
- **Stability Consideration:** Lower inclination orbits experience stronger J_2 -induced RAAN regression and perigee rotation. While useful for certain types of precessing orbits, such dynamic behavior can affect long-term pointing stability and may require additional station keeping. Conversely, higher inclination orbits undergo less nodal regression but are more prone to semi-major axis oscillations due to Earth's oblateness. If regional coverage allows, selecting a mid-inclination orbit (e.g., around 63.43° where $\dot{\omega} \approx 0$) offers a balance between dynamic stability and minimal secular drift, potentially reducing control effort over mission duration.

In summary, even under drag, RAAN and perigee precession remain governed by J_2 , emphasizing that inclination still critically affects long-term orbital geometry. Though, for small EO satellites where cost constraints limit maneuvering capacity, the moderate inclinations (e.g., $50\text{--}70^\circ$) offer a promising trade-off between regional coverage, stability, and orbital lifetime. Engineers designing multi-satellite constellations or repeat-pass missions must carefully choose inclinations that align RAAN and ω behaviors with desired ground track evolution.

4.3.2 Variation of Initial Parameters – a

Concurrent with the simulation of earth oblateness' effect, prediction of atmospheric drag is as crucial in better orbit determination. The effect this perturbative force of drag can vary with altitude, as such the effect this perturbative force has can vary with and orbits semimajor-axis (a). As the a decreases, the orbit gets closer to the Earth, leading to increased atmospheric density and, consequently, higher drag. The same goes for when a increases, so will the atmospheric density decrease.

The following simulations will focus on the variation of initial a . Table 4.9 sets out three cases where a value are varied by 50 km , increasing and decreasing from the initial parameters at 4.1. The varying values of a are selected so as to limit the satellite to within VLEO origin. The rest of the parameters will follow the initial case.

Qty.	Case 1	Case 2	Case 3	Unit
a	6628.17	6678.17	6728.17	km
e	0.015	0.015	0.015	—
i	10	10	10	deg
Ω	339.94	339.94	339.94	deg
ω	58	58	58	deg
θ	332	332	332	deg
T	89.50	90.52	91.53	min

TABLE 4.9: Initial Orbital Parameters of Satellite Cases with Varying Semimajor Axis (a).

Simulation With Drag Perturbation Model

Qty.	Case 1	Case 2	Case 3	Unit
a	6478.06	6478.43	6478.02	km
e	0.00204912	0.00258213	0.00246919	—
i	9.99724	9.99542	9.99438	deg
Ω	339.933	339.937	339.935	deg
ω	265.47	322.088	229.587	deg
ν	206.778	218.571	224.343	deg
T	86.48	86.48	86.48	min
$rev.$	42.65	300.68492	1192.701	—

TABLE 4.10: Final Orbital Parameters of Satellite Cases with Varying a under Atmospheric Drag Perturbation.

The final orbital parameters for each case after atmospheric drag perturbation are presented in Table 4.10.

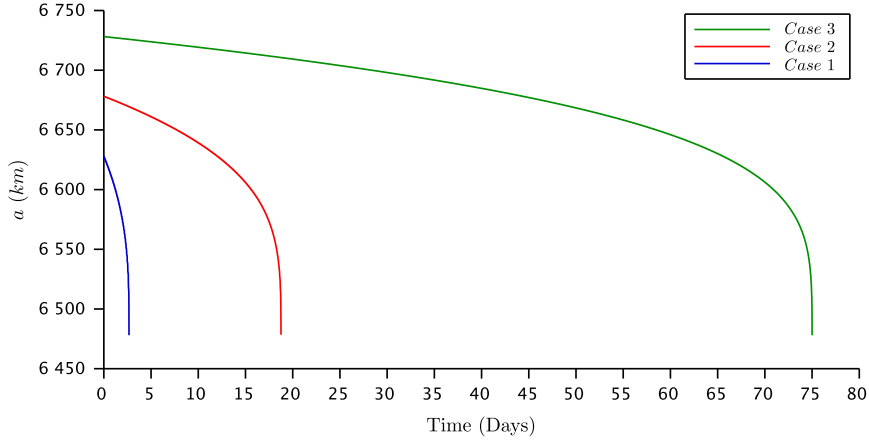


FIGURE 4.21: Variation of the semi-major axis of a VLEO due to atmospheric drag perturbation for different a .

The corresponding orbital lifetimes before complete decay are approximately: Case 1 – 2.5 days, Case 2 – 18 days, and Case 3 – 75 days. These results are plotted in Figures 4.21 and 4.22. Notably, Figure 4.22 reframes the evolution of the semimajor axis in terms of completed orbital revolutions rather than time. Case 1, starting at the lowest altitude, exhibits the fastest orbital decay. A useful sanity check is observed between Case 2 and Case 3, where the curves show like-behavior after their altitudes fall below 200 km, indicating convergence in drag-induced dynamics.

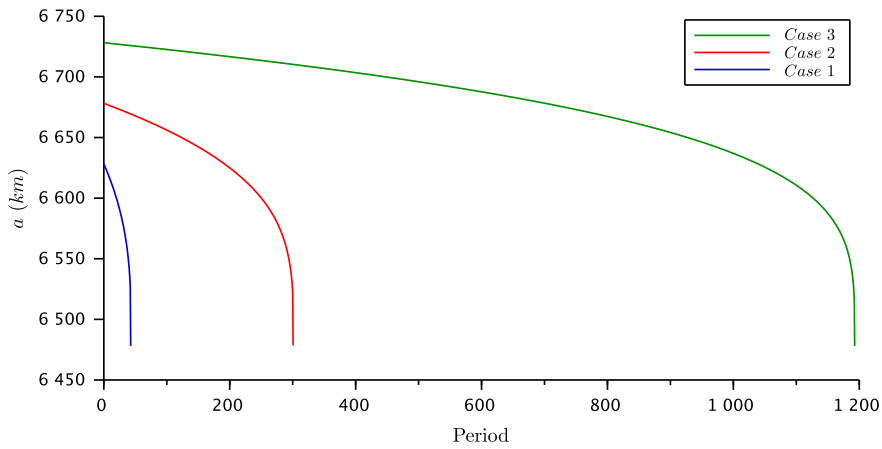


FIGURE 4.22: Semi-major axis change with number of revolutions due to atmospheric drag perturbation for different a .

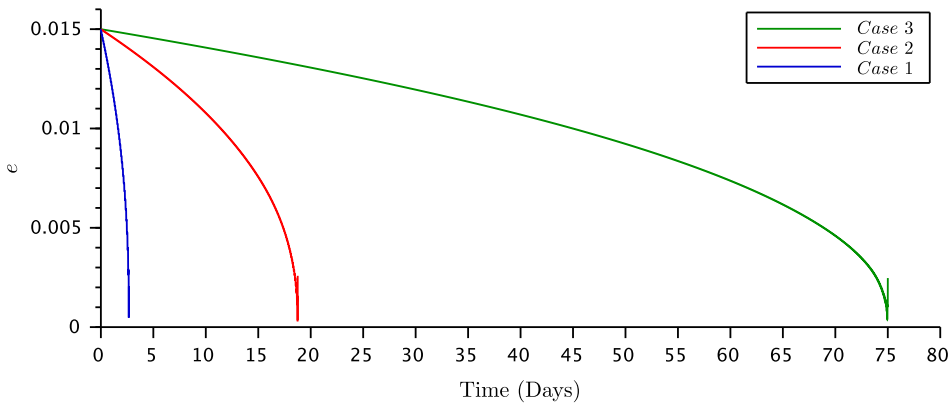


FIGURE 4.23: Variation of the eccentricity of a VLEO due to atmospheric drag perturbation for different a .

Figure 4.23 shows that orbital eccentricity gradually damps in all cases, although the rate varies with initial altitude. The sharp spikes near the end of each curve can be attributed to the chaotic conditions of rapid reentry, during which the orbital parameters become increasingly unstable.

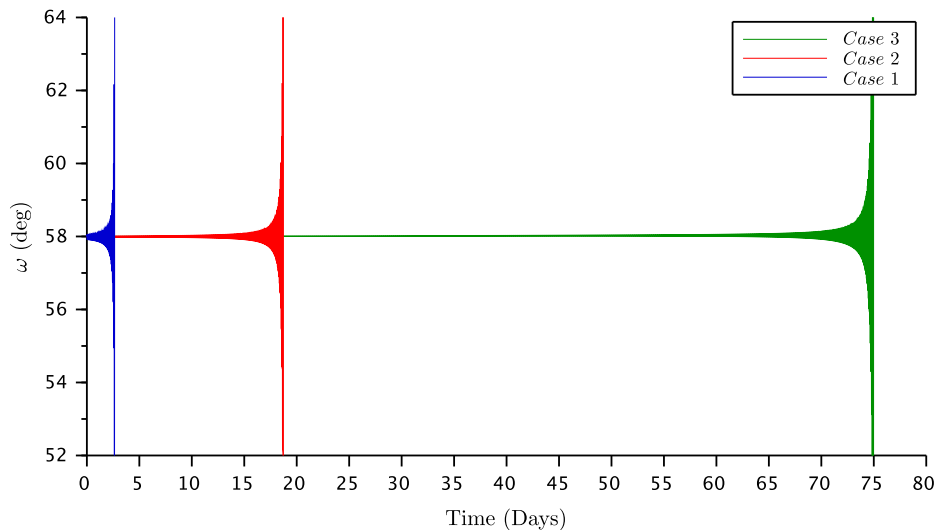


FIGURE 4.24: Variation of the argument of perigee of a VLEO due to atmospheric drag perturbation for different a .

In Figure 4.24, the argument of perigee (ω) remains relatively constant for most of the mission duration across all cases. However, it undergoes abrupt

changes during the final deorbiting phase, as the geometry of the orbit rapidly shifts near atmospheric reentry.

Lastly, Figure 4.25 confirms that the right ascension of the ascending node (RAAN) remains nearly constant throughout the mission, with only minimal variations—consistent with expectations under drag-only perturbation, and as shown in Table 4.10.

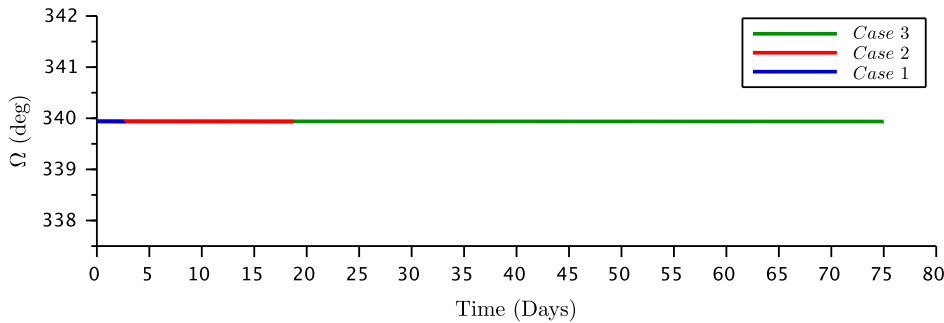


FIGURE 4.25: Variation of the RAAN of a VLEO due to atmospheric drag perturbation for different a .

Simulation With J_2 Perturbation Model

Qty.	Case 1	Case 2	Case 3	Unit
a	6627.34	6677.74	6727.25	km
e	0.0123079	0.0150931	0.0124131	—
i	9.99188	9.98922	9.98959	deg
Ω	219.286	222.446	225.48	deg
ω	296.879	289.345	285.413	deg
ν	179.367	348.209	171.571	deg
T	89.4888	90.5115	91.5201	min
$rev.$	225.57	223.04	220.55	—

TABLE 4.11: Final Orbital Parameters of Satellite Cases with Varying a under J_2 Perturbation.

Isolating the influence of J_2 , a comparative simulation was conducted using identical orbital parameters for three cases that differ only in their semimajor axis (a),

as shown in Table 4.9. The simulations project propagations of two weeks and the final orbital parameters, influenced purely by the oblateness effect, are presented in Table 4.11.

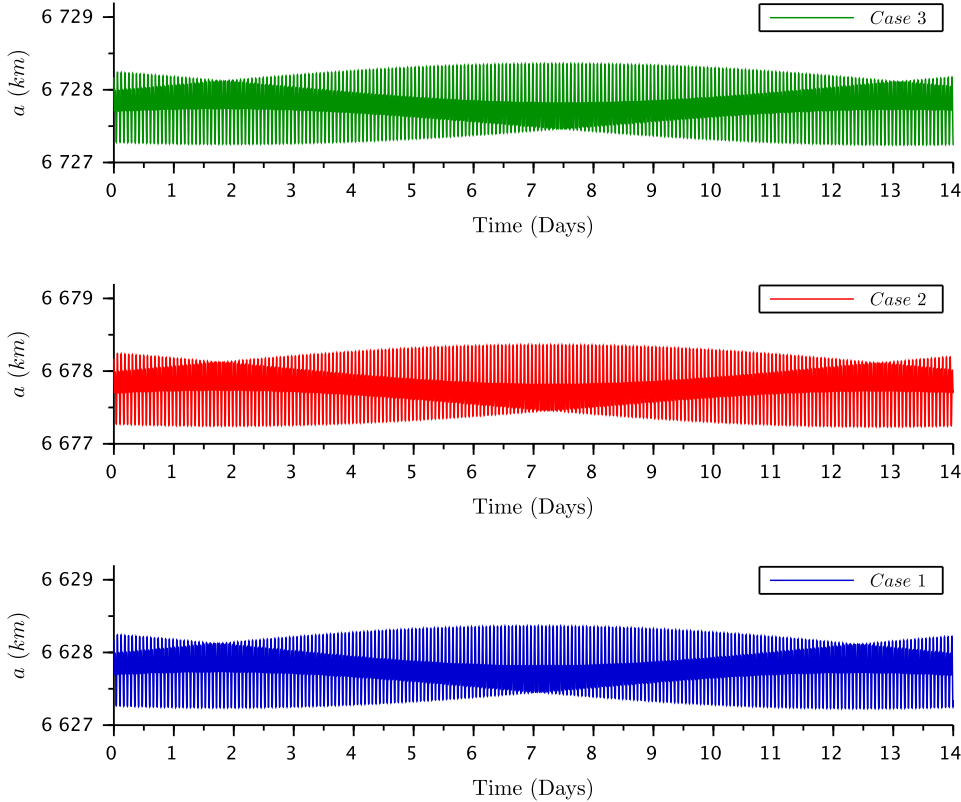


FIGURE 4.26: Variation of the semi-major axis of a VLEO due to J_2 perturbation for different a .

Despite varying altitudes, the resulting variations in orbital elements under J_2 appear minimal, particularly for a , e , and i , whose oscillations remain within narrow bounds. In Figure 4.26, the semimajor axis exhibits nearly identical oscillatory behavior across all three cases, each fluctuating by only a few hundred meters. As with previous simulations isolating the J_2 perturbative effects, the variation of a in each case show a combination of short-periodic, long-periodic, and secular variations. To isolate these variations, a form of data downsizing can be done, essentially strip off the short-periodic contributions so the remaining secular and long-periodic variations can be

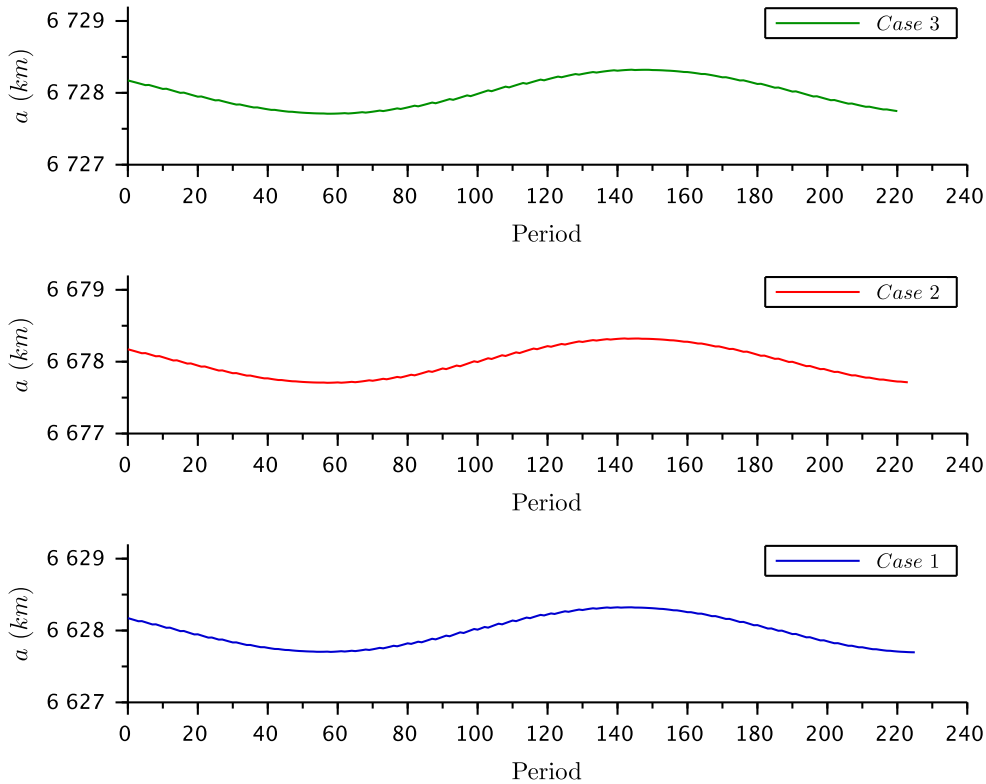


FIGURE 4.27: Semi-major axis change with number of revolutions due to J_2 perturbation for varying a .

The aforementioned method was used in Figure 4.27, these fluctuations reveal only the secular plus long-periodic effects. This pattern is consistent with known zonal harmonics influence, where extracting the a only at each time an orbit is completed, will not highlight the short-periodic effects the satellite undergoes. Long-periodic effects have period considerably longer than one orbital period, as the cycle for all cases will only complete after 170 orbits.

A similar effect is observed for eccentricity in Figure 4.28, and the structure of the beat period is more clearly illustrated in Figure 4.8, where all three orbits share identical oscillation shapes and timing. These results demonstrate that, within the narrow VLEO altitude range explored, the magnitude of J_2 -induced fluctuations is more sensitive to inclination and eccentricity than to modest changes in altitude.

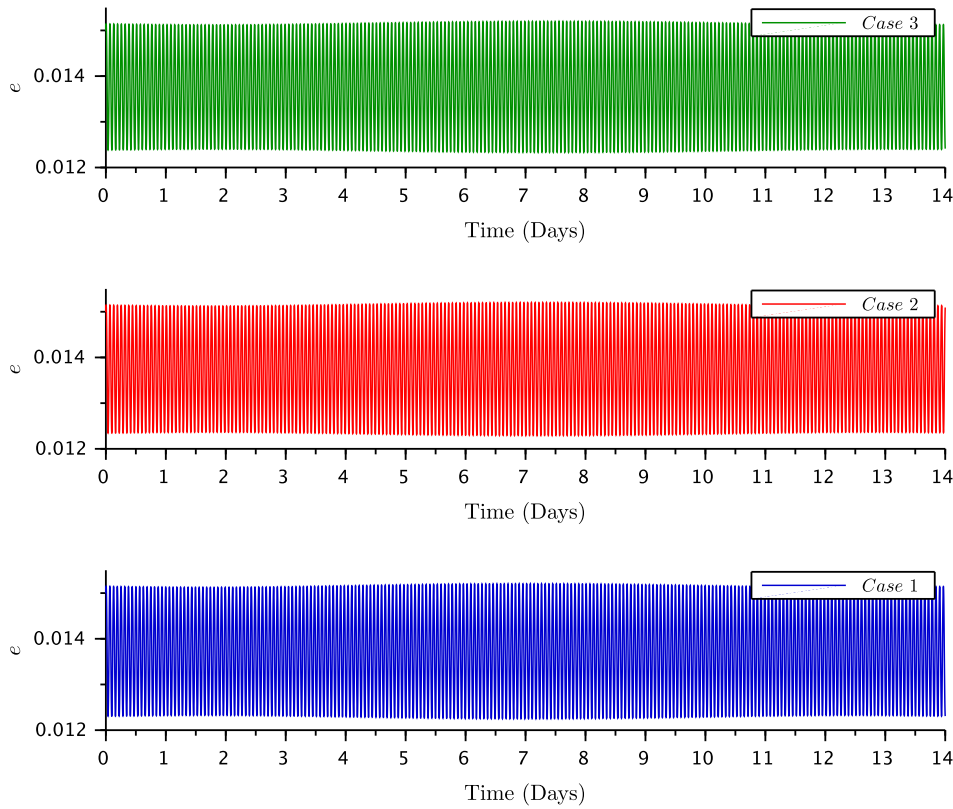


FIGURE 4.28: Variation of the eccentricity of a VLEO due to J_2 perturbation for different a .

However, Figures 4.30 and 4.29 reveal meaningful divergence in angular elements over time. The RAAN (Ω) and argument of perigee (ω) initially progress in a similar manner, but gradually diverge due to the altitude-dependent nature of J_2 perturbation. The case with the lowest semimajor axis ($a = 6628.17$ km) exhibits the fastest nodal regression and perigee rotation, consistent with analytical expressions showing that both $\dot{\Omega}$ and $\dot{\omega}$ are inversely proportional to $(1 - e^2)^2 a^{7/2}$ [16]. Where as altitude (or a) increases, the gravitational gradient, and in perpetuity the perturbing force, becomes weak, reducing the rate of change in these angular elements. This divergence highlights how, even over short durations, variations in semimajor axis begin to produce noticeable long-term effects in angular orbital elements.

(a)	Ω_{final}	$\dot{\Omega}$ [deg/day]	ω_{final}	$\dot{\omega}$ [deg/day]
6628.17	219.286°	-8.6181	296.879°	+17.0627
6678.17	222.446°	-8.3924	289.345°	+16.5246
6728.17	225.48°	-8.1757	285.413°	+16.2437

TABLE 4.12: Calculated Regression and Rotation Rates of Ω and ω over 14 Days under J_2 Perturbation.

(a)	$\dot{\Omega}$ [deg/day]	$\dot{\omega}$ [deg/day]
6628.17	-8.580	+16.769
6678.17	-8.358	+16.334
6728.17	-8.142	+15.913

TABLE 4.13: RAAN regression rate $\dot{\Omega}$ and argument of perigee rotation rate $\dot{\omega}$ under J_2 Perturbation, computed using GP theory.

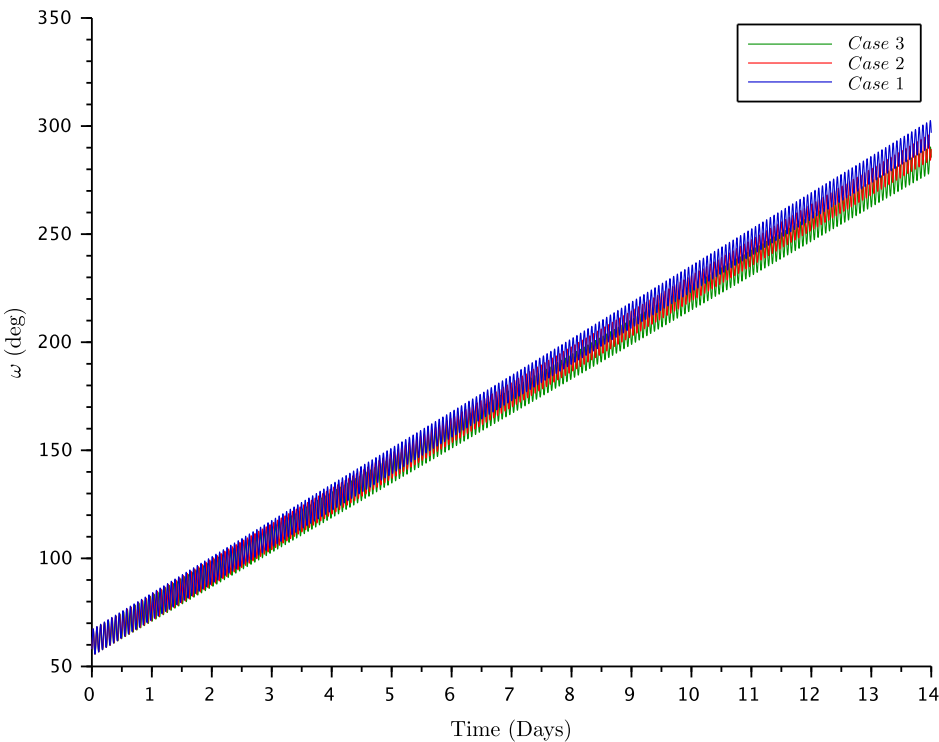


FIGURE 4.29: Variation of the argument of perigee of a VLEO due to J_2 perturbation for different a .

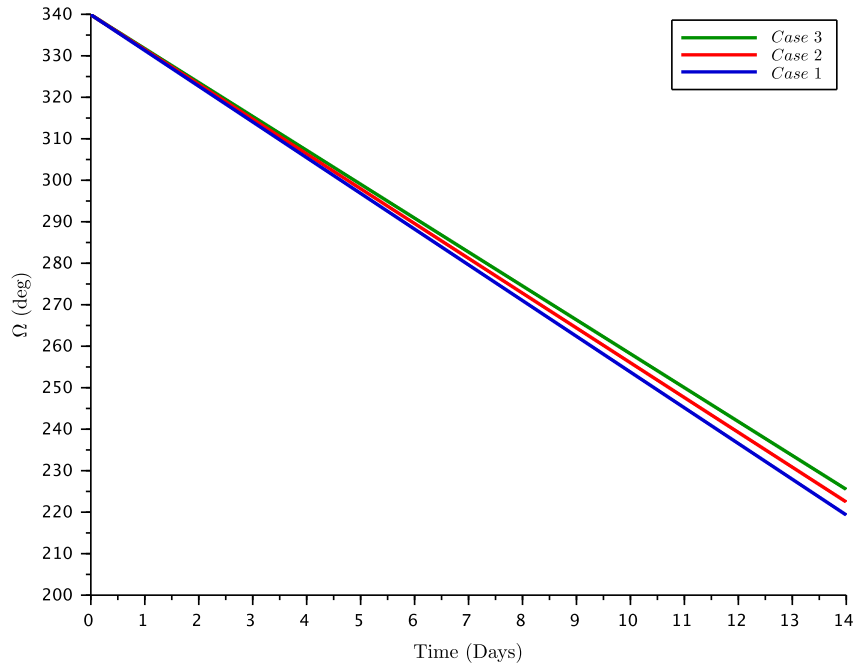


FIGURE 4.30: Variation of the RAAN of a VLEO due to J_2 perturbation for different a .

This relationship is quantitatively confirmed in Table 4.12, which presents rates derived from the simulation by comparing the initial and final values at the end of the 14-day period. These numerical results are in strong agreement with the theoretical predictions calculated via the GP formulation, shown in Table 4.13. While minor differences exist due to numerical integration effects and initial condition rounding, the consistent trend is evident: as altitude increases, the perturbing effects of Earth's oblateness diminish, leading to slower angular drift.

This divergence highlights how even small variations in initial a can produce cumulative and predictable differences in angular parameters, which become significant over longer durations. Overall, the J_2 -only simulations demonstrate that while a , e , and i remain relatively constant in Very Low Earth Orbit (VLEO), angular elements such as Ω and ω are highly sensitive to orbital altitude. These sensitivities have crucial implications for long-term mission planning, constellation phasing, and maintaining coordinated ground coverage.

Simulation With Drag + J_2 Perturbation Model

Qty.	Case 1	Case 2	Case 3	Unit
a	6478.46	6478.53	6477.9	km
e	0.00325291	0.00286327	0.00268559	—
i	9.99856	9.98428	9.99486	deg
Ω	320.552	202.398	153.528	deg
ω	128.782	22.1818	274.581	deg
ν	253.261	247.555	238.175	deg
T	86.4904	86.4918	86.4791	min
$rev.$	35.78	256.76	1032.73	—

TABLE 4.14: Final Orbital Parameters of Satellite Cases with Varying a under Atmospheric Drag + J_2 Perturbation.

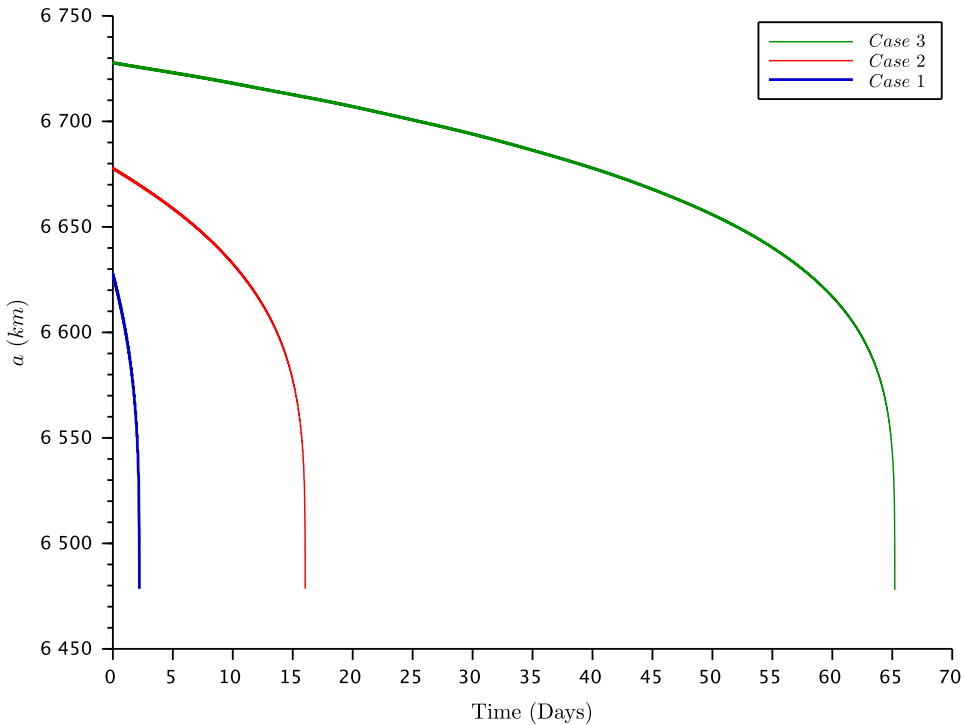


FIGURE 4.31: Variation of the semi-major axis of a VLEO due to atmospheric drag + J_2 perturbation for different a .

The simulation with combined atmospheric drag and J_2 perturbation was carried out for three satellite cases with differing semi-major axes, proceeding until each underwent orbital decay and subsequent reentry. The final orbital parameters upon decay are exhibited in Table 4.14.

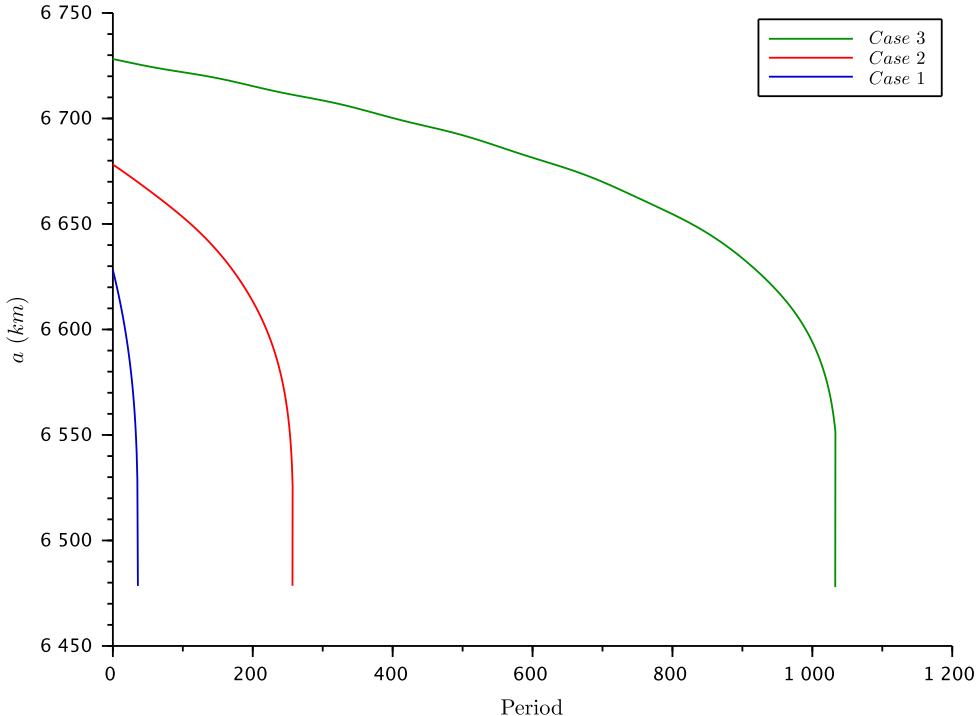


FIGURE 4.32: Semi-major axis change with number of revolutions due to atmospheric drag + J_2 perturbation for varying a .

Compared to the drag-only cases, the inclusion of J_2 causes reductions in orbital lifetime of all satellites. The decay durations observed were:

- Case 1 – from 2.5 to 2.2 days,
- Case 2 – from 18 to 16 days,
- Case 3 – from 75 to 65 days.

These reduced decay spans are in accordance with the endpoints of each case's data, visible across the figures in this section. The clearest visualization of decay can be seen in Figures 4.31 and 4.32, where the semi-major axis decreases progressively until reentry.

It is notable that similar to the drag-only scenario, Cases 2 and 3 exhibit a near-identical decay trajectory once their respective altitudes approach ~ 200 km. This suggests that, regardless of initial conditions, the atmospheric density at lower altitudes dominates and results in a convergence of decay behavior.

A comparison of revolutions completed before decay further illustrates the compounding effects of drag and J_2 perturbation. When compared to the drag-only cases (42.65, 300.68, and 1192.70 revolutions for Cases 1–3, respectively from Table 4.10), the inclusion of J_2 decreases the revolutions completed (35.78, 256.76, and 1032.73). This decrease highlights a slightly accelerated decay process due to J_2 influence on the orbit's geometry and velocity distribution.

Figure 4.32 plots decay against revolution count. Case 3, which sustains orbit the longest, is the only case to exhibit both long-period and secular variations in orbital elements, which consistent with previous simulations. This is especially relevant in the context of J_2 -induced perturbations, which manifest more clearly in longer-lived orbits.

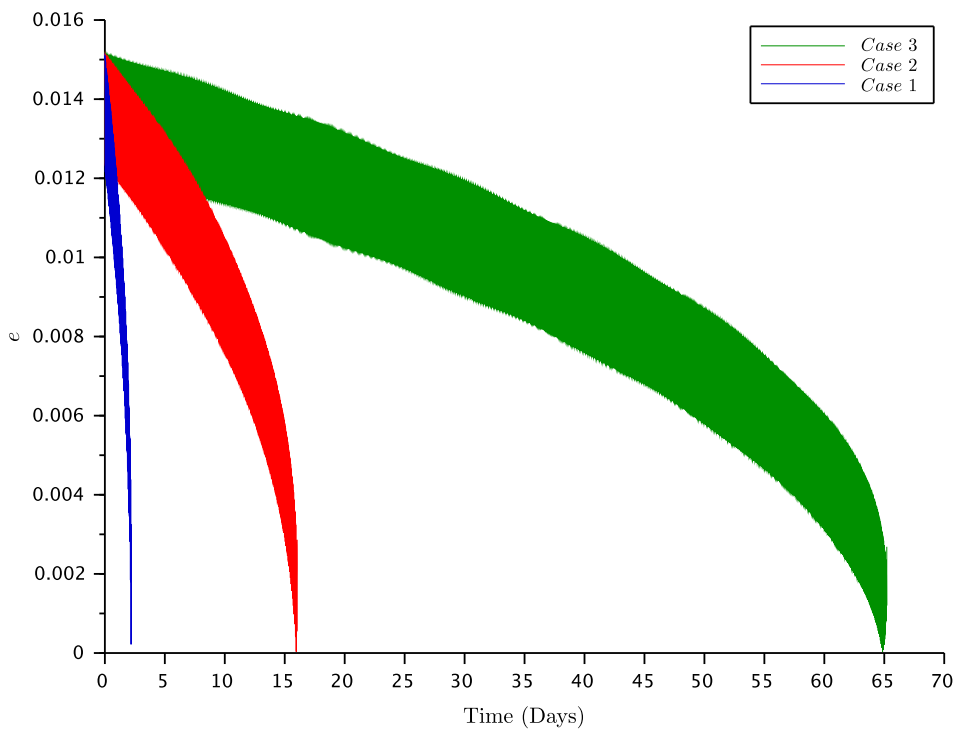


FIGURE 4.33: Variation of the eccentricity of a VLEO due to atmospheric drag + J_2 perturbation for different a .

In terms of eccentricity evolution, Figure 4.33 shows a clear damping trend across all cases due to atmospheric drag. However, the J_2 effect compounds periodic oscillations atop this decay. For Case 3, which remains in orbit the longest, the interplay between short-period, long-period, and secular changes in eccentricity is especially pronounced.

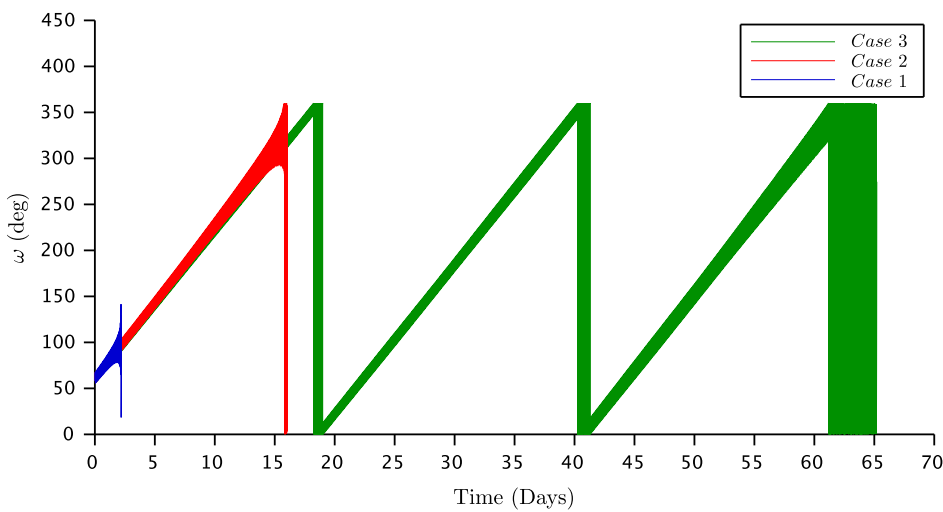


FIGURE 4.34: Variation of the argument of perigee of a VLEO due to atmospheric drag + J_2 perturbation for different a .

The argument of perigee, plotted in Figure 4.34, further demonstrates the compounded influence. As decay progresses and orbital geometry becomes increasingly elliptical and unstable, the perigee begins to rotate with growing amplitude. Among the three, Case 3 undergoes the most pronounced rotation, as its argument of perigee completes nearly three full cycles before reentry.

Finally, the right ascension of the ascending node (RAAN) evolution in Figure 4.35 reveals the effect of J_2 -induced nodal regression. In low Earth orbit, the oblateness of the Earth causes the orbital plane to precess westward. In this simulation, Case 3 again undergoes the most noticeable change in RAAN, crossing its initial value once before decay. The inclusion of the J_2 perturbation does not seem to oppose the GP theoretical rates in Table 4.13, where differing altitudes cause divergence between cases. Most apparent in Cases 2 and 3, where

the RAAN of Case 2 regresses more rapidly due to its slightly higher altitude and inclination.

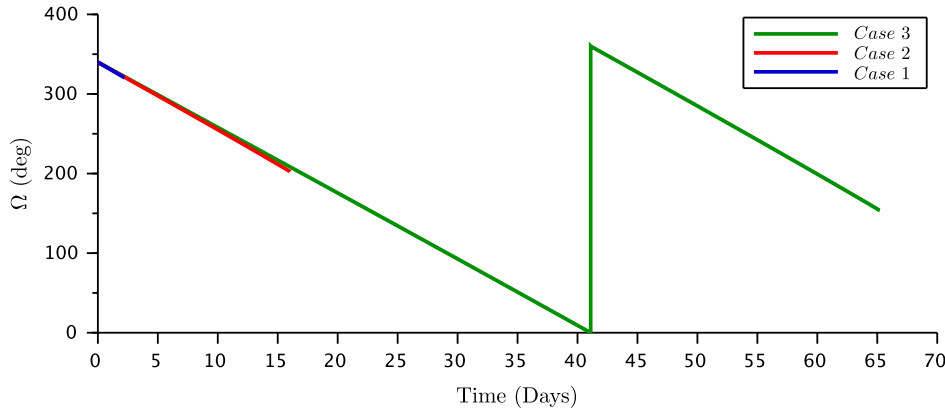


FIGURE 4.35: Variation of the RAAN of a VLEO due to atmospheric drag + J_2 perturbation for different a .

The regression of the RAAN reflects a westward rotation of the orbit's ground track due to the Earth's equatorial bulge (represented by the J_2 term). This shift in orbital plane orientation affects ground coverage and revisit patterns. For longer-lived orbits, like Case 3, this regression becomes evident and can be critical in constellation planning or mission design involving persistent regional coverage.

Relevance of Findings. The results of this study have direct implications for mission planning in Low Earth Orbit (LEO), particularly for Earth Observation (EO) satellites where long-term stability and predictable ground coverage are critical.

From an engineering standpoint, the influence of dominant perturbative forces must be carefully considered during early orbit selection. The findings show that both factors significantly shape the orbital lifetime, geometry evolution, and coverage stability. In particular:

- **Lifetime Optimization:** The combined effect of J_2 and drag accelerates orbital decay, especially below 200 km altitude where atmospheric density rises sharply. Missions targeting low altitudes for improved resolution must factor in shorter lifespans and plan for frequent replenishing or accept

shorter mission durations. Case 3's longevity highlights the value of initially higher orbits (>500 km) in delaying reentry and preserving nominal orbital elements.

- **Orbital Stability and Coverage:** The simulation confirms that higher orbits (e.g., Case 3) better preserve orbital geometry and allow J_2 -induced perturbations like RAAN regression and perigee rotation to actuate in predictable, periodic patterns. These behaviors can be exploited in sun-synchronous or frozen orbit designs to ensure consistent lighting and revisit patterns that can be key for EO tasks.
- **Engineering Application Cost vs. Performance Tradeoffs:** With launch costs tightly coupled to orbital altitude, mission planners face a tradeoff between fuel efficiency and operational longevity. Lower inclinations and moderate altitudes (ex. 400–500 km) offer a compromise between minimized launch delta-V and prolonged service life. This study recommends such orbits for small EO missions where cost-efficiency and moderate revisit performance are prioritized.
- **Constellation Planning:** For missions requiring coordinated coverage (e.g., imaging constellations), J_2 -induced RAAN regression must be factored into plane phasing strategies. As demonstrated, differing altitudes lead to diverging regression rates, which can be used to passively maintain spacing between orbital planes, thereby minimizing station-keeping fuel needs.

In summary, the compounded effects of drag and J_2 not only influence satellite decay rates but also shape orbital element evolution in ways that are exploitable in engineering design. Mission designers should leverage these predictable dynamics to select cost-efficient, long-lasting, and stable orbits suited to their EO objectives.

CHAPTER 5

SUMMARY, CONCLUSION, RECOMMENDATION

5.1 Summary of Research

Founded on what have been exhibited and discussed in this thesis, the research can be summed up as the following:

1. Mathematical models for conversion between classical orbital elements and state vectors have been successfully constructed. The tools have demonstrated its function to provide both a consistent initial condition and post-propagation data for analysis
2. The RK4 integration model has back-boned the orbital propagation framework which is the bulk of this research. Its custom-built nature has also provided the work considerable control over the solver behaviour, which was vital for quick debugging and expedient adaptation of the simulations.
3. Perturbation models of both collective and individual dominant perturbative forces exhibited successful application in numerical simulations using the custom built RK4 integrator.
4. Results stemming from the simulations has successfully projected how the propagated orbital elements and state vectors behaves over a period of time under the effect of dominant perturbative forces.

5.2 Research Conclusions

The conclusions based on the results of this research are as follows:

5.2.1 The Success of the Simulation

This can only be measured in relation to how effectively they reproduce and predict real-world orbital behaviors under various perturbation models. Consequently, the results not only fulfill theoretical expectations but also provide a foundation for future predictive analysis in very low Earth orbit (VLEO) mission design.

Two-Body Restricted Simulations

- The numerical integrator's effectiveness was verified with near-constant states over a 24-hour period, modelling orbital motion considered ideal. Minor deviations fall within acceptable bounds, and are likely the result of numerical artifacts. The lengthy 30-second timestep, leaves room for further accuracy that could be achieved with smaller timesteps, with greater computational resources.

J_2 Perturbed Simulations

- Through simulating the isolated J_2 perturbative effect, it showed that key orbital elements such as semi-major axis, eccentricity, and inclination remain effectively constant, while the angular elements, the right ascension of the ascending node (Ω) and argument of perigee (ω), exhibit characteristic J_2 -induced drift. The results align with theoretical expectations of effects due to Earth oblateness, including the notable turning point in $\dot{\omega}$ at the critical inclination of 63.43° , where perigee remains stationary.

- The simulations predicted that higher inclinations reduced the regression rate of Ω , while the behaviors of ω alluded to the influence of a critical inclination predicted by GP theory. There were minimal variations in angular drift with varying altitudes, though the rates still abide by the increased sensitivity to J_2 at lower altitudes.
- There was groundwork laid out for more detailed prediction, though limitations remain. The preclusion of higher-order zonal harmonics beyond J_2 may lead to small but accumulative inaccuracies, particularly for missions requiring long-term precision.

Drag Perturbed Simulations

- The drag-only simulations succeed in capturing the overall behavior of orbital decay under atmospheric drag, with results that reflect physically realistic trends across varying a . As expected, lower initial altitudes correspond to more rapid decay, with orbital lifetimes ranging from just a few days to several weeks. The simulations also reproduce the typical damping of eccentricity over time, and confirm that angular elements such as the argument of perigee and RAAN remain largely stable until the terminal descent phase, during which rapid geometric changes occur due to increased atmospheric interaction.
- USSA76 does not consider temporal or spatial variability in atmospheric density due to solar flux, geomagnetic disturbances, or latitude-dependent effects. Considering these elements would rid any possible deviations from real-world behavior. Further improvements to the model could incorporate adaptive time-stepping, updated atmospheric density models (e.g., NRLMSISE-00), and variable drag coefficients to enhance prediction accuracy.

Drag + J_2 Perturbed Simulations

- This segment of simulations demonstrated the compounding effects of atmospheric drag and Earth's oblateness. Drag interactions steadily decreased the semi-major axis, leading to orbital decay. Inclination and initial altitude were shown to influence decay duration, orbital geometry, and the number of completed revolutions, while eccentricity consistently damped across the board. Compounding with the effect of J_2 predicted additional secular and periodic variations, noticeable in longer-lived orbits, steadily shifting time to decay, orbital precession rates, and evolution of angular element. These results align with theoretical expectations and highlight the sensitivity of angular parameters, especially ω and Ω , to the compounded effects of drag and zonal harmonics.
- The results are bounded to the same limits that arise during simulations with isolating each dominant perturbative force. As the combined model also incorporates simplifications in the consideration both isolated perturbative, further accuracy can be achieved with adaptive time-stepping, updated density models, and extended geopotential expansions. Though the groundwork is established for further detailed modelling of predicting dominant perturbative effect

However accurate these simulations are at predicting satellite behavior, the use of a fixed timestep of 30 seconds, while computationally efficient, may lead to numerical smoothing and overlook precise dynamics. And such consequence would only exacerbate during the orbits under dominant perturbative effects, where conditions change rapidly.

5.2.2 Importance of Findings

The significance of this study will stand on its function to aid in real-world low Earth orbital mission design, where success is critical on precise lifetime

prediction, fuel efficiency, and orbital stability. This section outlines how the findings translate into concrete engineering considerations.

Orbital Lifetime and Altitude Planning

- Satellites operating below ~ 200 km are rapidly deorbited due to steep increases in atmospheric density, whereas those starting at the threshold of VLEO, 400-450km, exhibit substantially extended mission durations. While also dependent on satellite mass and form, the research ultimately finds that missions that require longer operational windows should target altitudes above 299 km, accepting the associated increase in launch energy.
- Conversely, the dependency of higher altitude will compromise resolution and signal latency for EO missions. The decay rates and the methods to predict them will to assess tradeoffs, giving mission designer the agency to balance operational life with imaging performance.

Inclination and Perturbation Sensitivity

- Along with drag, J_2 -induced precession remained active even in decay behavior. Across all inclinations, RAAN regression and perigee rotation persist, though with rates varying predictably with inclination and altitude. Findings of the method corroborate that the selection of inclination is vital for missions prioritizing stable, repeatable ground tracks or coordinated satellite constellations.
- Such as a sun-synchronous orbit (SSO), that would require precise coordination of inclination and altitude to achieve an acceptable nodal regression rate. The research provides the groundwork that such a precision is feasible even in drag-affected regimes, particularly in the upper band of VLEO, 250-450 km, where the evolving orbital geometry can be predicted and utilized.

Coverage vs. Lifetime Trade-offs

- Full Earth coverage can be exploited via polar orbits, though it can be compromised by accelerated decay due to higher drag exposure over high-latitude atmospheric bulges. Near-critical inclination orbits (ex, 50–70° & 140–160°) provide a middle ground that enables broad regional coverage, reduced decay rates, and fewer maneuvering requirements.
- Satellite that lack means to maneuver, benefit from this. Inclinations with more favorable perturbative profiles can extend mission lifetime while still capturing target regions, all with minimal hardware costs.

Eccentricity Damping and Imaging Stability

- Uniform eccentricity is indicative of orbit shape, where in constellations provides consistency in revisit patterns, timing, and coverage swaths. The intensity of eccentricity damping is dependent on how elliptic an orbit is, as near-circular orbit leaves little space for circularization. Aside from maintaining a near-constant altitude, a circularity would leave the dampening effect to be predictable and manageable to an extent.

Increased Revisit Opportunities from Shorter Periods

- The results observe a shortening of orbital period due to decay, concluding in a higher number of revolutions within a given timeframe. This behavior can be advantageous for EO missions that prioritize rapid revisit times over its lifespan, such as disaster monitoring or crop surveillance. Provided an the compromise of reduce operational durations is acceptable, missions would have increased sampling frequency in time-critical applications.

Constellation Phasing and Passive Control

- The simulation-derived rate of changes due to J_2 can be leveraged for phasing strategies in satellite orbits. For example, launching satellites into slightly differing altitudes can naturally drift apart or towards each other in RAAN over time, aiding in station-keeping strategies. This can be paramount for resource-constrained missions that aim to deploy large numbers of low-cost spacecraft. The findings can serve as a foundation for modeling drift rates, enabling engineers to create self-organizing constellations with minimal intervention.

The study reveals that understanding and predicting the dominant perturbative effects is crucial for performance, cost-effectiveness, and reliability in small satellite missions. The simulations do have limitations like simplified perturbation modeling and coarse time resolution, yet they validate the groundwork of open-source tools like Scilab for space mission analysis. With improvements like higher-resolution integration and enhanced atmospheric models, these methods could become a valuable asset for the broader aerospace community, ensuring better decision-making in altitude selection, inclination trade-offs, and orbital maintenance.

5.3 Recomendations for Future Research

Based on the results, there are possibilities for further efforts that can be developed from this research:

- **Integration of More Realistic Atmospheric Models:** Using more modern and dynamic models such as NRLMSISE-00 or JB2008 could improve drag prediction accuracy, especially for missions in Very Low Earth Orbit (VLEO) where atmospheric variability plays a larger role.
- **Detailed Satellite Modeling:** Specifics of spacecraft geometry, material properties, and orientation behavior would enable more accurate determination of the drag coefficient, and potentially lift, to reflect real-world aerodynamic interactions.
- **Higher-Order Gravity Perturbations:** Additional geopotential terms such as J_3 , J_4 , or even tesseral harmonics would provide more complete insight into long-term orbital behavior, especially for non-equatorial orbits.
- **Improved Temporal Resolution:** Utilizing smaller timesteps with greater computational resources could capture short-term perturbation effects more precisely and reduce numerical integration drift.
- **Expansion of Perturbation Types:** Future works would include third-body effects (e.g., Moon and Sun), solar radiation pressure, and eclipsing conditions for more complete mission environment modeling.
- **Open-Source Tool Development:** Continued work and validation of self-written, open-source Scilab tools not only enables transparency and accessibility but also contributes to the open scientific community by providing cost-effective alternatives to proprietary software.

Bibliography

- [1] O. Jonathan. “Sky skimmers: The race to fly satellites in the lowest orbits yet,” BBC News. (Feb. 9, 2025), [Online]. Available: <https://www.bbc.com/future/article/20250207-sky-skimmers-the-race-to-send-satellites-into-very-low-earth-orbits> (visited on 03/03/2025).
- [2] J. Virgili-Llop, P. Roberts, D. Z. Hao, L. Ramio-Tomas, and V. Beauplet, “Very low earth orbit mission concepts for earth observation. benefits and challenges,” Nov. 2014.
- [3] D. Anna, *Kármán line*, in *Encyclopedia Britannica*, Sep. 6, 2024. [Online]. Available: <https://www.britannica.com/science/Karman-line>.
- [4] W. Muszyński-Sulima, “Cold war in space: Reconnaissance satellites and US-soviet security competition,” *European journal of American studies*, vol. 18, no. 2, Jun. 30, 2023, ISSN: 1991-9336. DOI: [10.4000/ejas.20427](https://doi.org/10.4000/ejas.20427). [Online]. Available: <http://journals.openedition.org/ejas/20427> (visited on 07/08/2025).
- [5] H. Luo, X. Shi, Y. Chen, *et al.*, “Very-low-earth-orbit satellite networks for 6g,” *Communications of HUAWEI RESEARCH*, no. 2, Sep. 2022. [Online]. Available: <https://www-file.huawei.com/-/media/corp2020/pdf/publications/huawei-research/2022/huawei-research-issue2-en.pdf>.
- [6] Z. Lei, *Casic plans new satellite network by 2030*, <https://global.chinadaily.com.cn/a/202307/13/WS64af9523a31035260b8163bb.html>, China Daily. Accessed: 2025-05-22, 2023.
- [7] C. McGrath, C. Lowe, M. Macdonald, and S. Hancock, “Investigation of very low earth orbits (VLEOs) for global spaceborne lidar,” *CEAS Space Journal*, vol. 14, no. 4, pp. 625–636, Oct. 2022, Publisher: Springer Science and Business Media LLC, ISSN: 1868-2502, 1868-2510. DOI: [10.1007/s10552-022-00950-1](https://doi.org/10.1007/s10552-022-00950-1).

1007/s12567-022-00427-2. [Online]. Available: <https://link.springer.com/10.1007/s12567-022-00427-2>.

- [8] A. Sánchez-Juárez, *A new space economy: The emerging business in low orbit satellites*, <https://www.uoc.edu/en/news/2022/237-economy-new-space>, 2022.
- [9] P. Bhalla, “Very low earth orbit (vleo): The emerging band of interest in space,” *Synergy: Journal of the Centre for Joint Warfare Studies (CEN-JOWS)*, vol. 3, no. 1, pp. 114–131, Feb. 2024, ISSN: 2583-536X. [Online]. Available: https://cenjows.in/wp-content/uploads/2024/05/SYNERGY_Journal_Online_CENJOWS_Feb_2024_Edition.pdf.
- [10] N. H. Crisp, P. C. E. Roberts, S. Livadiotti, *et al.*, “The benefits of very low earth orbit for earth observation missions,” *Progress in Aerospace Sciences*, vol. 117, p. 100619, Aug. 2020, ISSN: 03760421. DOI: [10.1016/j.paerosci.2020.100619](https://doi.org/10.1016/j.paerosci.2020.100619). arXiv: [2007.07699 \[physics\]](https://arxiv.org/abs/2007.07699). [Online]. Available: [http://arxiv.org/abs/2007.07699](https://arxiv.org/abs/2007.07699) (visited on 07/08/2025).
- [11] L. McCreary, “A satellite mission concept for high drag environments,” *Aerospace Science and Technology*, vol. 92, pp. 972–989, Sep. 2019, Publisher: Elsevier BV, ISSN: 1270-9638. DOI: [10.1016/j.ast.2019.06.033](https://doi.org/10.1016/j.ast.2019.06.033). [Online]. Available: <https://linkinghub.elsevier.com/retrieve/pii/S1270963819311150>.
- [12] Y. C. Chan and *et al.*, “How low can you go: Advocating very low earth orbit as the next frontier for satellite operations,” in *Proceedings of the 8th European Conference on Space Debris (Virtual)*, 20–23 April 2021, ESA Space Debris Office, Darmstadt, Germany, Apr. 2021. [Online]. Available: <https://conference.sdo.esoc.esa.int/proceedings/sdc8/paper/109>.
- [13] COESA, *U.S. Standard Atmosphere, 1976*. NOAA, Oct. 1, 1976, 227 pp. [Online]. Available: <https://ntrs.nasa.gov/citations/19770009539>.
- [14] H. D. Curtis, *Orbital mechanics for engineering students* (Elsevier aerospace engineering series), Fourth edition. Kidlington, Oxford, United Kingdom:

Butterworth-Heinemann, an imprint of Elsevier, 2020, 1 p., ISBN: 978-0-08-102133-0.

- [15] D. A. Vallado, *Fundamentals of Astrodynamics and Applications*, Fourth Edition. Microcosm Press, 2013, ISBN: 978-1-881883-20-3.
- [16] J. R. Wertz and W. J. Larson, Eds., *Space Mission Analysis and Design* (Space Technology Library), Third Edition. El Segundo, Calif. : Dordrecht ; Boston: Microcosm Press; Kluwer Academic Publisher, 1999, 969 pp., ISBN: 978-0-7923-5901-2 978-1-881883-10-4.

Appendices

Appendix A: Mathematical Models

```
1 function [r, v] = sv_from_coe(coe, mu)
2 // This function computes the state vector (r,v) from the
3 // classical orbital elements (coe).
4
5 h     = coe(1);
6 e     = coe(2);
7 RA    = coe(3);
8 incl  = coe(4);
9 w     = coe(5);
10 TA   = coe(6);
11
12 // Equations 4.45 and 4.46 (rp and vp are column vectors):
13 rp = (h^2 / mu) * (1 / (1 + e * cos(TA))) * (cos(TA) * [1; 0; 0]
14     + sin(TA) * [0; 1; 0]);
15 vp = (mu / h) * (-sin(TA) * [1; 0; 0] + (e + cos(TA)) * [0; 1;
16     0]);
17
18 // Equation 4.34: Rotation matrix R3_W
19 R3_W = [cos(RA), sin(RA), 0;
20         -sin(RA), cos(RA), 0;
21         0, 0, 1];
22
23 // Equation 4.32: Rotation matrix R1_i
24 R1_i = [1, 0, 0;
25         0, cos(incl), sin(incl);
26         0, -sin(incl), cos(incl)];
27
28 // Equation 4.34: Rotation matrix R3_w
29 R3_w = [cos(w), sin(w), 0;
30         -sin(w), cos(w), 0;
31         0, 0, 1];
32
33 // Equation 4.49: Combined rotation matrix Q_pX
```

COMPARATIVE NUMERICAL STUDY OF DOMINANT PERTURBATION EFFECTS ON VLEO
SATELLITE ORBIT DEGRADATION

```

32 Q_pX = (R3_w * R1_i * R3_w)';
33
34 // Equations 4.51 (r and v are column vectors):
35 r = Q_pX * rp;
36 v = Q_pX * vp;
37
38 // Convert r and v into row vectors:
39 r = r';
40 v = v';
41 end

```

LISTING 1: Function to extract state vector from classical orbital elements

```

1 function coe = coe_from_sv(R, V, mu)
2 // This function computes the classical orbital elements (coe)
3 // from the state vector (R,V) using Algorithm 4.1.
4
5 eps = 1.e-6; // Small number for eccentricity threshold
6
7 r = norm(R);
8 v = norm(V);
9 vr = sum(R .* V) / r; // Dot product using element-wise
10 // multiplication
11 H = cross(R, V);
12 h = norm(H);
13
14 // Equation 4.7: Inclination
15 incl = acos(H(3) / h);
16
17 // Equation 4.8: Node vector
18 N = cross([0 0 1], H);
19 n = norm(N);
20
21 // Equation 4.9: Right Ascension of Ascending Node (RA)
22 if incl ~= 0
23 RA = acos(N(1) / n);
24 if N(2) < 0
25 RA = 2 * %pi - RA;
26 end
27 else

```

COMPARATIVE NUMERICAL STUDY OF DOMINANT PERTURBATION EFFECTS ON VLEO
SATELLITE ORBIT DEGRADATION

```
27 RA = 0;
28 end
29
30 // Equation 4.10: Eccentricity vector
31 E = 1 / mu * ((v^2 - mu / r) * R - r * vr * v);
32 e = norm(E);
33
34 // Equation 4.12: Argument of perigee (w)
35 if incl ~= 0
36 if e > eps
37 w = acos(sum(N .* E) / n / e); // Dot product using element-wise
      multiplication
38 if E(3) < 0
39 w = 2 * %pi - w;
40 end
41 else
42 w = 0;
43 end
44 else
45 if e > eps
46 w = acos(E(1) / e);
47 if E(2) < 0
48 w = 2 * %pi - w;
49 end
50 else
51 w = 0;
52 end
53 end
54
55 // Equation 4.13a: True anomaly (TA)
56 if incl ~= 0
57 if e > eps
58 TA = acos(sum(E .* R) / e / r); // Dot product using element-
      wise multiplication
59 if vr < 0
60 TA = 2 * %pi - TA;
61 end
62 else
63 TA = acos(sum(N .* R) / n / r); // Dot product using element-
      wise multiplication
```

COMPARATIVE NUMERICAL STUDY OF DOMINANT PERTURBATION EFFECTS ON VLEO
SATELLITE ORBIT DEGRADATION

```

64  if R(3) < 0
65  TA = 2 * %pi - TA;
66  end
67  end
68  else
69  if e > eps
70  TA = acos(sum(E .* R) / e / r); // Dot product using element-
71  // wise multiplication
72  if vr < 0
73  TA = 2 * %pi - TA;
74  end
75  else
76  TA = acos(R(1) / r);
77  if R(2) < 0
78  TA = 2 * %pi - TA;
79  end
80  end
81
82 // Equation 4.62: Semimajor axis (a)
83 a = h^2 / mu / (1 - e^2);
84
85 coe = [h, e, RA, incl, w, TA, a];
86 end

```

LISTING 2: Function to extract classical orbital elements from state
vector

```

1 function density = atmosphere(z)
2 // Geometric altitudes (km):
3 h = [ 0 25 30 40 50 60 70 80 90 100 110 120 130 140
4 150 180 200 250 300 350 400 450 500 600 700 800 900 1000];
5
6 // Corresponding densities (kg/m^3) from USSA76:
7 r = [1.225, 4.008e-2, 1.841e-2, 3.996e-3, 1.027e-3, 3.097e-4,
8 8.283e-5, ...
9 1.846e-5, 3.416e-6, 5.606e-7, 9.708e-8, 2.222e-8, 8.152e-9,
10 3.831e-9, ...
11 2.076e-9, 5.194e-10, 2.541e-10, 6.073e-11, 1.916e-11, 7.014e-12,
12 2.803e-12, ...

```

COMPARATIVE NUMERICAL STUDY OF DOMINANT PERTURBATION EFFECTS ON VLEO
SATELLITE ORBIT DEGRADATION

```

9  1.184e-12, 5.215e-13, 1.137e-13, 3.070e-14, 1.136e-14, 5.759e
10 -15, 3.561e-15];

11 // Scale heights (km):
12 H = [7.310, 6.427, 6.546, 7.360, 8.342, 7.583, 6.661, 5.927,
13 5.533, 5.703, 6.782, ...
14 9.973, 13.243, 16.322, 21.652, 27.974, 34.934, 43.342, 49.755,
15 54.513, 58.019, ...
16 60.980, 65.654, 76.377, 100.587, 147.203, 208.020];

17 // Handle altitudes outside of the range:
18 if z > 1000 then
19   z = 1000;
20 elseif z < 0 then
21   z = 0;
22 end

23 // Determine the interpolation interval:
24 ind = find(h >= z);
25 i = ind(1) - 1;
26 if i < 1 then
27   i = 1;
28 end

29 // Exponential interpolation:
30 density = r(i) * exp(-(z - h(i)) / H(i));
31
32 endfunction

```

LISTING 3: Function to compute density from altitude

```

1 function dYdt = two_body_ode(t, Y, params)
2   mu = params.mu; // 398600 km^3/s^2
3   x = Y(1);
4   y = Y(2);
5   z = Y(3);
6   vx = Y(4);
7   vy = Y(5);
8   vz = Y(6);
9
10  r = sqrt(x^2 + y^2 + z^2);
11

```

```

12 dYdt = [
13 vx;
14 vy;
15 vz;
16 -mu*x/r^3;
17 -mu*y/r^3;
18 -mu*z/r^3
19 ];
20 endfunction

```

LISTING 4: Two-body restricted ODE function

```

1 function [tout, yout] = rk4_integrator(ode_function, tspan, y0, h)
2     t0 = tspan(1);
3     tf = tspan(2);
4
5     t = t0;
6     y = y0;
7     tout = t;
8     yout = y';
9
10    while t < tf
11        if (t+h > tf) then
12            h = tf - t; // adjust last step
13        end
14
15        k1 = ode_function(t, y);
16        k2 = ode_function(t + h/2, y + h/2*k1);
17        k3 = ode_function(t + h/2, y + h/2*k2);
18        k4 = ode_function(t + h, y + h*k3);
19
20        y = y + (h/6)*(k1 + 2*k2 + 2*k3 + k4);
21        t = t + h;
22
23        tout = [tout; t];
24        yout = [yout; y'];
25    end
26 endfunction

```

LISTING 5: Function for RK4 integrator

COMPARATIVE NUMERICAL STUDY OF DOMINANT PERTURBATION EFFECTS ON VLEO
SATELLITE ORBIT DEGRADATION

```
1 function dydt = dragj2(t, f, params)
2 mu = params.mu;
3 RE = params.RE;
4 J2 = params.J2;
5 CD = params.CD;
6 A = params.A;
7 m = params.m;
8 wE = params.wE;
9
10 r = f(1:3); // position [km]
11 v = f(4:6); // velocity [km/s]
12 R = norm(r); // magnitude position [km]
13 V = norm(v); // magnitude velocity [km/s]
14
15 //... Compute the J2 perturbing acceleration from Equation 12.30:
16 xx = r(1); yy = r(2); zz = r(3);
17
18 fac = 3/2 * J2 * (mu/R^2) * (RE/R)^2;
19 ap = -fac * [(1 - 5*(zz/R)^2)*(xx/R)
20 (1 - 5*(zz/R)^2)*(yy/R)
21 (3 - 5*(zz/R)^2)*(zz/R)];
22
23 // Altitude and atmospheric density
24 alt = R - RE; // km
25 rho = atmosphere(alt); // kg/m^3
26
27 // Sanity check on density
28 if size(rho, "*") <> 1 then
29 error("atmosphere() returned invalid density value.");
30 end
31
32 // Relative velocity
33 Vrel = v - cross(wE, r); // km/s
34 vrel = norm(Vrel); // km/s
35
36 // Protect against division by zero
37 if vrel == 0 then
38 uv = [0; 0; 0];
39 else
40 uv = Vrel / vrel; // unit vector
```

COMPARATIVE NUMERICAL STUDY OF DOMINANT PERTURBATION EFFECTS ON VLEO
SATELLITE ORBIT DEGRADATION

```

41 end
42
43 // Drag acceleration (km/s^2)
44 at = -CD * A / m * rho * (1000 * vrel)^2 / 2 * uv / 1000;
45
46 // Gravitational acceleration (km/s^2)
47 a0 = -mu * r / R^3;
48
49 // Total acceleration of drag + J2
50 a = a0 + at + ap
51
52 // Return derivative of state vector (6x1 column vector)
53 dydt = [v; a];
54 endfunction

```

LISTING 6: Function for RK4 integrator

```

1  function dydt = dragj2(t, f, params)
2  mu = params.mu;
3  RE = params.RE;
4  J2 = params.J2;
5  CD = params.CD;
6  A = params.A;
7  m = params.m;
8  wE = params.wE;
9
10 r = f(1:3); // position [km]
11 v = f(4:6); // velocity [km/s]
12 R = norm(r); // magnitude position [km]
13 V = norm(v); // magnitude velocity [km/s]
14
15 //...Compute the J2 perturbing acceleration from Equation 12.30:
16 xx = r(1); yy = r(2); zz = r(3);
17
18 fac = 3/2 * J2 * (mu/R^2) * (RE/R)^2;
19 ap = -fac * [(1 - 5*(zz/R)^2)*(xx/R)
20 (1 - 5*(zz/R)^2)*(yy/R)
21 (3 - 5*(zz/R)^2)*(zz/R)];
22
23 // Altitude and atmospheric density
24 alt = R - RE; // km

```

COMPARATIVE NUMERICAL STUDY OF DOMINANT PERTURBATION EFFECTS ON VLEO
SATELLITE ORBIT DEGRADATION

```

25 rho = atmosphere(alt);           // kg/m^3
26
27 // Sanity check on density
28 if size(rho, "*") <> 1 then
29   error("atmosphere() returned invalid density value.");
30 end
31
32 // Relative velocity
33 Vrel = v - cross(wE, r);        // km/s
34 vrel = norm(Vrel);              // km/s
35
36 // Protect against division by zero
37 if vrel == 0 then
38   uv = [0; 0; 0];
39 else
40   uv = Vrel / vrel;            // unit vector
41 end
42
43 // Drag acceleration (km/s^2)
44 at = -CD * A / m * rho * (1000 * vrel)^2 / 2 * uv / 1000;
45
46 // Gravitational acceleration (km/s^2)
47 a0 = -mu * r / R^3;
48
49 // Total acceleration of drag + J2
50 a = a0 + at + ap
51
52 // Return derivative of state vector (6x1 column vector)
53 dydt = [v; a];
54 endfunction

```

LISTING 7: Function for drag + J_2 acceleration

```

1 mu = 398600;                      // km^3/s^2
2 funcprot(0);
3 hours = 3600;
4 days = 24 * hours;
5 deg = %pi / 180;
6 params.mu = 398600;
7 params.RE = 6378;
8 params.J2 = 1082.63e-6;

```

COMPARATIVE NUMERICAL STUDY OF DOMINANT PERTURBATION EFFECTS ON VLEO
SATELLITE ORBIT DEGRADATION

```

9  params.CD = 1.5;
10 params.m = 100;
11 params.A = %pi/4*(1^2);
12 params.wE = [0; 0; 7.2921159e-5];
13
14 //...Initial orbital parameters (given):
15 zp0 = 200;                                //Perigee altitude (km)
16 za0 = 400.34517766;                         //Apogee altitude (km)
17 RAO = 339.94*deg;                            //Right ascension of the
18     node (radians)
19 w0 = 58*deg;                                //Argument of perigee (radians)
20 i0 = 10*deg;                                 //inclination
21 TAO = 332*deg;                               //True anomaly (radians)
22
23 //...Initial orbital parameters (inferred):
24 rp0 = 6378 + zp0;                            //Perigee radius (km)
25 ra0 = 6378 + za0;                            //Apogee radius (km)
26 e0 = (ra0 - rp0) / (ra0 + rp0);             //Eccentricity
27 disp(e0)
28 a0 = (ra0 + rp0) / 2;                        //Semimajor axis (km)
29 disp(a0)
30 h0 = sqrt(mu*a0*(1-e0^2));                 //Angular momentum (km^2/s)
31 disp(h0)
32 T0 = 2 * %pi / sqrt(mu) * a0^1.5;           //Period (s)

```

LISTING 8: Preamble for initial orbital parameters

```

1 function dydt = dragj2_wrapper(t, f)
2     dydt = dragj2(t, f, params);
3 endfunction
4
5 coe30 = [h0, e0, RAO, i0, w0, TAO];
6 [r30, v30] = sv_from_coe(coe30, mu);
7 f30 = [r30(:); v30(:)];
8 [tout30, yout30] = rk4_integrator(dragj2_wrapper, tspan, f30, h);
9
10 n_30_points = size(yout30, "r");
11
12 for m = 1:n_30_points
13 R = yout30(m, 1:3);
14 V = yout30(m, 4:6);

```

COMPARATIVE NUMERICAL STUDY OF DOMINANT PERTURBATION EFFECTS ON VLEO
SATELLITE ORBIT DEGRADATION

```
15 coe = coe_from_sv(R, V, mu);
16
17 h_30_list(m) = coe(1);
18 e_30_list(m) = coe(2);
19 RA_30_list(m) = coe(3)/deg;
20 i_30_list(m) = coe(4)/deg;
21 w_30_list(m) = coe(5)/deg;
22 TA_30_list(m) = coe(6)/deg;
23 a_30_list(m) = coe(7);
24
25 rp_30_list(m) = a_30_list(m) * (1 - e_30_list(m)) - 6378;
26 ra_30_list(m) = a_30_list(m) * (1 + e_30_list(m)) - 6378;
27 end
28
29 // === Orbit counter ===
30 total_angle = 0;
31 TA_prev = TA_30_list(1); // degrees
32 orbit_counter = 1;
33
34 // Period list
35 T_30_list = 2 * %pi / sqrt(mu) * (a_30_list.^1.5); // element-wise
   power
36
37 // Start lists with initial values
38 orbit_counts_30 = [0]; // orbit 0
39 a_at_orbit_30 = [a_30_list(1)];
40 T_at_orbit_30 = [T_30_list(1)];
41
42 for k = 2:n_30_points
43 TA_now = TA_30_list(k);
44 dTA = TA_now - TA_prev;
45
46 // Correct wrap-around
47 if dTA < -180 then
48 dTA = dTA + 360;
49 elseif dTA > 180 then
50 dTA = dTA - 360;
51 end
52
53 total_angle = total_angle + dTA;
```

```
54 TA_prev = TA_now;
55
56 // Completed orbit?
57 if total_angle >= orbit_counter * 360 then
58 orbit_counts_30($+1) = orbit_counter;
59 a_at_orbit_30($+1) = a_30_list(k);
60 T_at_orbit_30($+1) = T_30_list(k);
61 orbit_counter = orbit_counter + 1;
62 end
63 end
64
65 // === Final fractional orbit ===
66 orbits_completed_30 = total_angle / 360;
67 disp("Total orbits completed (including fractions): " + string(
68     orbits_completed_30));
69 orbit_counts_30($+1) = orbits_completed_30;
70 a_at_orbit_30($+1) = a_30_list($);
71 T_at_orbit_30($+1) = T_30_list($);
```

LISTING 9: Example of integration, extraction and ordering of data

Turnitin Report



PRIMARY SOURCES

1	www.unoosa.org Internet Source	1 %
2	baixardoc.com Internet Source	1 %
3	www.yumpu.com Internet Source	1 %
4	ebin.pub Internet Source	1 %
5	tfaws.nasa.gov Internet Source	1 %
6	hdl.handle.net Internet Source	1 %
7	www.au.af.mil Internet Source	1 %
8	Lin Liu. "Chapter 5 Satellite Orbit Design and Orbit Lifespan Estimation", Springer Science and Business Media LLC, 2023 Publication	1 %
9	cenjows.in Internet Source	<1 %
10	www.sgu.ac.id Internet Source	<1 %
11	Submitted to University of Strathclyde Student Paper	<1 %

12 David B. Spencer, Davide Conte. "Interplanetary Astrodynamics", CRC Press, 2023 **<1 %**
Publication

13 Howard D. Curtis. "Introduction to Orbital Perturbations", Elsevier BV, 2014 **<1 %**
Publication

14 edisciplinas.usp.br **<1 %**
Internet Source

15 www.politesi.polimi.it **<1 %**
Internet Source

16 Submitted to University of Sydney **<1 %**
Student Paper

17 etd.repository.ugm.ac.id **<1 %**
Internet Source

18 repository.ipmi.ac.id **<1 %**
Internet Source

19 Submitted to American Public University System **<1 %**
Student Paper

20 dokumen.pub **<1 %**
Internet Source

21 A E Roy. "Orbital Motion", CRC Press, 2020 **<1 %**
Publication

22 dbc.wroc.pl **<1 %**
Internet Source

23 Submitted to University of Sheffield **<1 %**
Student Paper

24 en.wikipedia.org **<1 %**
Internet Source

25	ntrs.nasa.gov Internet Source	<1 %
26	Dennis S. Bernstein. "Spacecraft Trajectory Estimation Using a Sampled-Data Extended Kalman Filter with Range-Only Measurements", Proceedings of the 45th IEEE Conference on Decision and Control, 12/2006 Publication	<1 %
27	Ahmed, Riaz. "Real time hardware in the loop simulation testbed of spacecraft formation flying", 2008 Internet Source	<1 %
28	Submitted to Dominion High School Student Paper	<1 %
29	www.aerospacengineering.net Internet Source	<1 %
30	www.theseus.fi Internet Source	<1 %
31	Fucheng Guo, Yun Fan, Yiyu Zhou, Caigen Zhou, Qiang Li. "Space Electronic Reconnaissance", Wiley, 2014 Publication	<1 %
32	Submitted to University of Birmingham Student Paper	<1 %
33	Curtis, Howard D.. "Introduction to Orbital Perturbations", Orbital Mechanics for Engineering Students, 2014. Publication	<1 %
34	Lewis, H.. "The stability of disposal orbits at super-synchronous altitudes", Acta Astronautica, 200408/11 Publication	<1 %

35 N.H. Crisp, P.C.E. Roberts, F. Romano, K.L. Smith et al. "System modelling of very low Earth orbit satellites for Earth observation", *Acta Astronautica*, 2021 <1 %
Publication

36 P. E. Moran. "Studies in the application of recurrence relations to special perturbation methods", *Celestial Mechanics*, 1973 <1 %
Publication

37 Sulaymon L. Eshkabilov. "Practical MATLAB Modeling with Simulink", Springer Science and Business Media LLC, 2020 <1 %
Publication

38 Submitted to University of Alabama <1 %
Student Paper

39 Submitted to University of Auckland <1 %
Student Paper

40 Fundamentals of Spacecraft Attitude Determination and Control, 2014. <1 %
Publication

41 Submitted to Kuala Lumpur Infrastructure University College <1 %
Student Paper

42 Submitted to University of Bristol <1 %
Student Paper

43 Submitted to University of Canterbury <1 %
Student Paper

44 control.asu.edu <1 %
Internet Source

45 fastercapital.com <1 %
Internet Source

46	th.wikipedia.org Internet Source	<1 %
47	Submitted to Dublin City University Student Paper	<1 %
48	Francesco Sorge, Silvio Zilio. "Classical minimal-coupling theory of a polarized particle", Physical Review D, 2006 Publication	<1 %
49	Submitted to KoE Student Paper	<1 %
50	Mohammad Sanatifar, Roberto Capuzzo-Dolcetta. "Search-based method optimization applied to bi-impulsive orbital transfer", Acta Astronautica, 2019 Publication	<1 %
51	Ying Wang, Fang Zou. "Comparison of telemetry, tracking, and command approaches for very low Earth orbit satellites", CEAS Space Journal, 2025 Publication	<1 %
52	spectrum.library.concordia.ca Internet Source	<1 %
53	vdoc.pub Internet Source	<1 %
54	www.kitasato-u.ac.jp Internet Source	<1 %
55	www.researchgate.net Internet Source	<1 %
56	Submitted to UC, Boulder Student Paper	<1 %

57 Yongchun Xie, Yongjun Lei, Jianxin Guo, Bin Meng. "Spacecraft Dynamics and Control", Springer Science and Business Media LLC, 2022 <1 %
Publication

58 www.genrica.com <1 %
Internet Source

59 apps.dtic.mil <1 %
Internet Source

60 prod-edxapp.edx-cdn.org <1 %
Internet Source

61 www.coursehero.com <1 %
Internet Source

62 Clemente Lauretti, Tiberio Grasso, Eliana de Marchi, Stanislao Grazioso, Giuseppe di Gironimo. "A Geometric Approach to Inverse Kinematics of Hyper-Redundant Manipulators for tokamaks maintenance", Mechanism and Machine Theory, 2022 <1 %
Publication

63 Constantin Traub, Mohamed Khalil Ben-Larbi, Fabrizio Turco, Anton Johann Große Siestrup et al. "Revealing the impact of operational constraints on aerodynamic collision avoidance maneuvers: In-flight results from the BEESAT-4 CubeSat", Acta Astronautica, 2025 <1 %
Publication

64 Francesco Casella, Marco Lovera. "High-accuracy simulation of orbital dynamics: An object-oriented approach", Simulation Modelling Practice and Theory, 2008 <1 %
Publication

65 etd.aau.edu.et <1 %
Internet Source

66 www.geteasysolution.com <1 %
Internet Source

Exclude quotes On
Exclude bibliography On

Exclude matches < 10 words

Curriculum Vitae



Basic Information

Name	Renggani Ghifari
Place of Birth	Jakarta, Indonesia
Date of Birth	2 March, 2002
Address	Ciganjur, Jagakarsa, Jakarta Selatan, DKI Jakarta, Indonesia

Year	Education
2021 - present	International University Liaison Indonesia (IULI)
2019 - 2021	High School - Sekolah Cikal Amri Setu - Jakarta
2017 - 2019	High School - Sekolah Cita Buana- Jakartal
2013 - 2017	Secondary School - Madania School Bogor - Bogor
2013 - 2017	Elementary School - Madania School Bogor - Bogor

Year	Courses
2020	Basic Maintenance Training - UNSURYA

Year	Seminars & Workshops
2023	Basic Maintenance Training - UNSURYA

Year	Work Experiences
2024	Engineering Internship at PT Dirgantara Indonesia (Aerospace Technology Test Center)
